FINITE ELEMENT MODEL UPDATING THROUGH SUM-OF-SQUARES (SOS) OPTIMIZATION AND CONSTRAINED KALMAN FILTERS

A Dissertation
Presented to
The Academic Faculty

by

Dan Li

In Partial Fulfillment
of the Requirements for the Degree
Doctor of Philosophy in the
School of Civil and Environmental Engineering

Georgia Institute of Technology
May, 2020

FINITE ELEMENT MODEL UPDATING THROUGH SUM-OF-SQUARES (SOS) OPTIMIZATION AND CONSTRAINED KALMAN FILTERS

Approved by:

Dr. Yang Wang, Advisor
School of Civil and Environmental Engineering
Georgia Institute of Technology

Dr. Ying Zhang
School of Electrical and Computer Engineering
Georgia Institute of Technology

Dr. Barry Goodno
School of Civil and Environmental Engineering
Georgia Institute of Technology

Dr. Alper Erturk
The George W. Woodruff School of Mechanical Engineering
Georgia Institute of Technology

Dr. Rafi L. Muhanna
School of Civil and Environmental Engineering
Georgia Institute of Technology

Date Approved: [March 06, 2020]

ACKNOWLEDGEMENTS

First of all, I would like to express my sincere gratitude to my advisor Dr. Yang Wang, without whose guidance and support I could not have achieved any academic success during my Ph.D. studies. His expertise and meticulousness created an ideal environment for me to develop as a researcher. I am very grateful to him for providing me the opportunity to study at Georgia Institute of Technology. I am fortunate that Dr. Barry Goodno, Dr. Rafi L. Muhanna, Dr. Ying Zhang, and Dr. Alper Erturk, along with my advisor, constitute my dissertation committee, and I would like to thank all of them for their valuable time and consideration.

I would like to thank Chinese Scholarship Council (CSC) for funding my Ph.D. studies. I also would like to thank Inspecting and Preserving Infrastructure through Robotic Exploration (INSPIRE) University Transportation Center for the financial support during my Ph.D. studies.

I am grateful to Chunhee Cho for his collaboration and guidance on passive antenna sensors during the first two years of Ph.D. studies. I would like to thank Xinjun Dong and Xi Liu for their assistance in finite element model updating and developing wireless sensing system. I also would like to acknowledge Dapeng Zhu, Peter Lander, Yu Otsuki, and Nadine Fahed for providing me the opportunity to work and study with them in a friendly environment.

I would like to thank my friends, Yihai Fang, Xia Li, Yu Hong, Chengwei Li, Gaoxin Wang, Yiqiao Dong, Yichao Yao, Jin Yan, Heng Chi, Yang Jiang, Tuo Zhao, Qimen Xu, Sujith Mangalathu, Edwin Lim for their friendship and those joyful time that

they brought to me. I especially would like to thank Ke Liu, Xinjun Dong, Yidong Qin, Heng Chi, and Yanjie Tong for their help and companionship as my roommates.

Last but not least, I want to sincerely thank my wife Yating Cao for her support and love. I would like to give special thanks to my parents for their encouragement and trust in me.

TABLE OF CONTENTS

LIST OF TABLES

LIST OF FIGURES

LIST OF SYMBOLS AND ABBREVIATIONS

$\mathbf{K}$	Stiffness matrix
$\boldsymbol{\theta}$	Updating variable for stiffness parameters
$\boldsymbol{\theta}^*$	Optimal value of updating variable
$\mathbf{K}_0$	Initial stiffness matrix
$\mathbf{K}_i$	Stiffness influence matrix
$\mathbf{M}$	Mass matrix
ω	Resonance frequency
$\boldsymbol{\psi}$	Mode shape vector
DOF	Degree of freedom
$\mathcal{M}$	The set of DOFs measured by sensors
$\mathcal{U}$	The set of the remaining unmeasured DOFs
$n_{\mathcal{M}}$	The number of DOFs in the set $\mathcal{M}$
$n_{\mathcal{U}}$	The number of DOFs in the set $\mathcal{U}$
n_{modes}	Number of measured modes
$\boldsymbol{\omega}$	Measured resonance frequencies. $\boldsymbol{\omega} = \left(\omega_1, \omega_2, \cdots, \omega_{n_{\text{modes}}}\right)^{\mathrm{T}} \in \mathbb{R}^{n_{\text{modes}}}$
$\boldsymbol{\psi}_{\mathcal{M}}$	Measured entries in mode shape vectors. $\boldsymbol{\psi}_{\mathcal{M}} = \left(\boldsymbol{\psi}_{\mathcal{M},1}^{\mathrm{T}}, \boldsymbol{\psi}_{\mathcal{M},2}^{\mathrm{T}}, \cdots, \boldsymbol{\psi}_{\mathcal{M},n_{\text{modes}}}^{\mathrm{T}}\right)^{\mathrm{T}} \in \mathbb{R}^{n_{\mathcal{M}} \cdot n_{\text{modes}} \times 1}$
$\boldsymbol{\psi}_{\mathcal{U}}$	Unmeasured entries in mode shape vectors. $\boldsymbol{\psi}_{\mathcal{U}} = \left(\boldsymbol{\psi}_{\mathcal{U},1}^{\mathrm{T}}, \boldsymbol{\psi}_{\mathcal{U},2}^{\mathrm{T}}, \cdots, \boldsymbol{\psi}_{\mathcal{U},n_{\text{modes}}}^{\mathrm{T}}\right)^{\mathrm{T}} \in \mathbb{R}^{n_{\mathcal{U}} \cdot n_{\text{modes}} \times 1}$
$\mathbf{L}_{\boldsymbol{\theta}}$	Lower bound of $\boldsymbol{\theta}$
$\mathbf{U}_{\boldsymbol{\theta}}$	Upper bound of $\boldsymbol{\theta}$
SOS	Sum-of-squares
SDP	Semidefinite programming

EKF	Extended Kalman filter
UKF	Unscented Kalman filter
CEKF	Constrained extended Kalman filter
CUKF	Constrained unscented Kalman filter
$\mathbf{x}$	State vector
$\mathbf{u}$	Known excitation
$\mathbf{w}$	Zero-mean white Gaussian process noise
$\boldsymbol{\Sigma}_{\mathbf{w}}$	Covariance matrix of $\mathbf{w}$
$\boldsymbol{f}$	State-space process equation
$\mathbf{y}_k$	Measurement at time $t = k\Delta t$
$\mathbf{v}_k$	Zero-mean white Gaussian measurement noise at time $t = k\Delta t$
$\boldsymbol{\Sigma}_{\mathbf{v}}$	Covariance matrix of $\mathbf{v}$
$\boldsymbol{h}$	Measurement equation
$\hat{\mathbf{x}}_{k\|k-1}$	The *a priori* estimate of $\mathbf{x}$ at time $t = k\Delta t$
$\boldsymbol{\Sigma}_{\mathbf{x}_{k\|k-1}}$	Covariance matrix of the *a priori* estimate of $\mathbf{x}$ at time $t = k\Delta t$
$\hat{\mathbf{y}}_{k\|k-1}$	Predicted measurement at time $t = k\Delta t$
$\mathbf{L}_k$	The Kalman gain matrix at time $t = k\Delta t$
$\mathbf{H}_k^{\mathrm{x}}$	The linearized matrix of the measurement equation $\boldsymbol{h}$ with respect to $\mathbf{x}$ at time $t = k\Delta t$
$\mathbf{H}_k^{\mathrm{v}}$	The linearized matrix of the measurement equation $\boldsymbol{h}$ with respect to $\mathbf{v}$ at time $t = k\Delta t$
$\hat{\mathbf{x}}_{k\|k}$	The *a posteriori* estimate of $\mathbf{x}$ at time $t = k\Delta t$
$\boldsymbol{\Sigma}_{\mathbf{x}_{k\|k}}$	Covariance matrix of the *a posteriori* estimate of $\mathbf{x}$ at time $t = k\Delta t$
$\boldsymbol{\Phi}_k^{\mathbf{x}}$	The state transition matrix of the process equation $\boldsymbol{f}$ with respect to $\mathbf{x}$ at time $t = k\Delta t$

$\mathbf{\Phi}_k^{\mathbf{w}}$	The state transition matrix of the process equation $\boldsymbol{f}$ with respect to $\mathbf{w}$ at time $t = k\Delta t$
n_c	The number of inequality constraints
n_{ac}	The number of the active inequality constraints
$\mathbf{A}$	Constant coefficient matrix
$\mathbf{b}$	Constant coefficient vector
$\mathbf{A}_{\mathrm{a}}$	Coefficient matrix of the active inequality constraints
$\mathbf{b}_{\mathrm{a}}$	Coefficient vector of the active inequality constraints
$\mathbf{r}_k$	Measurement residual at time $t = k\Delta t$
$\mathbf{\Sigma}_{\mathbf{y}_{k\|k-1}}$	Innovation covariance at time $t = k\Delta t$
$\boldsymbol{\nu}$	Lagrange multiplier
$\tilde{\mathbf{L}}_k$	The unconstrained Kalman gain at time $t = k\Delta t$
$\tilde{\mathbf{x}}_{k\|k}$	The unconstrained *a posterior* state estimate at time $t = k\Delta t$
N	The number of augmented state vector
$\mathbf{x}^a$	Augmented state vector
$\boldsymbol{x}_{k\|k-1,i}^a$	The *i*-th sigma point
W_i	Weighting coefficient of the *i*-th sigma point
$\boldsymbol{\mathcal{Y}}_{k\|k-1,i}$	Predicted measurement of the *i*-th sigma point
$\mathbf{\Sigma}_{\mathbf{xy}_{k\|k-1}}$	Cross covariance between the *a priori* estimate $\hat{\mathbf{x}}_{k\|k-1}$ and its measurement $\hat{\mathbf{y}}_{k\|k-1}$
$\ddot{q}_g$	Ground acceleration
q	Displacement
z	Hysteretic displacement
β, γ, and n	Dimensionless parameters controlling the shape and magnitude of the hysteresis loop

$\mathrm{sgn}(\cdot)$	Signum function
ρ	Curvature controlling factor
MAC	Modal assurance criterion
$\boldsymbol{\iota}$	Influence vector

SUMMARY

Finite element (FE) modeling techniques optimize model parameter values for improving the predication accuracy of a numerical model. This research investigates algorithms utilizing the frequency-domain modal properties and the time-domain dynamic responses for FE model updating. In terms of frequency-domain model updating, a global optimization algorithm, the sum-of-squares (SOS) method, is proposed to solve the modal dynamic residual formulation for finding optimal model parameters. The SOS method can reformulate a nonconvex polynomial optimization problem into a convex semidefinite programming (SDP) problem, the global optimal solution of which can be reliably solved. In order to improve the computational efficiency, the sparsity of the optimization problem and facial reduction technique are investigated for reducing the size of the reformulated SDP problem. The proposed SOS method and efficiency improvement techniques are validated through numerical studies of a four-story shear frame structure and a plane truss structure.

In terms of time-domain model updating, the constrained extended Kalman filter (CEKF) and the constrained unscented Kalman filter (CUKF) are proposed to recursively update model parameters for both linear and nonlinear structures. Incorporating constraints during the model updating process can effectively prevent parameter estimates from being unrealistic. Analytical solution of the Kalman gain is derived when there are inequality constraints. With the explicit expression of the Kalman gain, the estimation process can be significantly accelerated. The proposed CEKF and CUKF are validated through numerical

studies of a linear four-story shear frame structure and a single degree of freedom (SDOF) Bouc-Wen hysteretic system.

Besides numerical studies, experimental measurements are also used to evaluate the model updating performance of the proposed methods. The first example is a four-story shear frame structure in laboratory. The second example is a full-scale reinforced concrete frame structure in field. Model updating performance of proposed SOS optimization method and constrained Kalman filters are investigated through comparison between simulated responses and experimental measurements.

CHAPTER 1. INTRODUCTION

In civil engineering, finite element (FE) models are widely used to simulate behaviors of structures and provide guidance for design and maintenance. For example, the FE models can be used to analyze the internal stress and strain distribution of structures or to predict dynamic responses of structures under excitations such as earthquake and strong wind. The validity of an FE model depends on the suitable values of model parameters. While nominal property values and simplified modeling are usually adopted in FE models, in practice, there are always uncertain material properties and boundary conditions in structures. These uncertainties may cause inaccurate and unreliable simulation results. To address this challenge, FE model updating techniques have been developed to update the uncertain model parameters based on experimental data collected from structures. Figure 1-1 illustrates the FE model updating procedure. Starting from initial model parameters, the structural responses are simulated and compared with experimental data. The model parameters are updated until the difference between simulated and experimental responses

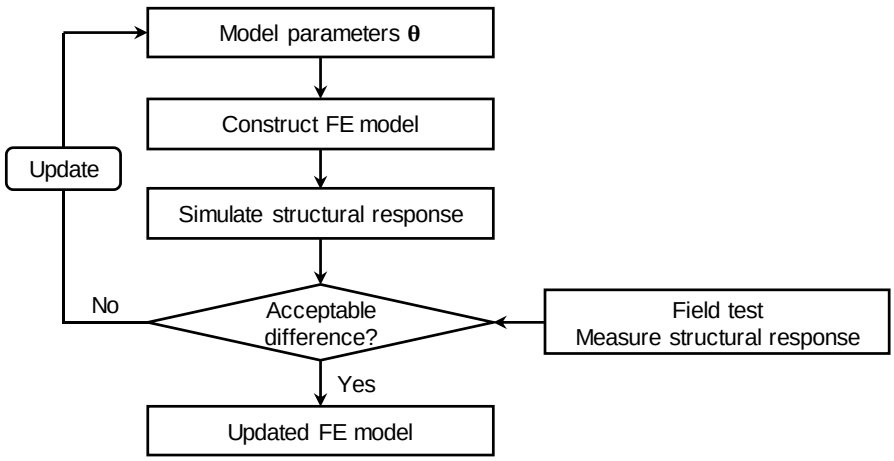

Figure 1-1 Flow chart of FE model updating

satisfies the requirement. After tuning model parameters, the updated FE model can more accurately predict behaviors of a structure under various loading cases [1].

Besides improving simulation performance, FE model updating techniques also find extensive application in structural health monitoring (SHM). Structural damage can result in changes of structural properties, especially reduction of stiffness. By updating structural stiffness parameters over time, structural damage can be identified, and the updating results may help evaluating the structural condition. Teughels and De Roeck identified the damage pattern of a prestressed concrete bridge by FE model updating using modal data [2]. Fang *et al.* developed a sensitivity-based model updating approach to identify the damage in a tested reinforced concrete frame [3]. Weber *et al.* investigated a regularization method for FE model updating and applied the method for identifying damage of a frame using both simulated and experimental data [4]. Other studies related to FE model updating for SHM can be found in [5-9].

Experimentally measured data serve as the baseline for FE model updating. With the development of sensing technology, dynamic responses (e.g. acceleration and

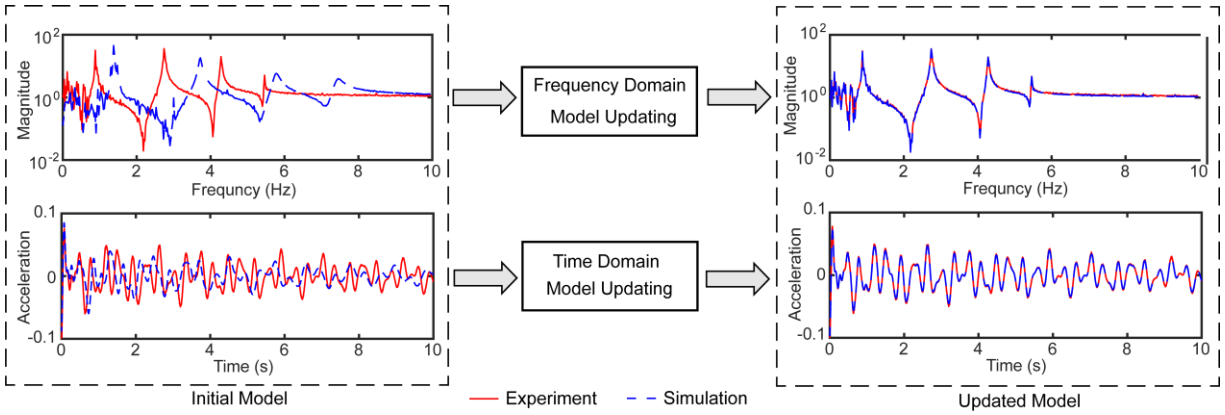

Figure 1-2 Frequency domain and time domain model updating algorithms

displacement) of structures can be measured from vibration experiments. These responses and the modal properties extracted from the measurements provide relevant information regarding the structural properties of interest (e.g. stiffness, damping and mass). According to the data utilized for model updating, these algorithms can be categorized into two groups: 1) frequency-domain algorithm, and 2) time-domain algorithm, as shown in Figure 1-2.

1.1 Frequency-Domain Model Updating

Most of the frequency-domain algorithms are based on a linear, elastic, and time-invariant structural model. To apply these algorithms, the modal properties, such as natural frequencies, mode shapes and damping ratios, of a structure are extracted from experimentally measured data and serve as the baseline for updating the FE model. Certain parameters (e.g. stiffness, damping, and mass parameters) in the FE model will be updated by minimizing an objective function measuring the discrepancies between the experimental and simulated modal properties. In order to obtain reliable solution of updating parameters, global optimization algorithms have been investigated to solve the formulated model updating problem. Section 1.1.1 introduces various FE model updating algorithms using frequency-domain data. Section 1.1.2 presents several methods to solve global optimum of the FE model updating problem.

1.1.1 FE Model Updating Using Modal Properties

Modal properties obtained from vibration tests for structures are usually used to update parameters in FE models. Natural frequencies are known to be significantly affected by the structural parameters including material density and elastic modulus, and thus can serve as an indicator of the change in model parameters. Zhang *et al.* updated the

parameters in an FE model to reduce the difference between the measured and simulated natural frequencies, and this approach was validated through a scaled suspension bridge model [10]. Besides natural frequencies, incorporating mode shapes into the objective function can achieve more accurate updated FE model. Ladevèze *et al.* proposed an approach to take into account both the experimentally obtained natural frequencies and corresponding mode shapes to update stiffness and mass matrices of the FE model [11]. Teughels *et al.* investigated damage assessment of a reinforced concrete beam by using a sensitivity-based FE model updating approach which iteratively minimizes the difference between the measured natural frequencies and mode shapes and the corresponding simulated predictions [12]. Jashi and Ren utilized the modal flexibility residual formed from natural frequencies and mode shapes to conduct FE model updating and detect possible damage in structures [13]. Mottershead *et al.* introduced a sensitivity method incorporating the natural frequencies and the mode shapes for FE model updating [14]. Some studies attempted to minimize the dynamic force/input residual of the equations of motion in frequency domain, which is defined as the difference between the two sides of the equation using updated model and measured dynamic forces and displacements [15, 16]. When evaluated at resonance frequencies and assuming normal modes, the dynamic force vanishes and the input residual simplifies to the modal dynamic residual of the generalized eigenvalue equation [17-19].

Researchers also investigate the frequency response functions (FRFs) for updating FE models using the frequency domain data. Imregun *et al.* investigated the FRF-based FE model updating method and corresponding solution strategies [20]. The effectiveness of the proposed method and numerical stability were studied through updating a medium-size

finite element model of a plate-beam structure [21]. Sipple and Sanayei presented an FRF-based FE model updating framework and showed the usefulness of this approach through several simulated test cases for damage detection [22]. Arora *et al.*utilized complex FRFs to update not only mass and stiffness matrices but also damping matrix [23].

1.1.2 Global Optimization Methods

The frequency domain FE model updating algorithms have shown great progress in parameter identification, condition assessment, and damage detection by minimizing the difference between as-built structures and the corresponding numerical models. Typically, these optimization problems formulated for model updating are nonconvex, which means there can be unknown number of local minima over the feasible domain. Traditional optimization algorithms, e.g. the gradient based algorithm, can be easily trapped at a local minimum and fail to find the global solution. Attempts have been made to seek the global optimum of the model updating problems. Levin and Lieven applied the genetic algorithm (GA) and the simulated annealing (SA) algorithm to update an FE model of a flat plat wing structure [24]. The results show that these stochastic search algorithms are capable of finding global solution of the model updating problem, while the performance highly depends on the choice of updating parameters.

Besides stochastic search algorithms, gradient search from multiple starting points has also been investigated for solving the global optimum of model updating problem. Teughels *et al.* utilized a population of coupled local minimizers (CLM) from gradient-based optimization algorithm to find the global optimum of the optimization problem [25]. The algorithm has been validated through model updating for a reinforced concrete beam.

Bakir *et al.* compared the CLM algorithm with local optimization algorithms, such as Levenberg-Marquardt algorithm and Gauss-Newton algorithm, and demonstrated that the CLM algorithm achieves better results in FE model updating problems [26].

Although achieving success in finding reliable solution for model updating problems, both stochastic search algorithms and gradient search from multiple starting points are heuristic. Thus, these algorithms can improve the updating results to some extent but cannot guarantee global optimality.

In this dissertation, the sum-of-squares (SOS) method is proposed to solve the modal dynamic residual formulation in FE model updating. It has been shown that if an optimization problem consists of only polynomials, the SOS method and its variant can be applied to approximate the nonconvex problem with a convex semidefinite programming (SDP) problem. The re-formulated SDP problem can be solved efficiently by many existing algorithms, such as the interior-point method. As the SDP problem is convex, the solution is guaranteed to be globally optimal. The SOS method has made significant impact on global optimization in many different fields, for example tensor decomposition [27, 28], computational geometry [29], and control theory [30].

In the field of FE model updating, the SOS optimization method can be applied to solve the modal dynamic residual formulation, which consists of polynomial objective function and polynomial constraints. The global optimum of the modal dynamic residual formulation can be obtained from the solution of the reformulated SDP problem. However, despite the appeal of yielding global optimality, the computational complexity of the SOS method grows rapidly when the polynomial optimization problem has a large number of

variables and/or high degree [31, 32]. One method to alleviate the difficulty is to exploit the sparsity in the polynomial optimization problem and eliminate some constraints in the formulated SDP problem. The so-called sparse SOS method can result in an SDP problem with smaller size and improve the overall computational efficiency. Furthermore, it turns out that the SDP problems formulated by both the standard and the sparse SOS approaches may fail to satisfy the Slater condition (strict feasibility), which plays an important role in the convergence of most interior-point solvers [33]. The failure to satisfy the Slater condition increases the difficulty of finding the optimal solution of the SDP problem using numerical algorithms. To address this challenge, facial reduction technique can be applied to restrict such an SDP problem onto a feasible set with lower dimension and yields an equivalent SDP problem for which there are strictly feasible points. The smaller equivalent SDP can then be solved by a numerical solver in a more stable manner.

1.2 Time-Domain Model Updating

The other category of FE model updating algorithms is the time-domain algorithms. Rather than using the modal properties extracted from the measured data, the time-domain algorithm directly utilizes the measured time history data to conduct FE model updating. Section 1.2.1 introduces various FE model updating algorithms using time-domain data. Section 1.2.2 presents Kalman filtering techniques for model updating. Section 1.2.3 covers algorithms incorporating constraints during Kalman filtering process.

1.2.1 FE Model Updating Using Time-Domain Data

The least-squares estimation (LSE) has been investigated to update model parameters by recursively minimizing the difference between simulated and experimental responses

of structures. Yang and Lin proposed an adaptive tracking technique based on LSE for tracking the abrupt changes of system parameters in structures and validated the proposed method through simulation [34]. Most of these LSE-based methods require measurements on displacement and velocity. The high measurement requirement limits the application of LSE-based methods on practical applications [35].

Sequential Monte Carlo method is another technique for time-domain model updating. Li *et al*. proposed a fast model updating approach based on sequential Monte Carlo method and validated the approach through simulation [36]. Chatzi and Smyth proposed a model updating approach with mutation operators improving the quality and quantity of samples to achieve better estimation of parameters [37]. Sequential Monte Carlo method usually relies on a large number of sampling points to estimate parameters together with system states. Although this method performs well on parameter identification, the computation complexity limits the application on small or medium-size problems.

1.2.2 Kalman Filtering Techniques for Model Updating

The nonlinear versions of Kalman filter, especially extended Kalman filter (EKF) and unscented Kalman filter (UKF), are also commonly used identification algorithms for civil structures. Kalman filter produces *a posteriori* probabilistic estimates of unknown state variables based on system equations and noisy measurements. Parameter identification is performed by treating the model parameters as augmented system states and thus, estimated through the measurement data. It should be noted that the augmented system is usually nonlinear, no matter the original system is linear or nonlinear. EKF

linearizes the system equation and measurement equation around the current optimal estimate, and updates the estimate based on the linearized equations. Yang *et al.* developed an adaptive EKF to tack changes of system parameters for structural damage detection [38].

A powerful alternative to EKF is UKF which relies on the unscented transformation for estimating system states and parameters. UKF is designed based on the intuition that it should be easier to approximate a given distribution than to approximate an arbitrary nonlinear function. At each iteration, UKF generates a sample distribution by a set of sampling points called sigma points, which capture the mean and covariance of the *a posteriori* distribution of system states. These sigma points can be easily propagated through the nonlinear system equation and used for updating the estimate. Chatzis *et al*. validated UKF on damage detection and finite element model updating through experiments on a steel structure [39].

Different from frequency domain algorithms that are mostly applicable to linear structures, EKF and UKF can be used for system identification of nonlinear structures. Nonlinearity and inelasticity are usually encountered in structures under severe dynamic loading, such as earthquake and strong wind. Reliable modeling of structures subject to such extreme events is of critical importance to structural damage assessment and post event maintenance. These nonlinear and inelastic structural behaviors due to dynamic loading usually exhibit in a form of hysteresis, which refers to the path-dependent relationship between restoring force and deformation. The area of the hysteresis loop represents the dissipated energy during the loading duration. Detailed modeling of hysteretic behaviors of structures is usually too complicated for engineering application [40]. In addition, the obtained models are always problem dependent and difficult to be

extended for general usage. For these reasons, phenomenological models are developed to characterize the hysteretic features. A survey on the phenomenological models for hysteresis can be found in [41]. Among these models, the Bouc-Wen model has been extensively used in civil engineering to describe the hysteresis phenomenon of, for example, magnetorheological (MR) dampers [42-44], beam-column joints [45, 46], and soil-structure interaction [47].

The governing equation of the Bouc-Wen model is a first-order nonlinear differential equation, the parameters of which control the shape and size of the hysteresis loop. In order to accurately describe the hysteretic properties of structures, the parameters in the Bouc-Wen model need to be identified from the output and/or the input of the structural system. The application of EKF and UKF in parameter identification for hysteretic systems is also extensively investigated and reported in the literature [48-53].

1.2.3 Constrained Kalman Filters

It has been shown that EKF works well for system with mild nonlinearity but often provides unreliable estimates for highly nonlinear systems due to the large linearization error. Researchers have investigated techniques to improve the accuracy of EKF and applying constraints on parameters during the estimation process is one effective technique. Yang and Ma proposed a constrained EKF, in which the constrained parameters are replaced by parameters in the entire solution space through specific functions, for example sinusoidal functions and square function [54]. In this way, the original problem has been converted to a problem of estimating new parameters using the standard EKF. However, these functions are not one-to-one functions and thus multiple values of a new

parameter could correspond to the same value of the original parameter. This fact increases the difficulty of accurate parameter estimation. Sen and Bhattacharya investigated a constrained EKF which restricts the Kalman gain to ensure that the updated estimate lies within the constrained space [55]. This restricted Kalman gain is obtained by solving a constrained optimization problem, which can be computational expensive. This dissertation adopts the idea of restricting the Kalman gain and derives the analytical solution of the Kalman gain when there are inequality constraints. With the explicit expression of the Kalman gain, the estimation process can be significantly accelerated.

Comparing with EKF, UKF provides better accuracy in nonlinear structure model updating. Wu and Smyth compared EKF and UKF on updating parameters of a single degree of freedom (SDOF) Bouc-Wen system, and showed that UKF outperformed EKF in estimation accuracy for this highly nonlinear system [53]. Nevertheless, UKF also attempts to find the optimal estimate of model parameters from the entire parameter space, while the model parameters usually possess physical meaning and cannot take arbitrary values. This requirement necessitates applying boundary constraints in the parameter identification using UKF for reasonable estimation. Kandepu *et al.* proposed a constrained UKF algorithm projecting sigma points which are outside the feasible region onto the boundary of the feasible region [56]. However, this projection method cannot ensure that the sigma points capture the mean and covariance of system states. Vachhani *et al.* proposed a constrained UKF algorithm by reducing the step size of sigma points [57]. This constrained method can preserve the mean but cannot preserve the covariance of system states. In this dissertation, instead of constraining sigma points, the Kalman gain in UKF

is constrained by the same way as EKF to ensure that the estimates follow applied constraints while preserving the mean and covariance of system states.

1.3 Organization of Dissertation

The rest of this dissertation is organized as follows.

Chapter 2 introduces the formulation of the modal dynamic residual approach for linear FE model updating. To find the global optimum of the model updating problem, detailed description of the SOS optimization method is presented. Numerical study of a four-story shear structure is conducted to compare the performance of the SOS optimization method and local optimization algorithms and to show that the SOS method can reliably find the global optimum. The sparsity in the SOS method is exploited to reduce the computational efforts. To further reduce the size of the optimization problem, facial reduction algorithm is investigated to take advantage of the failure of the Slater constraint qualification. Numerical studies of a 2D plane truss structure are presented to show the sparse SOS method and facial reduction algorithm can effectively improve the computational efficiency.

Chapter 3 briefly reviews EKF and UKF algorithms for FE model updating. Details of the constrained EKF (CEKF) and the constrained UKF (CUKF) are provided for parameter identification. Numerical studies of a linear four-story shear structure and a nonlinear single degree of freedom (SDOF) Bouc-Wen hysteretic system are conducted to evaluate the performance of the proposed CEKF and CUKF algorithms. In the nonlinear example, a modified and differentiable Bouc-Wen model is proposed. For the proposed

model, partial derivatives of the system equations with respect to hysteretic parameters can be analytically and explicitly calculated for the implementation of EKF and CEKF.

Chapter 4 investigates the proposed model updating approaches using experimental data of a four-story shear structure. Depending on a linear model, the inter-story stiffness parameters of the structure are updated through SOS optimization method on modal dynamic residual formulation. Depending on a nonlinear model with hysteresis, parameters including damping coefficients, inter-story stiffness, and hysteretic parameters are updated using Kalman filters (EKF, UKF, CEKF, and CUKF). Based on the updated model parameters, the structural responses of the structure are simulated and compared with experimental measurements to evaluate the updating performance.

Chapter 5 presents experimental validation of the proposed CEKF and CUKF on a full-scale concrete frame structure. Experimental setup and details of the FE model are introduced. Model order reduction techniques are applied for improving computational efficiency of time-domain analysis. Based on experimentally measured acceleration responses of the frame, model parameters are identified through constrained Kalman filters. Model updating performance of proposed approaches are evaluated through comparison between simulated responses and experimental measurements.

Chapter 6 summarizes the research and presents main conclusions. Future research directions on FE model updating are discussed.

CHAPTER 2. MODEL UPDATING USING SUM-OF-SQUARES (SOS) OPTIMIZATION OVER MODAL DYNAMIC RESIDUAL

This chapter addresses finite element model updating for linear and elastic structures using frequency domain data. Modal dynamic residual formulation is adopted here to update selected model parameters. This approach formulates an optimization problem to find the suitable values of model parameters by minimizing the residuals of the generalized eigenvalue equations from structural dynamics. In general, this formulation leads to a nonconvex polynomial optimization problem, for which local optimization algorithms can be applied but may converge at a local optimum far away from the global optimum. To address this challenge, sum-of-squares (SOS) optimization method is utilized to convert nonconvex polynomial optimization problems into convex semidefinite programming (SDP) problems, for which the global optimum can be conveniently solved. Furthermore, when the polynomial objective function consists of several polynomials only involving a small number of variables, sparse SOS optimization method can be applied to significantly reduce the computation efforts by eliminating some constraints in the formulated SDP problem. To further improve the efficiency of SOS optimization methods, facial reduction technique is used to regularize the SDP problems arising from modal dynamic residual formulation into ones with smaller size. Finally, the proposed methods are validated by simulation on a four-story shear structure and a plane truss structure. Model updating of the four-story shear structure has shown that the SOS optimization method can reliably find the global optimum of nonconvex model updating problems using the modal dynamic residual formulation. The plane truss structure example demonstrates that the sparse SOS optimization method greatly reduces the computation effort by exploiting the sparsity in

the polynomial and the facial reduction technique further reduces computation time by regularizing the SDP problems which fail the Slater condition (strict feasibility).

2.1 Modal Dynamic Residual Formulation

This section introduces the modal dynamic residual formulation for finite element model updating based on linear, elastic, and time-invariant structural models. For brevity, the formulation is provided only for updating stiffness values (although the formulation can be easily extended for updating mass and damping coefficient). Consider a linear structure with N degrees of freedom (DOFs). The updating variable for stiffness values is represented by a vector variable $\boldsymbol{\theta} \in \mathbb{R}^{n_{\boldsymbol{\theta}}}$, where each entry θ_i is the relative change from the initial/nominal value of a selected stiffness parameter (to be updated). The stiffness matrix $\mathbf{K} \in \mathbb{R}^{N\times N}$ can be written as an affine matrix function of the updating variable $\boldsymbol{\theta}$:

$$\mathbf{K}(\boldsymbol{\theta}) = \mathbf{K}_0 + \sum_{i=1}^{n_{\boldsymbol{\theta}}} \theta_i \mathbf{K}_i \tag{2-1}$$

where $\mathbf{K}_0 \in \mathbb{R}^{N\times N}$ denotes the initial stiffness matrix and $\mathbf{K}_i \in \mathbb{R}^{N\times N}$ denotes the i-th (constant) stiffness influence matrix corresponding to the updating variable θ_i. Finally, $\mathbf{K}(\boldsymbol{\theta}): \mathbb{R}^{n_{\boldsymbol{\theta}}} \to \mathbb{R}^{N\times N}$ represents that the structural stiffness matrix is written as an affine matrix function of the vector variable $\boldsymbol{\theta} \in \mathbb{R}^{n_{\boldsymbol{\theta}}}$. Because some stiffness parameters may not need updating, it is not required that $\mathbf{K}_0 = \sum_{i=1}^{n_{\boldsymbol{\theta}}} \mathbf{K}_i$.

In theory, given a pair of resonance frequency ω and mode shape vector $\boldsymbol{\psi} \in \mathbb{R}^N$, only the actual/correct value of updating parameter $\boldsymbol{\theta}^*$ can provide the stiffness matrix $\mathbf{K}(\boldsymbol{\theta}^*)$ that satisfies the generalized eigenvalue equation:

$$[\mathbf{K}(\boldsymbol{\theta}^*) - \omega^2\mathbf{M}]\boldsymbol{\psi} = \mathbf{0} \tag{2-2}$$

Based on this concept, modal dynamic residual formulation updates parameter $\boldsymbol{\theta}$ by minimizing the residuals of the generalized eigenvalue equations in structural dynamics. The residuals are calculated using matrices generated by the finite element model in combination with experimentally obtained modal properties. To obtain modal properties of the structure from dynamic modal testing, sensors are instrumented to measure responses of the structure. In general, not all DOFs of the structure can be measured. The set of DOFs measured by sensors is denoted as $\mathcal{M}$, and the set of the remaining unmeasured DOFs is denoted as $\mathcal{U}$. The number of DOFs in the set $\mathcal{M}$ is denoted as $n_{\mathcal{M}}$, and similarly the number of DOFs in the set $\mathcal{U}$ is denoted as $n_{\mathcal{U}}$. The measured modal properties of the structure usually include the first several resonance frequencies, $\boldsymbol{\omega} = \left(\omega_1, \omega_2, \cdots, \omega_{n_{\text{modes}}}\right)^{\text{T}} \in \mathbb{R}^{n_{\text{modes}}}$, and measured entries $\boldsymbol{\psi}_{\mathcal{M}} = \left(\boldsymbol{\psi}_{\mathcal{M},1}^{\text{T}}, \boldsymbol{\psi}_{\mathcal{M},2}^{\text{T}}, \cdots, \boldsymbol{\psi}_{\mathcal{M},n_{\text{modes}}}^{\text{T}}\right)^{\text{T}} \in \mathbb{R}^{n_{\mathcal{M}} \cdot n_{\text{modes}} \times 1}$ of corresponding mode shapes. The maximum magnitude of each mode shape $\boldsymbol{\psi}_{\mathcal{M},i}$ is normalized to be 1.

The entries corresponding to the unmeasured DOFs, $\boldsymbol{\psi}_{\mathcal{U}} = \left(\boldsymbol{\psi}_{\mathcal{U},1}^{\text{T}}, \boldsymbol{\psi}_{\mathcal{U},2}^{\text{T}}, \cdots, \boldsymbol{\psi}_{\mathcal{U},n_{\text{modes}}}^{\text{T}}\right)^{\text{T}} \in \mathbb{R}^{n_{\mathcal{U}} \cdot n_{\text{modes}} \times 1}$, are unknown and need to be treated as optimization variables. With updating variable $\boldsymbol{\theta} \in \mathbb{R}^{n_{\boldsymbol{\theta}}}$ and unmeasured mode shape entries $\boldsymbol{\psi}_{\mathcal{U}} \in \mathbb{R}^{n_{\mathcal{U}} \cdot n_{\text{modes}} \times 1}$ as the optimization variables, the model updating problem can be formulated by minimizing following residual r:

$$\underset{\boldsymbol{\theta},\,\boldsymbol{\psi}_{\mathcal{U}}}{\text{minimize}}\ r = \sum_{i=1}^{n_{\text{modes}}} \left\| [\mathbf{K}(\boldsymbol{\theta}) - \omega_i^2 \mathbf{M}] \begin{Bmatrix} \boldsymbol{\psi}_{\mathcal{M},i} \\ \boldsymbol{\psi}_{\mathcal{U},i} \end{Bmatrix} \right\|_2^2 \tag{2-3}$$

$$\text{subject to } \mathbf{L}_{\boldsymbol{\theta}} \leq \boldsymbol{\theta} \leq \mathbf{U}_{\boldsymbol{\theta}}$$

where $\|\cdot\|_2$ denotes the ℓ_2-norm; $\mathbf{M}$ is the mass matrix, which is considered accurate. The formulation implies that both $\mathbf{K}(\boldsymbol{\theta})$ and $\mathbf{M}$ are reordered according to the sets $\mathcal{M}$ and $\mathcal{U}$. Constant vector $\mathbf{L}_{\boldsymbol{\theta}}$ denotes the lower bound for $\boldsymbol{\theta}$ and constant vector $\mathbf{U}_{\boldsymbol{\theta}}$ denotes the upper bound. The sign "$\leq$" is overloaded to represent entry-wise inequality.

Although the bound constraints in Eq. (2-3) define a convex feasible set, the objective function is a 4-*th* order polynomial function which is nonconvex in general. A special case is when all DOFs are measured, i.e. $\boldsymbol{\psi}_{\mathcal{U}}$ vanishes in the optimization problem. The formulation then leads to a convex least-squares problem of updating parameter $\boldsymbol{\theta}$. However, in practice, usually not all DOFs are instrumented/measured and the problem Eq. (2-3) is a nonconvex optimization problem with the cross term between $\boldsymbol{\theta}$ and $\boldsymbol{\psi}_{\mathcal{U}}$ [58]. When the problem is nonconvex, most off-the-shelf optimization algorithms can only find some local optima which may greatly differ from the global optimum and result in inaccurate updating results.

Although the optimization problem Eq. (2-3) is generally nonconvex, the objective function and constraints can be equivalently formulated as polynomial functions. This property enables of finding the global optimum of the optimization problem by the sum-of-squares (SOS) optimization method. The SOS optimization method can relax a nonconvex polynomial optimization problem into a convex semidefinite programming (SDP) problem. The SDP problem then can be reliably solved by existing optimization

algorithms, such as the interior-point method, and the global optimality of the solution is guaranteed [59]. The next section presents details of the SOS optimization method.

2.2 SOS Optimization Method

This section introduces the SOS optimization method which can be applicable for finding the global solutions for polynomial optimization problems. The relationship between nonnegative polynomials and SDP problems is presented first. Based on this relationship, this section describes the SOS optimization method that relaxes nonconvex polynomial problems into convex SDP problems. In addition, the method is shown to extract the solutions of the original polynomial optimization problems from the solutions of dual problems of the formulated SDP problems. A four-story shear structure is simulated to validate the proposed SOS optimization method. Shown in the example, local optimization algorithms, such as Gauss-Newton algorithm and trust-region-reflective algorithm, can be applied directly to the optimization problem, while they cannot guarantee to find the global optimum. On the other hand, the SOS optimization method can reliably solve the global optimum from the formulated convex SDP problem.

Notations used in this section are listed in Table 2-1.

Table 2-1 Notations used in SOS optimization method

$\mathbb{Z}$	The set of integers
$\mathbb{Z}_+$	The set of nonnegative integers
$\mathbb{Z}_{++}$	The set of positive integers
$\mathbb{S}^n$	The set of real symmetric matrices of size $n \times n$
$\mathbb{S}_+^n$	The set of positive semidefinite matrices of size $n \times n$
$\mathbb{S}_{++}^n$	The set of positive definite matrices of size $n \times n$
$\mathbf{A} \succcurlyeq \mathbf{0}$	A positive semidefinite matrix $\mathbf{A} \in \mathbb{S}_+^n$
$\mathbf{A} \succ \mathbf{0}$	A positive definite matrix $\mathbf{A} \in \mathbb{S}_{++}^n$
$\langle \mathbf{A}, \mathbf{B} \rangle$	The inner product between matrices $\mathbf{A} \in \mathbb{S}^n$ and $\mathbf{B} \in \mathbb{S}^n$. $\langle \mathbf{A}, \mathbf{B} \rangle = \mathrm{Tr}(\mathbf{A}^{\mathrm{T}}\mathbf{B}) = \sum a_{ij} b_{ij}$
$\mathbf{x}$	Variable vector. $\mathbf{x} = (x_1, x_2, \cdots, x_n) \in \mathbb{R}^n$
$\boldsymbol{\alpha}$	Nonnegative power vector. $\boldsymbol{\alpha} = (\alpha_1, \alpha_2, \cdots, \alpha_n) \in \mathbb{Z}_+^n$
$\mathbf{x}^{\boldsymbol{\alpha}}$	A monomial in $\mathbf{x}$ with power $\boldsymbol{\alpha}$. $\mathbf{x}^{\boldsymbol{\alpha}} = x_1^{\alpha_1} x_2^{\alpha_2} \cdots x_n^{\alpha_n}$
$c_{\boldsymbol{\alpha}}$	The coefficient for monomial $\mathbf{x}^{\boldsymbol{\alpha}}$
$f(\mathbf{x})$	A polynomial in $\mathbf{x}$. $f(\mathbf{x}) = \sum_{\boldsymbol{\alpha}} c_{\boldsymbol{\alpha}} \mathbf{x}^{\boldsymbol{\alpha}}$.
$\deg(f)$	The degree of a polynomial $f(\mathbf{x})$. $\deg(f) = \max_{\boldsymbol{\alpha}} (\sum_{i=1}^n \alpha_i)$

2.2.1 Nonnegative Polynomials

Nonnegative polynomials are of practical importance in numerous optimization applications. In general, checking whether a given polynomial is nonnegative or not is a hard problem, and no efficient algorithm has been reported to solve this problem [60]. However, if a polynomial $f(\mathbf{x})$ can be represented as a sum of squared polynomials, then $f(\mathbf{x})$ is clearly nonnegative over its domain. For example, it can be easily concluded that $f(x_1, x_2, x_3) = 2x_1^2 + 2x_2^2 + 2x_3^2 - 2x_1x_2 - 2x_2x_3 - 2x_1x_3$ is nonnegative as it can be

expressed as $f(x_1, x_2, x_3) = (x_1 - x_2)^2 + (x_2 - x_3)^2 + (x_3 - x_1)^2$. This expression of $f(\mathbf{x})$ as a sum of squared polynomials acts as a certificate of nonnegativity, which gives an immediate proof of the nonnegativity of $f(\mathbf{x})$. With the development of convex optimization, it has been shown that checking whether a given polynomial has an SOS decomposition, i.e. $f(\mathbf{x})$ can be represented as a sum of squared polynomials, or not is equivalent to solve a semidefinite programming (SDP) problem [60].

A necessary condition for nonnegativity of a polynomial $f(\mathbf{x})$ is that the degree $\deg(f)$ is even. Considering a polynomial $f(\mathbf{x}) = \sum_{\boldsymbol{\alpha}} c_{\boldsymbol{\alpha}} \mathbf{x}^{\boldsymbol{\alpha}}$ with even degree $\deg(f) = 2t,\ t \in \mathbb{Z}_{++}$, $f(\mathbf{x})$ has an SOS decomposition if and only if there is a positive semidefinite matrix $\mathbf{W} \succcurlyeq \mathbf{0}$ such that

$$f(\mathbf{x}) = \mathbf{z}^{\mathrm{T}}(\mathbf{x}) \mathbf{W} \mathbf{z}(\mathbf{x}) = \langle \mathbf{z}(\mathbf{x}) \mathbf{z}^{\mathrm{T}}(\mathbf{x}), \mathbf{W} \rangle \tag{2-4}$$

where $\mathbf{z}(\mathbf{x}) \in \mathbb{R}^{n_{\mathbf{z}}}$ is a vector containing all the base monomials with degree up to t:

$$\mathbf{z}(\mathbf{x}) = (1, x_1, x_2, \cdots, x_n, x_1^2, x_1 x_2, \cdots, x_n^2, \cdots, x_n^t)^{\mathrm{T}} \tag{2-5}$$

According to the theory of combinatorics [61], the number of monomials in n variables with degree up to t is $n_{\mathbf{z}} = \binom{n+t}{n}$. The equality in Eq. (2-4) implies that both sides of the polynomial $\sum_{\boldsymbol{\alpha}} c_{\boldsymbol{\alpha}} \mathbf{x}^{\boldsymbol{\alpha}} = \langle \mathbf{z}(\mathbf{x}) \mathbf{z}^{\mathrm{T}}(\mathbf{x}), \mathbf{W} \rangle$ should have the same coefficient for the same monomial $\mathbf{x}^{\boldsymbol{\alpha}}$. To explicitly describe this coefficient matching condition, a group of matrices $\{\mathbf{A}_{\boldsymbol{\alpha}}\}$ is defined as each matrix $\mathbf{A}_{\boldsymbol{\alpha}} \in \mathbb{R}^{n_{\mathbf{z}} \times n_{\mathbf{z}}}$ being an indicator matrix for monomial $\mathbf{x}^{\boldsymbol{\alpha}}$ in the matrix $\mathbf{z}(\mathbf{x}) \mathbf{z}^{\mathrm{T}}(\mathbf{x})$:

$$(\mathbf{A}_{\boldsymbol{\alpha}})_{\boldsymbol{\beta},\boldsymbol{\gamma}} = \begin{cases} 1 & \text{if } \boldsymbol{\beta}+\boldsymbol{\gamma}=\boldsymbol{\alpha} \\ 0 & \text{if } \boldsymbol{\beta}+\boldsymbol{\gamma}\neq\boldsymbol{\alpha} \end{cases} \tag{2-6}$$

Here the natural ordering of multi-indices $\boldsymbol{\beta} \in \mathbb{Z}_+^n$ and $\boldsymbol{\gamma} \in \mathbb{Z}_+^n$ are used to index the entries of $\mathbf{A}_{\boldsymbol{\alpha}}$. Figure 2-1 illustrates the coefficient matching between $f(\mathbf{x})$ and $\langle \mathbf{z}(\mathbf{x})\mathbf{z}^{\mathrm{T}}(\mathbf{x}), \mathbf{W} \rangle$. As shown in the figure, on the left-hand side of Figure 2-1 (a), the coefficient of monomial $\mathbf{x}^{\boldsymbol{\alpha}}$ in the polynomial $f(\mathbf{x})$ is $c_{\boldsymbol{\alpha}}$; on the right-hand side of Figure 2-1 (a), the coefficient of monomial $\mathbf{x}^{\boldsymbol{\alpha}}$ in the polynomial $\langle \mathbf{z}(\mathbf{x})\mathbf{z}^{\mathrm{T}}(\mathbf{x}), \mathbf{W} \rangle$ is $\sum_{\boldsymbol{\beta}+\boldsymbol{\gamma}=\boldsymbol{\alpha}} \mathbf{W}_{\boldsymbol{\beta},\boldsymbol{\gamma}}$, which can be written as $\langle \mathbf{A}_{\boldsymbol{\alpha}}, \mathbf{W} \rangle$. The indicator matrix $\mathbf{A}_{\boldsymbol{\alpha}}$ indicates the position of monomial $\mathbf{x}^{\boldsymbol{\alpha}}$ in the matrix $\mathbf{z}(\mathbf{x})\mathbf{z}^{\mathrm{T}}(\mathbf{x})$. It is easy to verify that $\mathbf{A}_{\boldsymbol{\alpha}} = \mathbf{A}_{\boldsymbol{\alpha}}^{\mathrm{T}}$, and $\mathbf{A}_{\boldsymbol{\alpha}}$ is sparse. Only a few entries in $\mathbf{A}_{\boldsymbol{\alpha}}$ are one and all the others are zero.

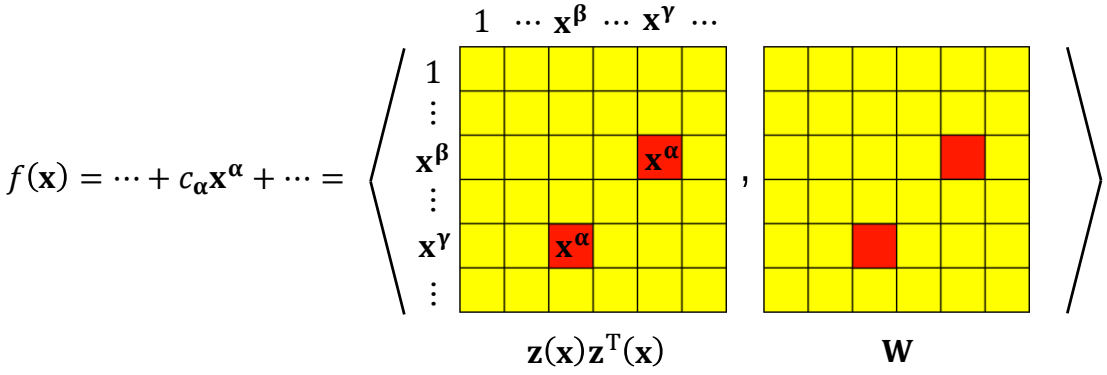

(a) Polynomial $f(\mathbf{x})$

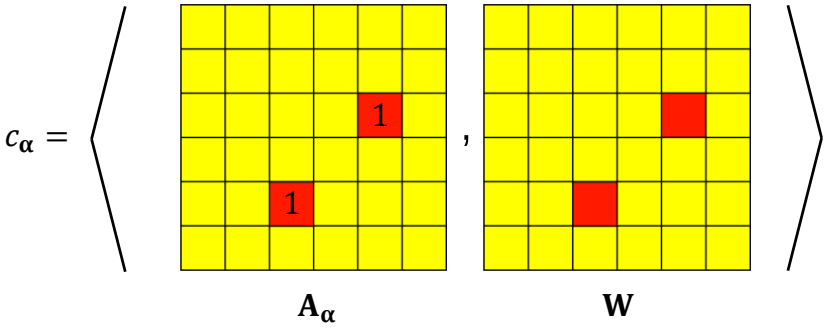

(b) Coefficient $c_{\boldsymbol{\alpha}}$ for monomial $\mathbf{x}^{\boldsymbol{\alpha}}$

Figure 2-1 Coefficient matching

Using the notation shown above, checking whether a given polynomial $f(\mathbf{x})$ has an SOS decomposition can be formulated as a feasibility SDP problem:

$$\begin{aligned} &\text{find} \quad \mathbf{W} \\ &\text{subject to} \quad \langle \mathbf{A}_{\boldsymbol{\alpha}}, \mathbf{W} \rangle = c_{\boldsymbol{\alpha}}, \quad \forall \boldsymbol{\alpha} \text{ in } f(\mathbf{x}) = \textstyle\sum_{\boldsymbol{\alpha}} c_{\boldsymbol{\alpha}} \mathbf{x}^{\boldsymbol{\alpha}} \\ &\mathbf{W} \succcurlyeq \mathbf{0} \end{aligned} \tag{2-7}$$

Example: Consider a polynomial $f(\mathbf{x})$ in $\mathbf{x} = (x_1, x_2)^{\mathrm{T}}$ with degree of $\deg(f) = 2$:

$$f(\mathbf{x}) = 1 + 2x_1 - 4x_2 + 2x_1^2 + 2x_1x_2 + 13x_2^2 \tag{2-8}$$

The polynomial has six monomials. The power index, monomials, and corresponding coefficients are shown below:

Table 2-2 Monomials and coefficients in the polynomial Eq. (2-8)

$\boldsymbol{\alpha}$	(0, 0)	(1, 0)	(0, 1)	(2, 0)	(1, 1)	(0, 2)
$\mathbf{x}^{\boldsymbol{\alpha}}$	1	x_1	x_2	x_1^2	x_1x_2	x_2^2
$c_{\boldsymbol{\alpha}}$	1	2	-4	2	2	13

The base monomial vector $\mathbf{z}(\mathbf{x})$ and the matrix $\mathbf{z}(\mathbf{x})\mathbf{z}^{\mathrm{T}}(\mathbf{x})$ are shown as:

$$\mathbf{z}(\mathbf{x}) = \begin{Bmatrix} 1 \\ x_1 \\ x_2 \end{Bmatrix} \qquad \mathbf{z}(\mathbf{x})\mathbf{z}^{\mathrm{T}}(\mathbf{x}) = \begin{pmatrix} 1 & x_1 & x_2 \\ x_1 & x_1^2 & x_1x_2 \\ x_2 & x_1x_2 & x_2^2 \end{pmatrix}$$

According to Eq. (2-6), the indicator matrices $\{\mathbf{A}_{\boldsymbol{\alpha}}\}$ are shown as:

$$\mathbf{A}_{(0,0)} = \begin{pmatrix} 1 & 0 & 0 \\ 0 & 0 & 0 \\ 0 & 0 & 0 \end{pmatrix} \qquad \mathbf{A}_{(1,0)} = \begin{pmatrix} 0 & 1 & 0 \\ 1 & 0 & 0 \\ 0 & 0 & 0 \end{pmatrix} \qquad \mathbf{A}_{(0,1)} = \begin{pmatrix} 0 & 0 & 1 \\ 0 & 0 & 0 \\ 1 & 0 & 0 \end{pmatrix}$$

$$\mathbf{A}_{(2,0)} = \begin{pmatrix} 0 & 0 & 0 \\ 0 & 1 & 0 \\ 0 & 0 & 0 \end{pmatrix} \qquad \mathbf{A}_{(1,1)} = \begin{pmatrix} 0 & 0 & 0 \\ 0 & 0 & 1 \\ 0 & 1 & 0 \end{pmatrix} \qquad \mathbf{A}_{(0,2)} = \begin{pmatrix} 0 & 0 & 0 \\ 0 & 0 & 0 \\ 0 & 0 & 1 \end{pmatrix}$$

Solving the feasibility problem in Eq. (2-7), the solution is calculated as:

$$\mathbf{W} = \begin{pmatrix} 1 & 1 & -2 \\ 1 & 2 & 1 \\ -2 & 1 & 13 \end{pmatrix}$$

Here the monomial $x_1 x_2$ is used to illustrate the coefficient matching. The monomial has power vector $\boldsymbol{\alpha} = (1,1)$. $\boldsymbol{\beta}$ and $\boldsymbol{\gamma}$ can only take values of $(0,0)$, $(1,0)$, and $(0,1)$. The two possible pairs of $\boldsymbol{\beta}$ and $\boldsymbol{\gamma}$ satisfying $\boldsymbol{\beta} + \boldsymbol{\gamma} = \boldsymbol{\alpha}$ are: (*i*) $\boldsymbol{\beta} = (1,0)$ and $\boldsymbol{\gamma} = (0,1)$; (*ii*) $\boldsymbol{\beta} = (0,1)$ and $\boldsymbol{\gamma} = (1,0)$. The two pairs of $\boldsymbol{\beta}$ and $\boldsymbol{\gamma}$ are then used to construct matrix $\mathbf{A}_{(1,1)}$ as above. Finally, to verify $\langle \mathbf{A}_{\boldsymbol{\alpha}}, \mathbf{W} \rangle = c_{\boldsymbol{\alpha}}$, the coefficient of $x_1 x_2$ in polynomial $\langle \mathbf{z}(\mathbf{x})\mathbf{z}^{\mathrm{T}}(\mathbf{x}), \mathbf{W} \rangle$ is $\langle \mathbf{A}_{(1,1)}, \mathbf{W} \rangle = 2$, which equals the coefficient of $x_1 x_2$ in $f(\mathbf{x})$.

This positive semidefinite matrix $\mathbf{W}$ can be decomposed as $\mathbf{L}^{\mathrm{T}}\mathbf{L}$ by many different decomposition algorithms, such as Cholesky decomposition or eigen decomposition. The Cholesky decomposition provides

$$\mathbf{L} = \begin{pmatrix} 1 & 1 & -2 \\ 0 & 1 & 3 \end{pmatrix}.$$

Thus, the polynomial in Eq. (2-8) can be written as the sum of two squared polynomials:

$$f(\mathbf{x}) = \mathbf{z}^{\mathrm{T}}(\mathbf{x})\mathbf{W}\mathbf{z}(\mathbf{x}) = \big(\mathbf{L}\mathbf{z}(\mathbf{x})\big)^{\mathbf{T}}\big(\mathbf{L}\mathbf{z}(\mathbf{x})\big) = (1 + x_1 - 2x_2)^2 + (x_1 + 3x_2)^2$$

2.2.2 SOS Relaxation of Polynomial Optimization Problems

Consider a general polynomial optimization problem:

$$\begin{aligned} &\underset{\mathbf{x}}{\text{minimize}} \;\; f_0(\mathbf{x}) = \sum\nolimits_{\boldsymbol{\alpha}_0} c_{\boldsymbol{\alpha}_0}\mathbf{x}^{\boldsymbol{\alpha}_0} \\ &\text{subject to} \;\; f_i(\mathbf{x}) = \sum\nolimits_{\boldsymbol{\alpha}_i} c_{\boldsymbol{\alpha}_i}\mathbf{x}^{\boldsymbol{\alpha}_i} \geq 0 \qquad i = 1, 2, \cdots, k \end{aligned} \tag{2-9}$$

where $f_0(\mathbf{x})\colon \mathbb{R}^n \to \mathbb{R}$ and $f_i(\mathbf{x})\colon \mathbb{R}^n \to \mathbb{R}$ are polynomials with degrees of $\deg(f_0)$ and $\deg(f_i)$, respectively. The optimal objective function value of the problem in Eq. (2-9) is denoted as f^*. Finding the optimal objective value $f_0^* = f_0(\mathbf{x}^*)$ can be equivalently reformulated as solving for the maximum lower bound of the function $f_0(\mathbf{x})$ over the feasible set $\boldsymbol{\Omega} = \{\mathbf{x} \in \mathbb{R}^n | f_i(\mathbf{x}) \geq 0, i = 1, 2, \cdots, k\}$:

$$\begin{aligned} &\underset{\gamma}{\text{minimize}} \;\; \gamma \\ &\text{subject to} \;\; f_0(\mathbf{x}) - \gamma \geq 0 \qquad \forall \mathbf{x} \in \boldsymbol{\Omega} \end{aligned} \tag{2-10}$$

The optimization problem in Eq. (2-10) is convex, as the objective function is affine, and the feasible set is defined as an intersection of an infinite number of halfspaces. On the other hand, the constraints in Eq. (2-10) are intractable because there are infinitely many halfspaces involved. To implement the constraints, the SOS decomposition is utilized [62].

A sufficient condition for $f_0(\mathbf{x}) - \gamma \geq 0$ over the feasible set $\mathbf{\Omega}$ is that there exist SOS polynomials $s_0(\mathbf{x})$ and $s_i(\mathbf{x})$, $i = 1, 2, \cdots, k$, satisfying the following SOS decomposition of $f_0(\mathbf{x}) - \gamma$:

$$f_0(\mathbf{x}) - \gamma = s_0(\mathbf{x}) + \sum_{i=1}^{k} s_i(\mathbf{x}) f_i(\mathbf{x}) \tag{2-11}$$

Substituting $f_0(\mathbf{x})$ and $f_i(\mathbf{x})$ from Eq. (2-9), the following equation is obtained

$$\sum_{\boldsymbol{\alpha}_0} c_{\boldsymbol{\alpha}_0} \mathbf{x}^{\boldsymbol{\alpha}_0} - \gamma = s_0(\mathbf{x}) + \sum_{i=1}^{k} s_i(\mathbf{x}) \sum_{\boldsymbol{\alpha}_i} c_{\boldsymbol{\alpha}_i} \mathbf{x}^{\boldsymbol{\alpha}_i} \tag{2-12}$$

The function $f_0(\mathbf{x}) - \gamma$ is then represented as a polynomial with degree of $2t$, where t is the smallest integer satisfying the inequality $2t \geq \max_{i=0,1,\cdots,k} \big(\deg(f_i)\big)$. Here the SOS polynomial $s_0(\mathbf{x})$ has degree of $\deg(s_0) = 2t$ and $s_i(\mathbf{x})$ has degree of $\deg(s_i) = 2e_i$, where e_i is the largest integer satisfying the condition $2e_i \leq 2t - \deg(f_i)$. Indeed, for any $\mathbf{x} \in \mathbf{\Omega}$, nonnegativity of the SOS polynomials implies that $f_0(\mathbf{x}) - \gamma \geq 0$. The indicator matrices $\{\mathbf{A}_{\boldsymbol{\alpha}_0}\}$ and $\{\mathbf{B}_{i,\boldsymbol{\alpha}_0}\}$, $i = 1, 2, \cdots, k$, are introduced for coefficient matching. Recall $\boldsymbol{\alpha}_0$ is the variable index in function $f_0(\mathbf{x})$ and $\boldsymbol{\alpha}_i$ is the variable index in function $f_i(\mathbf{x})$ in Eq. (2-9). Analogous to Eq. (2-6), each $\mathbf{A}_{\boldsymbol{\alpha}_0}$ and each $\mathbf{B}_{i,\boldsymbol{\alpha}_0}$ are defined as:

$$\begin{aligned} \left(\mathbf{A}_{\boldsymbol{\alpha}_0}\right)_{\boldsymbol{\beta},\boldsymbol{\gamma}} &= \begin{cases} 1 & \text{if } \boldsymbol{\beta} + \boldsymbol{\gamma} = \boldsymbol{\alpha}_0 \\ 0 & \text{if } \boldsymbol{\beta} + \boldsymbol{\gamma} \neq \boldsymbol{\alpha}_0 \end{cases} \\ \left(\mathbf{B}_{i,\boldsymbol{\alpha}_0}\right)_{\boldsymbol{\beta},\boldsymbol{\gamma}} &= \begin{cases} c_{\boldsymbol{\alpha}_i} & \text{if } \boldsymbol{\beta} + \boldsymbol{\gamma} + \boldsymbol{\alpha}_i = \boldsymbol{\alpha}_0 \\ 0 & \text{if } \boldsymbol{\beta} + \boldsymbol{\gamma} + \boldsymbol{\alpha}_i \neq \boldsymbol{\alpha}_0 \end{cases} \end{aligned} \tag{2-13}$$

Here the natural ordering of multi-indices $\boldsymbol{\beta}$ and $\boldsymbol{\gamma}$ are used to index the entries of $\mathbf{A}_{\boldsymbol{\alpha}_0}$ and $\mathbf{B}_{i,\boldsymbol{\alpha}_0}$. Representing the inequality constraints in Eq. (2-10), $f_0(\mathbf{x}) - \gamma \geq 0, \forall \mathbf{x} \in \boldsymbol{\Omega}$, through coefficient matching, the optimization problem is then relaxed to an SDP problem with γ, $\mathbf{W}$, and $\mathbf{Q}_i$ as optimization variables:

$$
\begin{aligned}
&\underset{\gamma, \mathbf{W}, \mathbf{Q}_i}{\text{maximize}} \;\; \gamma \\
&\text{subject to} \;\; \langle \mathbf{A}_{\mathbf{0}}, \mathbf{W} \rangle + \sum_{i=1}^{k} \langle \mathbf{B}_{i,\mathbf{0}}, \mathbf{Q}_i \rangle = c_{\mathbf{0}} - \gamma \\
&\qquad \langle \mathbf{A}_{\boldsymbol{\alpha}_0}, \mathbf{W} \rangle + \sum_{i=1}^{k} \langle \mathbf{B}_{i,\boldsymbol{\alpha}_0}, \mathbf{Q}_i \rangle = c_{\boldsymbol{\alpha}_0}, \quad \forall \boldsymbol{\alpha}_0 \neq \mathbf{0} \\
&\qquad \mathbf{W} \succcurlyeq \mathbf{0}, \qquad \mathbf{Q}_i \succcurlyeq \mathbf{0}, \qquad i = 1, 2, \cdots, k.
\end{aligned}
\tag{2-14}
$$

Solving the SDP problem in Eq. (2-14) provides the maximum lower bound γ^* for the original optimization problem in Eq. (2-9). Although in rare cases it is possible that $\gamma^* < f_0^*$, in practical applications, this lower bound achieved by SOS relaxation usually reaches the optimal value of the original optimization problem, i.e. $\gamma^* = f_0^*$ [60].

To summarize the optimization procedure, Figure 2-2 shows the flow chat of the procedure. First, the problem of minimizing a polynomial $f_0(\mathbf{x})$ over a set $\boldsymbol{\Omega} = \{\mathbf{x} \in \mathbb{R}^n | f_i(\mathbf{x}) \geq 0, i = 1, 2, \cdots, k\}$ (Eq. (2-9)) is equivalently reformulated as finding the best lower bound γ^* of $f_0(\mathbf{x})$ over the set $\boldsymbol{\Omega}$ (Eq. (2-10)). Second, the condition that $f_0(\mathbf{x}) - \gamma \geq 0$ over set $\boldsymbol{\Omega}$ is relaxed to a more easily solvable condition that $f_0(\mathbf{x}) - \gamma$ has an SOS decomposition over set $\boldsymbol{\Omega}$ (Eq. (2-14)).

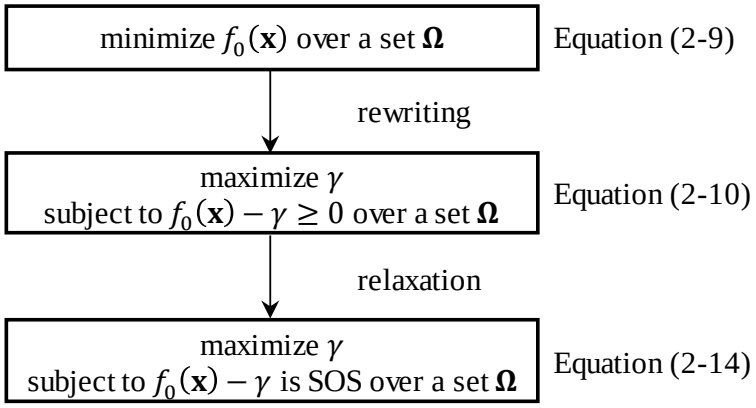

Figure 2-2 Flow chat of the optimization procedure

2.2.3 Minimizer Extraction

To accomplish model updating, only finding the lower bound or the optimal value of the objective function (f_0^*) is not enough. The minimizer of the original optimization problem in Eq. (2-9) can be extracted from the solution of the dual problem of the SDP problem in Eq. (2-14) [63]. Define the dual variables, including Lagrangian multiplier vector $\mathbf{y}$ and matrices $\mathbf{U} \succcurlyeq \mathbf{0}$ and $\mathbf{V}_i \succcurlyeq \mathbf{0}$, $i = 1, 2, \cdots, k$. Here the natural order for the dual variable $\mathbf{y}$ is shown as:

$$\mathbf{y} = \{\mathbf{y}_{\boldsymbol{\alpha}_0}\} = \{y_{(0,0,\cdots,0)}, y_{(1,0,\cdots,0)}, y_{(0,1,\cdots,0)}, \cdots, y_{(0,0,\cdots,1)}, \cdots, y_{(0,0,\cdots,2t)}\}^{\mathrm{T}} \tag{2-15}$$

The Lagrangian for the problem in Eq. (2-14) can be written as:

$$\mathcal{L}(\gamma, \mathbf{W}, \mathbf{Q}_i, \mathbf{y}, \mathbf{U}, \mathbf{V}_i) = \gamma + y_{\mathbf{0}}\left(c_{\mathbf{0}} - \gamma - \langle \mathbf{A}_{\mathbf{0}}, \mathbf{W}\rangle - \sum_{i=1}^{k} \langle \mathbf{B}_{i,\mathbf{0}}, \mathbf{Q}_i\rangle\right)$$

$$+\sum_{\boldsymbol{\alpha}_0\neq\mathbf{0}} y_{\boldsymbol{\alpha}_0}\left(c_{\boldsymbol{\alpha}_0}-\langle\mathbf{A}_{\boldsymbol{\alpha}_0},\mathbf{W}\rangle-\sum_{i=0}^{k}\langle\mathbf{B}_{i,\boldsymbol{\alpha}_0},\mathbf{Q}_i\rangle\right)+\langle\mathbf{U},\mathbf{W}\rangle+\sum_{i=1}^{k}\langle\mathbf{V}_i,\mathbf{Q}_i\rangle$$

$$=\sum_{\boldsymbol{\alpha}_0} c_{\boldsymbol{\alpha}_0} y_{\boldsymbol{\alpha}_0}+\gamma(1-y_{\mathbf{0}})+\left\langle\mathbf{U}-\sum_{\boldsymbol{\alpha}_0} y_{\boldsymbol{\alpha}_0}\mathbf{A}_{\boldsymbol{\alpha}_0},\mathbf{W}\right\rangle \tag{2-16}$$

$$+\sum_{i=1}^{k}\left\langle\mathbf{V}_i-\sum_{\boldsymbol{\alpha}_0} y_{\boldsymbol{\alpha}_0}\mathbf{B}_{i,\boldsymbol{\alpha}_0},\mathbf{Q}_i\right\rangle$$

The dual function is then formulated as the supremum of the Lagrangian with respect to primal variables γ, $\mathbf{W}$, and $\mathbf{Q}_i$. The dual function is found as:

$$\begin{aligned}\mathcal{D}(\mathbf{y},\mathbf{U},\mathbf{V}_i) &= \sup_{\gamma,\mathbf{W},\mathbf{Q}_i}\mathcal{L}(\gamma,\mathbf{W},\mathbf{Q}_i,\mathbf{y},\mathbf{U},\mathbf{V}_i)\\ &=\begin{cases}\sum_{\boldsymbol{\alpha}_0} c_{\boldsymbol{\alpha}_0} y_{\boldsymbol{\alpha}_0} & \text{if } y_{\mathbf{0}}=1,\mathbf{U}=\sum_{\boldsymbol{\alpha}_0} y_{\boldsymbol{\alpha}_0}\mathbf{A}_{\boldsymbol{\alpha}_0},\mathbf{V}_i=\sum_{\boldsymbol{\alpha}_0} y_{\boldsymbol{\alpha}_0}\mathbf{B}_{i,\boldsymbol{\alpha}_0}\\ +\infty & \text{otherwise}\end{cases}\end{aligned} \tag{2-17}$$

Thus, the dual problem of the SDP problem in Eq. (2-14) can be written as:

$$\begin{aligned}&\underset{\mathbf{y}}{\text{minimize}}\ \sum_{\boldsymbol{\alpha}_0} c_{\boldsymbol{\alpha}_0} y_{\boldsymbol{\alpha}_0}\\ &\text{subject to}\ \ y_{\mathbf{0}}=1\\ &\qquad\mathbf{U}=\sum_{\boldsymbol{\alpha}_0} y_{\boldsymbol{\alpha}_0}\mathbf{A}_{\boldsymbol{\alpha}_0}\succcurlyeq\mathbf{0}\\ &\qquad\mathbf{V}_i=\sum_{\boldsymbol{\alpha}_0} y_{\boldsymbol{\alpha}_0}\mathbf{B}_{i,\boldsymbol{\alpha}_0}\succcurlyeq\mathbf{0}\qquad i=1,2,\cdots,k.\end{aligned} \tag{2-18}$$

It has been shown that if $\gamma^*=f^*$, the optimal solution of the dual problem in Eq. (2-18) can be calculated as [64]:

$$\mathbf{y}^* = (1, x_1^*, x_2^*, \cdots, x_n^*, \cdots, (x_n^*)^{2t})^{\mathrm{T}} \tag{2-19}$$

where the entries correspond to the monomials $\mathbf{x}^{\boldsymbol{\alpha}_0}$. Thus, the optimal solution $\mathbf{x}^*$ for the original problem in Eq. (2-9) can be easily extracted from $\mathbf{y}^*$, as the 2nd to the $(n+1)^{\text{th}}$ entries. Since most of the primal-dual interior methods simultaneously solve both the primal and dual problems, the optimal solution $\mathbf{x}^*$ can be computed efficiently.

The SOS optimization method provides the great theoretical advantage of converting a nonconvex polynomial optimization problem into a convex SDP problem. Thus, all the desirable properties of convex problems can be exploited to analyze and solve the problem. However, the size of the SDP problem remains a significant challenge. Recall that there are n optimization variables in the optimization problem in Eq. (2-9). In order to achieve the SOS representation in Eq. (2-14), the degree of SOS polynomial $s_0(\mathbf{x})$ should be $\deg(s_0) = d_0 = 2t$, where t is the smallest integer such that $2t \geq \max_i \deg(f_i)$, $i = 0, 1, 2, \cdots, k$. Similarly, the degree of SOS polynomial $s_i(\mathbf{x})$ should be $\deg(s_i) = d_i = d_0 - e_i$, where e_i is the smallest even integer such that $e_i \geq \deg(f_i)$, $i = 1, 2, \cdots, k$. The sizes of the matrices $\mathbf{W}$ and $\mathbf{Q}_i$ are $\binom{n+d_0}{n} \times \binom{n+d_0}{n}$ and $\binom{n+d_i}{n} \times \binom{n+d_i}{n}$, respectively, and the number of equality constraints in Eq. (2-14) is $\binom{n+2d_0}{n}$ [58]. The size of the SDP problem in Eq. (2-14) can be very large as n and/or d_0 grow, making the problem while theoretically convex, practically difficult to solve. This difficulty necessitates exploring the problem structure to improve the solvability of the SDP problem, which will be addressed in Section 2.3 and Section 2.4.

2.2.4 Numerical Study: Four-Story Shear Structure

To validate the proposed SOS optimization methods for model updating, a four-story shear frame is first simulated (Figure 2-3). In the initial model, the nominal weight and inter-story stiffness values of all floors are set as 12.060 lb and 10 lbf/in, respectively. To construct an "as-built" structure, the stiffness value of the fourth story is reduced by 10% to 9 lbf/in, as shown in Figure 2-3. Modal properties of the "as-built" structure are directly used as "experimental" modal properties. It is assumed that only the first three floors are instrumented with sensors and only the first mode is "measured" and available for model updating. The first resonance frequency and the "measured" (instrumented) three mode shape entries are $\omega_1 = 6.196\,\mathrm{rad/s}$ and $\boldsymbol{\psi}_{\mathcal{M},1} = (0.395, 0.742, 1.000)^{\mathrm{T}}$, respectively. Recalling notations in Eq. (2-3), here $n_{\mathrm{modes}} = 1$.

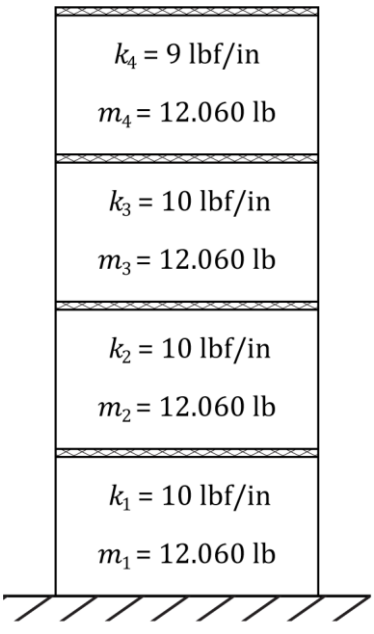

Figure 2-3 Four-story shear frame structure used for SOS optimization

To make 3D graphical illustration possible for the nonconvex objective function, the optimization variables include the stiffness parameter change only of the fourth floor, denoted as θ, and the fourth entry in the mode shape vector, denoted as $\psi_{4,1}$ and abbreviated as ψ_4. Here the variable θ represents the relative change of k_4 from the initial nominal value of 10 lbf/in, i.e. $\theta = (k_4 - 10)/10$. In other words, it is assumed k_1, k_2, and k_3 do not require updating; the change is known to happen with k_4 but need to identify/update how much the change is. The value of ψ_4 is obviously influenced by the previous normalization in $\boldsymbol{\psi}_{\mathcal{M},1}$. With only two optimization variables, θ and ψ_4, the nonconvex objective function can be written as:

$$\begin{aligned} &\underset{\theta,\psi_4}{\text{minimize}} \;\; f_0(\theta,\psi_4) = \left\| [(\mathbf{K}_0 + \theta\mathbf{K}_4) - \omega_1^2\mathbf{M}] \begin{Bmatrix} \boldsymbol{\psi}_{\mathcal{M},1} \\ \psi_4 \end{Bmatrix} \right\|_2^2 \\ &\text{subject to} \;\; f_1(\theta) = (1-\theta)(1+\theta) \geq 0 \end{aligned} \tag{2-20}$$

Figure 2-4 illustrates the nonconvex objective function $f_0(\mathbf{x})$ against the two variables, θ and ψ_4. Figure 2-4 (a) plots the contour of objective function over the feasible set $\{\theta | -1 \leq \theta \leq 1\}$. Here for clarity of the plot, the bound of ψ_4 is set as $-2 \leq \psi_4 \leq 2$ in the plot. The global optimum $\mathbf{x}^* = (\theta^*, \psi_4^*)$ is at $(-0.100, 1.154)$, which corresponds to the "true" values of the two variables, i.e. the ideal solution. Two local optimal points, named as $\mathbf{x}_{\text{GN}} = (-1.000, 0.827)$ and $\mathbf{x}_{\text{TR}} = (-1.000, 0.000)$, locate at the boundary. This contour plot clearly shows that the objective function is nonconvex, especially around the squared region where a saddle point $s = (-0.944, 1.000)$ locates. Figure 2-4 (b) shows the 3D close-up of $f_0(\mathbf{x})$ around the saddle point with the vertical axis as the objective

function value. The figure again demonstrates the nonconvexity of this small model updating problem.

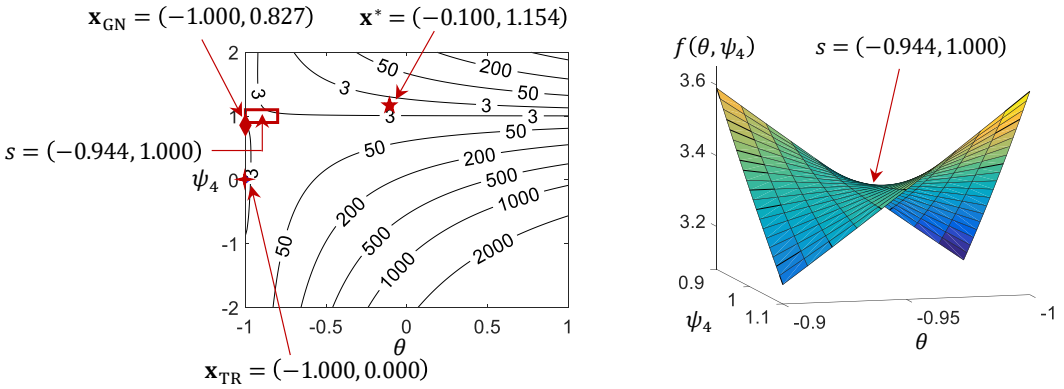

(a) Contour of objective function f_0 over the feasible set

(b) Detailed plot of objective function f_0 around the saddle point

Figure 2-4 Plot of objective function $f_0(\mathbf{x})$, i.e. $f_0(\theta, \psi_4)$

In this example, the SOS optimization method is applied to solve the global optimum of the optimization problem. The nonconvex problem is recast into a convex SDP problem using the formulation in Eq. (2-14), and the dual problem is illustrated in Eq. (2-18). By solving the primal and dual problems, the optimal solutions can be calculated as $\gamma^* = 0.000$ for the primal and $\mathbf{y}^* = (1, -0.100, 1.154, \cdots)$ for the dual. Recalling Eq. (2-19), the optimal solution $\mathbf{x}^*$ for problem (2-20) is now easily extracted as $(-0.100, 1.154)$, which is the same as the global optimum shown in Figure 2-4.

To compare with the SOS optimization method, two local optimization algorithms are adopted to solve the optimization problem. The first local optimization algorithm is Gauss-Newton algorithm for nonlinear least squares problems [65]. Gauss-Newton algorithm is a modified version of Newton algorithm with an approximation of the Hessian matrix by omitting the higher order term. Through the MATLAB command '`lsqnonlin`'

[66], the second algorithm uses trust-region-reflective algorithm [67]. The algorithm heuristically minimizes the objective function by solving a sequence of quadratic subproblems subject to ellipsoidal constraints.

For a nonconvex problem, depending on different search starting points, a local optimization algorithm may converge to different locally optimal points. Table 2-3 summarizes the model updating results calculated by different algorithms. The results show that if the search starting point happens to be close to the saddle point in Figure 2-4 (b), Gauss-Newton algorithm and the trust-region-reflective algorithm converge at boundary points ($\mathbf{x}_{\mathrm{GN}}$ and $\mathbf{x}_{\mathrm{TR}}$, respectively) of the feasible region. The corresponding objective function values are both much larger than $\gamma^* = 0.000$. Only when the starting point happens to be chosen away from the saddle point, the local optimization algorithms can find the global optimum. On the other hand, the SOS optimization method does not require

Table 2-3 Model updating results of the four-story shear structure using SOS optimization method

Optimization algorithms	Starting point			Updated value			Error		Objective function value
		θ	ψ_4		θ	ψ_4	θ	ψ_4	
Gauss-Newton	around s	-0.950	1.000	$\mathbf{x}_{\mathrm{GN}}$	-1.000	0.827	-100%	-28.30%	2.898
	$\mathbf{x}_0$	0.000	0.000	$\mathbf{x}^*$	-0.100	1.154	0.00%	0.00%	0.000
Trust-region-reflective	around s	-0.950	1.000	$\mathbf{x}_{\mathrm{TR}}$	-1.000	0.000	-100%	-100%	1.914
	$\mathbf{x}_0$	0.000	0.000	$\mathbf{x}^*$	-0.100	1.154	0.00%	0.00%	0.000
SOS		–	–	$\mathbf{x}^*$	-0.100	1.154	0.00%	0.00%	0.000

any search starting point on (θ, ψ_4), but recasts the nonconvex problem into a convex optimization problem and reliably reaches the global optimum.

2.3 Exploring Sparsity in the SOS Optimization Method

This section investigates the sparsity in SOS optimization method, which can be utilized to reduce the size of the formulated SDP problems. As discussed in the Section 2.2, the SDP problem formulated by the SOS optimization method can be computationally expensive as the SDP problem enforces the coefficient matching for all monomials $\{\mathbf{x}^{\boldsymbol{\alpha}_0}\}$ in $f_0(\mathbf{x})$. Fortunately, the high sparsity of the polynomials in optimization problem Eq. (2-9) can strongly reduce the overall computation efforts since only a few of monomials in $f_0(\mathbf{x})$ require coefficient matching, thus resulting in a smaller size of optimization variables $\mathbf{W}$ and $\mathbf{Q}_i$ in the SDP problem. A plane truss is simulated, and the results show that the sparse SOS optimization method can save a great amount of computational efforts.

2.3.1 Sparse SOS Optimization Method

In this thesis, we examine a specific sparsity pattern where the polynomial objective function consists of several polynomials only involving a small number of variables. Take the modal dynamic residual formulation in Eq. (2-3) as an example. The total number of optimization variables in Eq. (2-3) is $n_{\boldsymbol{\theta}} + n_u \cdot n_{\text{modes}}$, including the stiffness parameter $\boldsymbol{\theta} \in \mathbb{R}^{n_{\boldsymbol{\theta}}}$ and the unmeasured entries $\boldsymbol{\psi}_{\mathcal{U}} = \left(\boldsymbol{\psi}_{\mathcal{U},1}^{\mathrm{T}}, \boldsymbol{\psi}_{\mathcal{U},2}^{\mathrm{T}}, \cdots, \boldsymbol{\psi}_{\mathcal{U},n_{\text{modes}}}^{\mathrm{T}}\right)^{\mathrm{T}} \in \mathbb{R}^{n_{\mathcal{U}} \cdot n_{\text{modes}} \times 1}$ in the mode shapes. Nevertheless, the objective function r consists of n_{modes} polynomials, each of which involves only $\boldsymbol{\theta} \in \mathbb{R}^{n_{\boldsymbol{\theta}}}$ and $\boldsymbol{\psi}_{\mathcal{U},i} \in \mathbb{R}^{n_{\mathcal{U}}}$. This motivates the representation of each of these n_{modes} polynomials individually in SOS form, so that the

SOS representation does not need to concern the cross terms between $\boldsymbol{\psi}_{\mathcal{U},i}$ and $\boldsymbol{\psi}_{\mathcal{U},j}$, $i \neq j$.

Consider a constrained polynomial optimization problem in which the objective function consists of m number of polynomials:

$$\begin{aligned} &\underset{\mathbf{x}}{\text{minimize}} \;\; f_0(\mathbf{x}) = \sum_{j=1}^{m} f_{0,j}(\mathbf{x}) = \sum_{j=1}^{m} \sum_{\boldsymbol{\alpha}_{0,j}} c_{\boldsymbol{\alpha}_{0,j}} \mathbf{x}^{\boldsymbol{\alpha}_{0,j}} \\ &\text{subject to} \;\; f_i(\mathbf{x}) = \sum_{\boldsymbol{\alpha}_i} c_{\boldsymbol{\alpha}_i} \mathbf{x}^{\boldsymbol{\alpha}_i} \geq 0, \qquad\qquad i = 1, 2, \cdots, k \end{aligned} \tag{2-21}$$

Instead of representing $f_0(\mathbf{x})$ as an SOS directly, each polynomial $f_{0,j}(\mathbf{x})$ is represented as an SOS. Here only the sparsity in the objective function is considered. The condition for $f_0(\mathbf{x}) - \gamma \geq 0$ over the feasible set $\boldsymbol{\Omega}$ is that there exist SOS polynomials $s_{0,j}(\mathbf{x})$, $j = 1, 2, \cdots, m$, and $s_i(\mathbf{x})$, $i = 1, 2, \cdots, k$, satisfying the following SOS decomposition of $f_0(\mathbf{x}) - \gamma$:

$$f_0(\mathbf{x}) - \gamma = \sum_{j=1}^{m} s_{0,j}(\mathbf{x}) + \sum_{i=1}^{k} s_i(\mathbf{x}) f_i(\mathbf{x}) \tag{2-22}$$

Substituting $f_0(\mathbf{x})$ and $f_i(\mathbf{x})$ from Eq. (2-21), the following equation is obtained:

$$\sum_{j=1}^{m} \sum_{\boldsymbol{\alpha}_{0,j}} c_{\boldsymbol{\alpha}_{0,j}} \mathbf{x}^{\boldsymbol{\alpha}_{0,j}} - \gamma = \sum_{j=1}^{m} s_{0,j}(\mathbf{x}) + \sum_{i=1}^{k} s_i(\mathbf{x}) \sum_{\boldsymbol{\alpha}_i} c_{\boldsymbol{\alpha}_i} \mathbf{x}^{\boldsymbol{\alpha}_i} \tag{2-23}$$

As the sparsity in $f_i(\mathbf{x})$ is not considered, the indicator matrices $\{\mathbf{B}_{i,\boldsymbol{\alpha}_0}\}$ corresponding to function $s_i(\mathbf{x})$ are the same as those in Eq. (2-13). The indicator matrices $\{\mathbf{A}_{j,\boldsymbol{\alpha}_0}\}$ corresponding to $s_{0,j}(\mathbf{x})$ are introduced below:

$$\left(\mathbf{A}_{j,\boldsymbol{\alpha}_0}\right)_{\boldsymbol{\beta},\boldsymbol{\gamma}} = \begin{cases} 1 & \text{if } \boldsymbol{\beta}+\boldsymbol{\gamma} = \boldsymbol{\alpha}_0 \\ 0 & \text{if } \boldsymbol{\beta}+\boldsymbol{\gamma} \neq \boldsymbol{\alpha}_0 \end{cases} \tag{2-24}$$

Note that although each polynomial $f_{0,j}(\mathbf{x})$ is represented as an SOS polynomial separately, the equality constraint on coefficient $c_{\boldsymbol{\alpha}_0} = \sum_{j=1}^{m} c_{\boldsymbol{\alpha}_{0,j}}$ should hold for every monomial $\mathbf{x}^{\boldsymbol{\alpha}_0}$ in $f_0(\mathbf{x}) - \gamma$. The SDP problem through the sparse SOS optimization method can be formulated as:

$$\begin{aligned} \underset{\gamma,\mathbf{W}_j,\mathbf{Q}_i}{\text{maximize}} \quad & \gamma \\ \text{subject to} \quad & \sum_{j=1}^{m} \langle \mathbf{A}_{j,\mathbf{0}}, \mathbf{W}_j \rangle + \sum_{i=1}^{k} \langle \mathbf{B}_{i,\mathbf{0}}, \mathbf{Q}_i \rangle = c_{\mathbf{0}} - \gamma \\ & \sum_{j=1}^{m} \langle \mathbf{A}_{j,\boldsymbol{\alpha}_0}, \mathbf{W}_j \rangle + \sum_{i=1}^{k} \langle \mathbf{B}_{i,\boldsymbol{\alpha}_0}, \mathbf{Q}_i \rangle = c_{\boldsymbol{\alpha}_0}, \qquad \forall \boldsymbol{\alpha}_0 \neq \mathbf{0} \\ & \mathbf{W}_j \succcurlyeq \mathbf{0}, \quad j = 1, 2, \cdots, m \\ & \mathbf{Q}_i \succcurlyeq \mathbf{0}, \quad i = 1, 2, \cdots, k \end{aligned} \tag{2-25}$$

The dual problem of Eq. (2-25) can be formulated in the similar way as shown in Section 2.2.3, and the minimizer of Eq. (2-21) can be extracted from the solution of the dual problem. Exploring sparsity can effectively reduce the overall computational efforts of the SOS optimization method. To further improve the computational efficiency, the size of the formulated SDP problem Eq. (2-25) can be reduced more using the method introduced in Section 2.4.

2.3.2 Numerical Study: Plane Truss Structure

To validate the proposed sparse SOS optimization method for structural model updating, a plane truss structure is simulated (Figure 2-5). The truss model has 10 nodes, and each node has a vertical and a horizontal DOF. All member cross-sectional areas are set as 8×10^{-5} m^2, and the material density is set as 7,849 kg/m^3. Flexible support conditions are considered in this structure. Vertical and horizontal springs (k_1 and k_2) are allocated at the left support, while a vertical spring (k_3) is allocated at the right support. The Young's moduli of the truss bars are divided into three groups, including E_1 of the top-level truss bars, E_2 of the diagonal and vertical truss bars, and E_3 of the bottom-level truss bars. The mechanical properties of the structure are summarized in Table 2-4, including the initial/nominal values and the "as-built"/actual values.

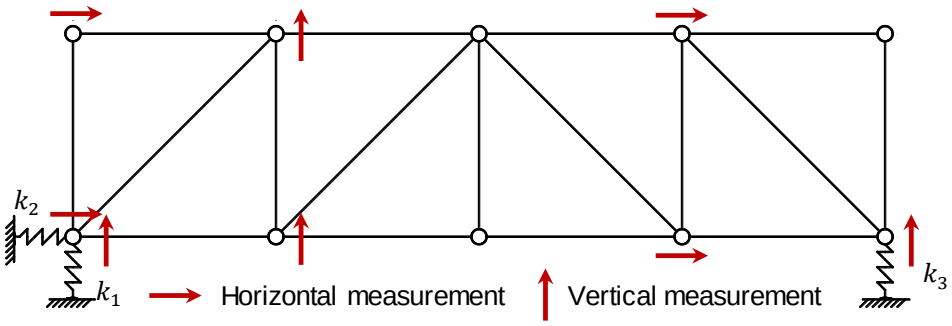

Figure 2-5 Plane truss structure with 8 DOFs measured

Table 2-4 Model updating parameters of the plane truss structure

Property		Initial/Nominal	"As-built"/Actual	Ideal updating result for θ_i
Young's moduli ($\times 10^{11}$ N/m^2)	Top (E_1)	2	2.2	0.100
	Diagonal & Vertical (E_2)	2	1.8	−0.100
	Bottom (E_3)	2	1.9	−0.050
Springs ($\times 10^6$ N/m)	k_1	6	7	0.167
	k_2	6	3	−0.500
	k_3	6	5	−0.167

In this study, modal properties of the "as-built" structure are directly used as "experimental" properties. It is assumed that eight DOFs are measured by sensors, as illustrated in Figure 2-5. Mode shapes extracted from the "experimental" data are only available at these eight measured DOFs. Furthermore, it is assumed that only the first two modes (associated with the two lowest resonance frequencies) are available for model updating. Figure 2-6 shows the first two resonance frequencies and mode shapes of the plane truss structure.

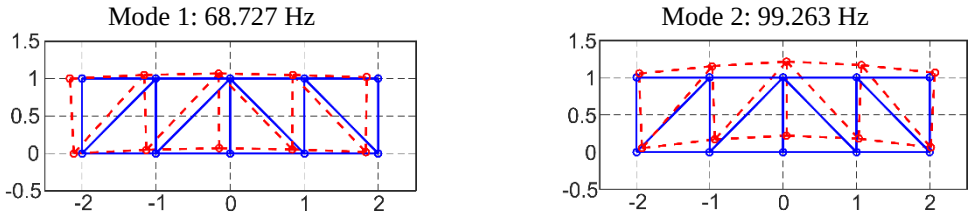

Figure 2-6 Modal properties of the plane truss structure for the 1st and 2nd modes

Six stiffness parameters $\boldsymbol{\theta} \in \mathbb{R}^6$ are updated, including three Young's moduli in the structure (E_1, E_2, and E_3) and the spring stiffness values (k_1, k_2, and k_3). The ideal updating result for each θ_i is shown in the last column of Table 2-4. The lower bound for $\boldsymbol{\theta}$ is set as $\mathbf{L} = -\mathbf{1}_{6\times 1}$ and the upper bound is set as $\mathbf{U} = \mathbf{1}_{6\times 1}$. The bounds effectively restrict the variation range of the stiffness parameters as $\pm$100%. In total, $n_u = 12$ DOFs of the structure are unmeasured. As per Eq. (2-3), all unmeasured entries in the two available mode shapes, $\boldsymbol{\psi}_{\mathcal{U}} = \begin{Bmatrix} \boldsymbol{\psi}_{\mathcal{U},1} \\ \boldsymbol{\psi}_{\mathcal{U},2} \end{Bmatrix} \in \mathbb{R}^{24}$, are treated as optimization variables together with $\boldsymbol{\theta}$. The total number of optimization variables is $n = n_{\boldsymbol{\theta}} + n_{\text{modes}} \cdot n_{\mathcal{U}} = 6 + 2 \times 12 = 30$. To minimize the modal dynamic residual r, the model updating problem can be formulated as follows with optimization variables $\mathbf{x} = (\boldsymbol{\theta}, \boldsymbol{\psi}_{\mathcal{U}})$.

$$\begin{aligned} &\underset{\boldsymbol{\theta},\, \boldsymbol{\psi}_{\mathcal{U}}}{\text{minimize}} \;\; f_0(\boldsymbol{\theta},\, \boldsymbol{\psi}_{\mathcal{U}}) = \sum_{j=1}^{2} \left\| \left[\mathbf{K}(\boldsymbol{\theta}) - \omega_j^2 \mathbf{M}\right] \begin{Bmatrix} \boldsymbol{\psi}_{\mathcal{M},j} \\ \boldsymbol{\psi}_{\mathcal{U},j} \end{Bmatrix} \right\|_2^2 \\ &\text{subject to} \;\; f_i(\theta_i) = 1 - \theta_i^2 \geq 0, \qquad i = 1, 2, \cdots, 6 \end{aligned} \tag{2-26}$$

Using the standard SOS optimization method, the nonconvex problem in Eq. (2-26) is recast into an equivalent convex SDP problem Eq. (2-14). In the SDP problem, optimization variables γ, $\mathbf{W}$, $\mathbf{Q}_i$ $(i = 1, \cdots, 6)$ are introduced. The variable γ is a scalar. With $d = 2t = 4$ and $n = 30$, the size of variable $\mathbf{W}$ is $\binom{n+t}{n} \times \binom{n+t}{n} = \binom{30+2}{30} \times \binom{30+2}{30} = 496 \times 496$. Recall in SOS decomposition Eq. (2-12), e_i is the largest integer satisfying the condition $2e_i \leq 2t - \deg(f_i)$. In this example, with $e_i = 1$, the size of variable $\mathbf{Q}_i$ is $\binom{n+t-e_i}{n} \times \binom{n+t-e_i}{n} = \binom{30+2-1}{30} \times \binom{30+2-1}{30} = 31 \times 31$.

In addition, coefficient matching generates $\binom{n+d}{n} = \binom{30+4}{30} = 46{,}376$ linear equality constraints. It took 457h-16min-49s to solve this SDP problem formulated by the standard SOS optimization method on a computing clusters using 16 CPUs and 84.56 GB RAM memory [68].

The sparse SOS optimization method Eq. (2-25) can significantly reduce the computation load. The objective function of problem in Eq. (2-26) consists of two polynomials, each of which contains updating parameters $\boldsymbol{\theta}$ and unmeasured entries in the mode shape $\boldsymbol{\psi}_{\mathcal{U},j}$, $j = 1, 2$. Each polynomial has $n_j = 18$ variables and degree of $d_j = 2t_j = 4$. Applying the sparse SOS approach, the nonconvex problem in Eq. (2-26) can be recast into an equivalent convex SDP problem, with optimization variables γ, $\mathbf{W}_j$ $(j = 1, 2)$, and $\mathbf{Q}_i$ $(i = 1, \cdots, 6)$. The variables γ and $\mathbf{Q}_i$ $(i = 1, \cdots, 6)$ share the same size as those produced by the SOS approach. With $d_j = 2t_j = 4$ and $n_j = 18$, the size of variable $\mathbf{W}_j$ is $\binom{n_j + t_j}{n_j} \times \binom{n_j + t_j}{n_j} = \binom{18+2}{18} \times \binom{18+2}{18} = 190 \times 190$. The coefficient matching also generates $\binom{n+d}{n} = \binom{30+4}{30} = 46{,}376$ linear equality constraints. Solving the SDP problem formulated by the sparse SOS approach took 3h-13min-14s on the same computing cluster [68]. Comparing to the standard SOS optimization method, the sparse SOS method can effectively improve the computational efficiency.

Table 2-5 briefly summarizes the problem size of the standard and sparse SOS methods applied on model updating of plane truss structure. It is shown that the sparse SOS optimization method can effectively reduce the problem size and improve computational efficiency.

Table 2-5 Problem size of the standard and sparse SOS optimization methods

	Size of $\mathbf{W}_j$	# of $\mathbf{W}_j$	Size of $\mathbf{Q}_i$	# of $\mathbf{Q}_i$	Computation time
Standard SOS	496×496	1	31×31	6	457h-16min-49s
Sparse SOS	190×190	2	31×31	6	3h-13min-14s

Table 2-8 summarizes the updating results obtained from the standard and sparse SOS methods. Both approaches can solve the model updating problem with acceptable accuracy.

Table 2-6 Updating results for the plane truss structure with the first 2 modes measured at 8 DOFs

Variables	Ideal updating results $\boldsymbol{\theta}^*$	Standard SOS $\boldsymbol{\theta}^*_{\mathrm{SOS}}$	Sparse SOS $\boldsymbol{\theta}^*_{\mathrm{SpSOS}}$
θ_1	0.100	0.099	0.099
θ_2	−0.100	−0.101	−0.101
θ_3	−0.050	−0.051	−0.051
θ_4	0.167	0.165	0.166
θ_5	−0.500	−0.501	−0.500
θ_6	−0.167	−0.168	−0.167

2.4 Facial Reduction for Regularizing SDP Problems

This section describes the facial reduction technique for regularizing SDP problems which fail the Slater condition qualification. Although effectiveness of SOS optimization

methods on global optimality has been demonstrated, it turns out that the formulated SDP problems may fail to satisfy the Slater condition (strict feasibility), which plays an important role in the convergence of most interior-point solvers [33]. The failure to satisfy the Slater condition increases the difficulty of finding the optimal solution of the SDP problem using numerical algorithms. Facial reduction technique is one of the methods to overcome this challenge. The technique restricts such an SDP problem onto a feasible set with lower dimension and yields an equivalent SDP problem for which there are strictly feasible points. The smaller equivalent SDP can then be solved by a numerical solver in a more stable manner.

Facial reduction technique is first introduced with emphasis on a practical algorithm which only inspects constraints of SDP problems. Next, this algorithm is shown to be applicable to the SDP problems arising from modal dynamic residual formulation. Finally, simulation on a plane truss structure demonstrates that the facial reduction technique can efficiently reduce the size of the formulated SDP problems. This technique enable SOS optimization method to solve model updating problems of larger-scale structures.

2.4.1 Facial Reduction

Further improvement in computational efficiency for SOS optimization methods can be achieved by tackling the redundancy resulted from the failure of the Slater condition (strict feasibility), i.e., when there is no feasible positive definite matrices $\mathbf{W}_j \succ \mathbf{0}$ and $\mathbf{Q}_i \succ \mathbf{0}$ for the SDP problems in Eq. (2-14) and Eq. (2-25). When the Slater condition fails for the SDP problem, SDP solvers, especially those based on the interior-point methods,

often struggle to find the optimal point. For simplicity of discussion, the standard primal form of an SDP problem with $\mathbf{C} \in \mathbb{S}^n$ and $\mathbf{A}_i \in \mathbb{S}^n$ is considered:

$$\begin{aligned} &\underset{\mathbf{X}}{\text{minimize}} \ \langle \mathbf{C}, \mathbf{X} \rangle \\ &\text{subject to} \ \langle \mathbf{A}_i, \mathbf{X} \rangle = b_i \qquad i = 1, 2, \cdots, k \\ &\mathbf{X} \succcurlyeq \mathbf{0} \end{aligned} \tag{2-27}$$

The initial step of an interior-point method is finding a strictly feasible point, a positive definite matrix for the SDP problem. If there is no strictly feasible point, i.e. there is no $\mathbf{X} \succ \mathbf{0}$ that satisfies $\langle \mathbf{A}_i, \mathbf{X} \rangle = b_i$, $i = 1, 2, \cdots, k$, the Slater condition qualification fails. As a result, slight perturbation can make the SDP problem infeasible, which increases the difficulty for the numerical algorithms solving the problem. In this case, several techniques can be applied to reformulate SDP problems which fail the Slater condition qualification, such as using the homogeneous self-dual embedding method [69]. Here the facial reduction technique is applied to regularize the SDP problems. The idea of facial reduction is to reformulate the SDP problem onto a feasible domain with lower dimension. Thus, the equivalent SDP problem is not only more robust for numerical algorithms to solve but also smaller in size.

Let $\mathbb{C} \subseteq \mathbb{R}^n$ be a convex set. A subset $\mathbb{F} \subseteq \mathbb{C}$ is called a face of $\mathbb{C}$, if and only if

$$\text{For any } \mathbf{X}, \mathbf{Y} \in \mathbb{C} \text{ such that } \frac{\mathbf{X} + \mathbf{Y}}{2} \in \mathbb{F}, \qquad \mathbf{X}, \mathbf{Y} \in \mathbb{F} \text{ holds.}$$

A face $\mathbb{F}$ is a proper face if it is non-empty and not equal to $\mathbb{C}$. Figure 2-7 shows examples of proper faces of two convex sets. In Figure 2-7(a), the edge OA is a proper face of the convex set in $\mathbb{R}^2$. In Figure 2-7(b), both the edge OA and facet OBC are proper faces of the convex set in $\mathbb{R}^3$.

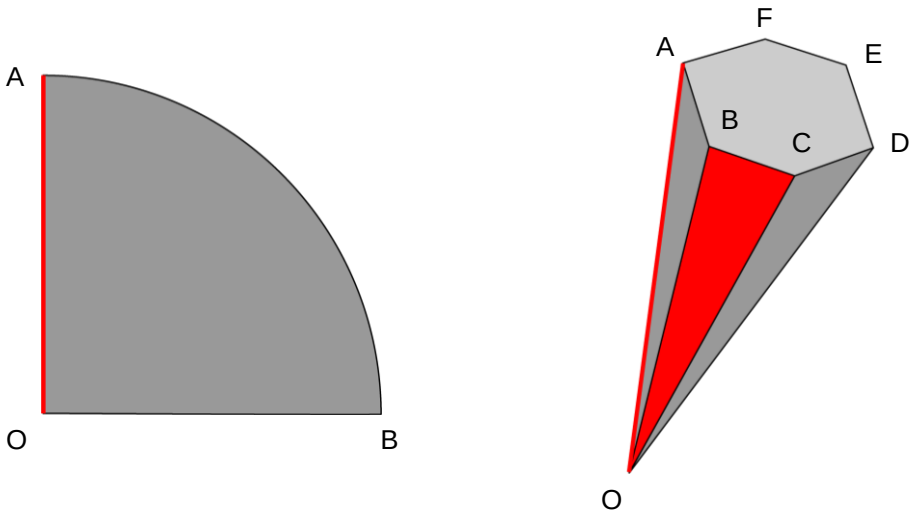

(a) Convex set in $\mathbb{R}^2$ (b) Convex set in $\mathbb{R}^3$

Figure 2-7 Proper faces of convex sets

The feasible set of the SDP problem in Eq. (2-27) can be described by the intersection of an affine subspace $\mathcal{A} = \{\mathbf{X} \in \mathbb{S}^n | \langle \mathbf{A}_i, \mathbf{X} \rangle = b_i, i = 1, 2, \cdots, k\}$ with the semidefinite cone $\mathbb{S}_+^n$. If this SDP problem is feasible but not strictly feasible, it can be reformulated as an optimization problem over a lower dimensional face (proper face) of $\mathbb{S}_+^n$ [70, 71].

Facial reduction algorithms were first proposed for general conic programming (CP) problems and later found many applications in SDP problems. The goal of facial reduction algorithms is to reformulate an SDP problem as one over the proper face with lower dimension. In the cases of semidefinite problems, finding the proper face containing the feasible set can be achieved by solving a sequence of SDP subproblems, which may be as

difficult as solving the original SDP problem. To address these issues, here an alternative approach is adopted to achieve facial reduction by simply inspecting the constraints of the SDP problem [72].

Example: Consider an SDP problem:

$$\begin{aligned} &\underset{x_1,x_2,x_3}{\text{minimize}} \ \left\langle \begin{pmatrix} 0 & 1 \\ 1 & 1 \end{pmatrix}, \begin{pmatrix} x_1 & x_2 \\ x_2 & x_3 \end{pmatrix} \right\rangle \\ &\text{subject to} \ \left\langle \begin{pmatrix} 1 & 0 \\ 0 & 0 \end{pmatrix}, \begin{pmatrix} x_1 & x_2 \\ x_2 & x_3 \end{pmatrix} \right\rangle = 0 \\ &\begin{pmatrix} x_1 & x_2 \\ x_2 & x_3 \end{pmatrix} \succcurlyeq \mathbf{0} \end{aligned} \tag{2-28}$$

The equality constraint requires that $x_1 = 0$. The positive semidefinite matrix $\mathbf{X} = \begin{pmatrix} x_1 & x_2 \\ x_2 & x_3 \end{pmatrix} \succcurlyeq \mathbf{0}$ requires that $x_1 x_3 \geq x_2^2$, and thus $x_2 = 0$. As $\mathbf{X} = \begin{pmatrix} 0 & 0 \\ 0 & x_3 \end{pmatrix}$ is not positive definite no matter what value x_3 takes, the Slater condition (strict feasibility) qualification fails. This SDP problem in Eq. (2-28) can then be reformulated as a regularized SDP problem with lower dimension. In this simple example, the SDP problem degenerates to a linear programming (LP) problem, a special case of SDP problems. Compared to the SDP problem in Eq. (2-28), the following equivalent problem is regularized and smaller in size.

$$\begin{aligned} &\underset{x_3}{\text{minimize}} \ x_3 \\ &\text{subject to} \ x_3 \geq 0 \end{aligned} \tag{2-29}$$

Geometrically, an SDP problem in Eq. (2-27) minimizes an affine function $\langle \mathbf{C}, \mathbf{X} \rangle$ over an intersection between an affine subspace (defined by linear equalities $\langle \mathbf{A}_i, \mathbf{X} \rangle = b_i$, $i = 1, 2, \cdots, k$) and a positive semidefinite cone $\mathbf{X} \succcurlyeq \mathbf{0}$. Figure 2-8 illustrates the feasible set of the SDP example in Eq. (2-28). The intersection of the affine subspace $x_1 = 0$ and the positive semidefinite cone $\mathbf{X} \succcurlyeq \mathbf{0}$ is one proper face of the positive semidefinite cone. The proper face is described simply as $x_3 \geq 0$, i.e. a halfline in this $\mathbb{R}^3$ space.

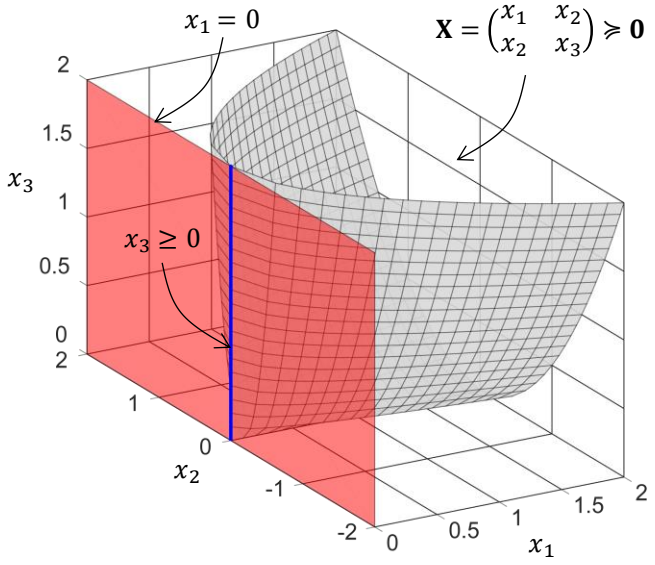

Figure 2-8 Feasible set of the SDP example in Eq. (2-28)

This example motivates and illustrates the approach to achieve facial reduction by inspecting the constraints of the SDP problem. This facial reduction approach is based on the property of a positive semidefinite matrix $\mathbf{X}$ whose leading principal minors are all nonnegative. For the *i*-th linear equality constraint $\langle \mathbf{A}_i, \mathbf{X} \rangle = b_i$, it is first checked whether the following equivalent form can be obtained by permutating rows and columns of matrices $\mathbf{A}_i$ and $\mathbf{X}$:

$$\left\langle \begin{pmatrix} \mathbf{D}_i & \mathbf{0} \\ \mathbf{0} & \mathbf{0} \end{pmatrix}, \begin{pmatrix} \mathbf{X}_{11} & \mathbf{X}_{12} \\ \mathbf{X}_{21} & \mathbf{X}_{22} \end{pmatrix} \right\rangle = b_i', \qquad \text{with } \mathbf{D}_i \succ \mathbf{0} \text{ and } b_i' = b_i \text{ or } b_i' = -b_i. \tag{2-30}$$

If $b_i' > 0$, no facial reduction can be performed according to this constraint. If $b_i' = 0$, $\mathbf{X}_{11}$ has to be a zero matrix. Therefore, this redundant constraint can be eliminated, and all the rows and columns of $\mathbf{X}$ corresponding to the nullified variable $\mathbf{X}_{11}$ can be deleted, together with the corresponding rows and columns in other matrices $\mathbf{A}_j$, $j \neq i$. Note that if b_i' is found to be negative, then it can be concluded that the SDP problem is infeasible as there is no such positive semidefinite matrix $\mathbf{X}$ satisfying this constraint. The idea of inspecting constraints to achieve facial reduction is proposed by Zhu, *et al.* [72]. This facial reduction technique is named as Sieve-SDP, since a sieve-like structure is finally obtained as the rows and columns are eliminated in the matrices $\mathbf{X}$ and $\mathbf{A}_i$. The implementation of the Sieve-SDP algorithm is available as public domain software `SieveSDP` [72], and this facial reduction technique is applied to SDP problems arising from modal dynamic residual formulation.

2.4.2 SDP Problems Arising from Modal Dynamic Residual Formulation

Consider the original model updating problem in Eq. (2-3), the objective in general is a 4-*th* order polynomial, and the monomials with degree of 4 are the cross terms $\theta_i^2 \psi_{u,j}^2$, $u \in \mathcal{U}$. The standard SOS optimization method in Eq. (2-14) generates an SDP problem with redundant constraints. For example, consider coefficient matching equality constraint for monomial $\psi_{u,j}^4$ which does not exist in the objective function. For simplicity in discussion, the index of this monomial is denoted as $\boldsymbol{\alpha}_0 = (\mathbf{0}, 4, \mathbf{0})$, which means that only the power of $\psi_{u,j}$ is 4 and others are 0.

$$\mathbf{x} = (\ \theta_1, \cdots \theta_{n_{\boldsymbol{\theta}}}, \psi_{u_1,1}, \cdots \psi_{u,j}, \cdots \psi_{u_{n_u},n_{\text{mode}}}\ )^{\text{T}}$$

$$\boldsymbol{\alpha}_0 = (\ 0, \ \cdots \ 0, \quad 0, \quad \cdots \ 4, \ \cdots \quad 0 \quad)^{\text{T}}$$

As there is no $\psi_{u,j}^4$ in the objective function $f_0(\mathbf{x})$, the corresponding coefficient $c_{(\mathbf{0},4,\mathbf{0})} = 0$. From coefficient matching in the standard SOS optimization method, the indicator matrix for monomial $\psi_{u,j}^4$ has only one non-zero entry:

$$\mathbf{A}_{(\mathbf{0},4,\mathbf{0})} = \begin{pmatrix} 0 & \cdots & 0 & \cdots & 0 \\ \vdots & \ddots & \vdots & \ddots & \vdots \\ 0 & \cdots & 1 & \cdots & 0 \\ \vdots & \ddots & \vdots & \ddots & \vdots \\ 0 & \cdots & 0 & \cdots & 0 \end{pmatrix}.$$

Meanwhile, the model updating problem in Eq. (2-3) only incorporates bounds on $\boldsymbol{\theta}$, and the bounds can be equivalently rewritten as polynomials $f_i(\mathbf{x}) = (\theta_i - L_i)(U_i - \theta_i) \geq 0$. Since $\sum_{i=1}^{n_{\boldsymbol{\theta}}} s_i(\mathbf{x}) f_i(\mathbf{x})$ as in the right-hand side of Eq. (2-11) cannot produce monomial $\psi_{u,j}^4$, all the indicator matrices $\mathbf{B}_{i,(\mathbf{0},4,\mathbf{0})} = \mathbf{0}$. Thus, the coefficient matching equality constraint in Eq. (2-14) for monomial $\psi_{u,j}^4$ is $\langle \mathbf{A}_{(\mathbf{0},4,\mathbf{0})}, \mathbf{W} \rangle = 0$. By Eq. (2-30), the constraint is redundant and can be eliminated; the corresponding diagonal entry in the matrix variable $\mathbf{W}$ should be zeroed out.

The sparse SOS optimization method through Eq. (2-25) generates similar redundancy. When representing the objective function as n_{modes} number of SOS polynomials, only the *j*-th polynomial contains the monomial $\psi_{u,j}^4$. This fact implies that the indicator matrices in Eq. (2-25) are:

$$\mathbf{A}_{j,(\mathbf{0},4,\mathbf{0})} = \begin{pmatrix} 0 & \cdots & 0 & \cdots & 0 \\ \vdots & \ddots & \vdots & \ddots & \vdots \\ 0 & \cdots & 1 & \cdots & 0 \\ \vdots & \ddots & \vdots & \ddots & \vdots \\ 0 & \cdots & 0 & \cdots & 0 \end{pmatrix} \qquad \text{and} \qquad \mathbf{A}_{p,(\mathbf{0},4,\mathbf{0})} = \mathbf{0}, \qquad p \neq j.$$

The indicator matrix corresponding to $s_i(\mathbf{x})$ is $\mathbf{B}_{i,(\mathbf{0},4,\mathbf{0})} = \mathbf{0}$ for the same reason as the standard SOS optimization method. Thus, the coefficient matching equality constraint in Eq. (2-25) for monomial $\psi_{u,j}^4$ is $\langle \mathbf{A}_{j,(\mathbf{0},4,\mathbf{0})}, \mathbf{W}_j \rangle = 0$, which is redundant and can be eliminated. The corresponding entry in matrix variable $\mathbf{W}_j$ should be zeroed out.

2.4.3 Numerical Study: Plane Truss Structure

To validate the facial reduction technique for reducing the size of the SDP problems, the same model updating problem Eq. (2-26) is solved by the standard and sparse SOS optimization methods with facial reduction technique.

The facial reduction technique is first applied to the SDP problem Eq. (2-14) formulated by the standard SOS optimization method. The size of variable $\mathbf{W}$ is reduced to 196×196, about 40% of the original size. The size of variable $\mathbf{Q}_i$ is not changed, remaining as 31×31. As a result, the number of linear equality constraints is reduced to 10,626, about 22% of the original number of 46,376. It took only 1h-55min to solve this SDP problem regularized by the facial reduction technique on the same computing cluster.

The facial reduction technique is again applied to the SDP problem Eq. (2-25) formulated by the sparse SOS optimization method. The size of variable $\mathbf{W}_j$ is reduced to 112×112, about 60% as the original size. The size of variable $\mathbf{Q}_i$ is not changed, remaining as 31×31. The number of the linear equality constraints is reduced to 7,602,

about 16% of the original number of 46,376. It took only 10min-53s to solve this SDP problem regularized by the facial reduction algorithm on the same computing cluster.

Table 2-7 briefly summarizes the problem size of the standard and sparse SOS methods with facial reduction technique applied on this model updating problem. Comparing to the computation loads without applying facial reduction technique shown in Table 2-5, the facial reduction technique can significantly save the computation time as it regularizes the formulated SDP problems into ones with smaller size

Table 2-7 Problem size of the SOS optimization methods with facial reduction

	Size of $\mathbf{W}_j$	# of $\mathbf{W}_j$	Size of $\mathbf{Q}_i$	# of $\mathbf{Q}_i$	Computation time
Standard SOS with facial reduction	196×196	1	31×31	6	1h-55min-0s
Sparse SOS with facial reduction	112×112	2	31×31	6	10min-53s

Table 2-8 summarizes the updating results obtained from the standard and sparse SOS methods with facial reduction technique. Both approaches can solve the model updating problem with acceptable accuracy. The updating results slightly deviate from the ideal updating results $\boldsymbol{\theta}^*$. These numerical inaccuracies of the SDP solutions are inevitable as the problems are solved on double precision floating point SDP solvers [73, 74]. To further refine the updating results, the data processing method proposed in [75] is adopted. The identified parameters from the SDP solutions are used as the initial points and the function `lsqnonlin` in MATLAB Optimization Toolbox [66] is applied to solve the problem in Eq. (2-26). It can be verified that the SDP solutions serve as good starting

points, and the model updating results from the local optimization solver reach the global optimal solution.

Table 2-8 Updating results for the plane truss structure using facial reduction technique

Variables	Ideal updating results $\boldsymbol{\theta}^*$	Standard SOS with facial reduction $\boldsymbol{\theta}^*_{\mathrm{FR}}$	Sparse SOS with facial reduction $\boldsymbol{\theta}^*_{\mathrm{SpFR}}$
θ_1	0.100	0.096	0.097
θ_2	−0.100	−0.100	−0.102
θ_3	−0.050	−0.051	−0.052
θ_4	0.167	0.164	0.164
θ_5	−0.500	−0.500	−0.501
θ_6	−0.167	−0.166	−0.168

In practice, incorporating more experimental modes in model updating usually provides better updating results. However, for SOS approaches, utilizing more modes introduces more optimization variables and makes the SDP problems more difficult to solve. With the help of facial reduction, such unsolvable problems can be simplified to be solvable again. To study this issue, we now assume that the first five modes are available for model updating. Modal properties of the first two modes are already shown in Figure 2-6. Resonance frequencies and mode shapes of the third to the fifth modes are consequently shown in Figure 2-9.

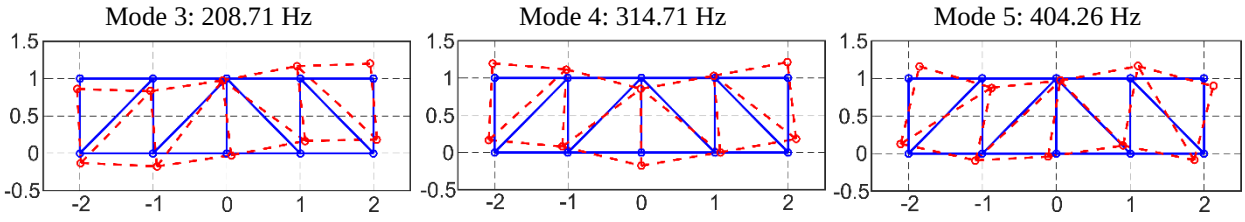

Figure 2-9 Modal properties of the plane truss structure for the 3rd, 4th, and 5th modes

The same stiffness updating variables, $\boldsymbol{\theta} \in \mathbb{R}^6$ corresponding to three Young's moduli in the structure (E_1, E_2, and E_3) and the spring stiffness values (k_1, k_2, and k_3), are updated through the optimization process. To formulate the optimization problem, all unmeasured entries in the five available mode shapes, $\boldsymbol{\psi}_{\mathcal{U}} = \left\{\boldsymbol{\psi}_{\mathcal{U},1}^{\mathrm{T}}, \boldsymbol{\psi}_{\mathcal{U},2}^{\mathrm{T}}, \boldsymbol{\psi}_{\mathcal{U},3}^{\mathrm{T}}, \boldsymbol{\psi}_{\mathcal{U},4}^{\mathrm{T}}, \boldsymbol{\psi}_{\mathcal{U},5}^{\mathrm{T}}\right\}^{\mathrm{T}} \in \mathbb{R}^{60}$, are treated as optimization variables together with $\boldsymbol{\theta}$. The total number of optimization variables is $n = n_{\boldsymbol{\theta}} + n_{\mathrm{modes}} \cdot n_{\mathcal{U}} = 6 + 5 \times 12 = 66$, which is notably higher than the example shown in the previous section. The same lower bound and upper bound for $\boldsymbol{\theta}$ are adopted, and the optimization problem can be formulated in a similar way as shown in Eq. (2-26).

Previous discussion indicates that the sparse SOS approach with facial reduction is the most efficient method to solve the FE model updating problem. For this problem, there are five polynomials of $\left\| \left[\mathbf{K}(\boldsymbol{\theta}) - \omega_j^2 \mathbf{M}\right] \begin{Bmatrix} \boldsymbol{\psi}_{\mathcal{M},j} \\ \boldsymbol{\psi}_{\mathcal{U},j} \end{Bmatrix} \right\|_2^2$ in the objective function, each of which involves updating parameters $\boldsymbol{\theta}$ and unmeasured entries in the mode shape $\boldsymbol{\psi}_{\mathcal{U},j}$, $j = 1, \cdots, 5$. Each polynomial has $n_j = 18$ variables and a degree of $d_j = 2t_j = 4$. The sparse SOS approach introduces optimization variables γ, $\mathbf{W}_j$ $(j = 1, \cdots, 5)$, and $\mathbf{Q}_i$ $(i = 1, \cdots, 6)$. The variable γ is a scalar. With $d_j = 2t_j = 4$ and $n_j = 18$, the size of variable $\mathbf{W}_j$ is $\binom{n_j + t_j}{n_j} \times \binom{n_j + t_j}{n_j} = \binom{18+2}{18} \times \binom{18+2}{18} = 190 \times 190$. With $n = 66$, $t = 2$ and $e_i = 1$, the size of variable $\mathbf{Q}_i$ is $\binom{n + t - e_i}{n} \times \binom{n + t - e_i}{n} = \binom{66+2-1}{66} \times \binom{66+2-1}{66} = 67 \times 67$. The coefficient matching generates $\binom{n+d}{n} = \binom{66+4}{66} = 916{,}895$ linear equality constraints. After the facial reduction algorithm is applied on the

SDP problem, the size of variable $\mathbf{W}_j$ is reduced to 112×112, about 60% of the original size. The size of variable $\mathbf{Q}_i$ is not changed, remaining as 67×67. The number of linear equality constraints is reduced to 26,250, about 3% of the original number. Solution of this regularized SDP problem took 1h-28min-6s on the same computing cluster to successfully complete.

Table 2-9 summarizes the updating results obtained from the sparse SOS approach with facial reduction. Compared to the results with only 2 modes, the updating results with 5 modes available are more accurate. Therefore, it is not necessary to further optimize the parameters using the function `lsqnonlin`.

Table 2-9 Updating results for the plane truss structure with the first 5 modes measured at 8 DOFs

Variables	Ideal updating results $\boldsymbol{\theta}^*$	Sparse SOS with facial reduction $\boldsymbol{\theta}^*_{\mathrm{SpFR}}$
θ_1	0.100	0.100
θ_2	-0.100	-0.100
θ_3	-0.050	-0.050
θ_4	0.167	0.167
θ_5	-0.500	-0.500
θ_6	-0.167	-0.167

2.5 Summary

This chapter presents SOS optimization methods over modal dynamic residual for linear model updating. Modal dynamic residual approach formulates a polynomial optimization problem to update the unknown model parameters as well as unmeasured entries in the mode shape vectors. When not all DOFs are instrumented/measured by

sensors, this formulation leads to a nonconvex polynomial optimization problem. Local optimization algorithms can be applied directly to such a problem, while they cannot guarantee to find the global optimum and may generate inaccurate values for the model parameters. As shown in the example of a four-story shear structure, only when the starting point is chosen far away from the saddle point, the local optimization algorithms can find correct values for model parameters.

The SOS optimization method converts a polynomial optimization problem into a convex SDP problem, of which the global optimality is guaranteed. While the SOS optimization method is promising in solving nonconvex polynomial problems, the formulated SDP problem can be very expensive to solve. The size of the SDP problem has been discussed and the problem may be practically unsolvable when the number of optimization variable and/or the degree of the polynomial are large. The sparse SOS optimization method is then presented to take advantage of the sparsity in the objective function to reduce the computation effort. When the polynomial objective function consists of several polynomials only involving a small number of variables, sparse SOS optimization method can be applied to eliminate some constraints in the formulated SDP problem.

It is shown that the SDP problems arising from modal dynamic residual formulation fail to satisfy the Slater condition. This failure increases the difficulty of finding the optimal solution of the SDP problem using numerical algorithms. The facial reduction technique, especially a practical algorithm Sieve-SDP, is discussed and applied to restrict such an SDP problem onto a feasible set with lower dimension and yields an equivalent SDP problem for which there are strictly feasible points. The smaller equivalent SDP can then be solved

by a numerical solver in a more stable manner. Numerical simulation on a plane truss structure demonstrates that the facial reduction technique can effectively reduce the size of an SDP problem and thus save the overall computational efforts to find the global optimum of the model updating problem.

CHAPTER 3. MODEL UPDATING USING CONSTRAINED KALMAN FILTERS

This chapter addresses finite element model updating for linear and nonlinear structures using time domain data. The nonlinear versions of Kalman filter, especially extended Kalman filter (EKF) and unscented Kalman filter (UKF), are commonly used identification algorithms in civil engineering. Kalman filter produces *a posteriori* probabilistic estimates of unknown state variables based on system equations and noisy measurements. Parameter identification is performed by treating the model parameters as augmented system states. The parameter values are then also estimated from the measurement data. Different from frequency domain algorithms that are mostly applicable to linear structures, EKF and UKF can be used for system identification of nonlinear structures.

As one of the most widely used approaches in state estimation for nonlinear systems, EKF linearizes the nonlinear system equation around the current estimate and calculates the Kalman gain based on the linearized system equation. It has been shown that EKF works well for system with mild nonlinearity but often provides unreliable estimates for highly nonlinear systems due to the large linearization error. A powerful alternative to EKF is UKF which relies on the unscented transformation for estimating system states and parameters. UKF is designed based on the intuition that it should be easier to approximate a given distribution than to approximate an arbitrary nonlinear function. At each iteration, UKF generates a sample distribution by a set of sampling points called sigma points, which capture the mean and covariance of the *a posteriori* distribution of system states. These

sigma points can be easily propagated through the nonlinear system equation and used for the state estimate.

The standard EKF and UKF are briefly introduced. To improve the parameter identification performance, the constrained EKF (CEKF) and the constrained UKF (CUKF) are proposed to ensure that the parameter estimates satisfy constraints from physical laws. The performance of the proposed methods is investigated through simulation on a linear four-story shear frame structure and a nonlinear single degree of freedom (SDOF) Bouc-Wen hysteretic system.

3.1 Extended Kalman Filter (EKF) for Parameter Identification

This section presents EKF for structural model parameter identification. EKF is an extension of Kalman filter for optimally estimating the state of a nonlinear system from measurement data. The standard EKF is briefly introduced and the constrained EKF (CEKF) is proposed to prevent the estimates from being unrealistic during estimation process.

3.1.1 The Standard EKF

Consider a state vector $\mathbf{x} = (\mathbf{q}^{\mathrm{T}}, \dot{\mathbf{q}}^{\mathrm{T}}, \boldsymbol{\theta}^{\mathbf{T}})^{\mathbf{T}}$ containing displacement vector $\mathbf{q}$, velocity vector $\dot{\mathbf{q}}$, and model parameters $\boldsymbol{\theta}$ for the FE model updating problem. The general dynamical system is governed by a nonlinear state-space equation as:

$$\dot{\mathbf{x}} = \boldsymbol{f}(\mathbf{x}, \mathbf{u}, \mathbf{w}) \tag{3-1}$$

where $\mathbf{u}$ is known excitation applied on the system and $\mathbf{w} \sim \mathcal{N}(\mathbf{0}, \boldsymbol{\Sigma}_{\mathbf{w}})$ is a zero-mean white Gaussian process noise with covariance matrix $\boldsymbol{\Sigma}_{\mathbf{w}}$. At time $t = k\Delta t$, the measurement $\mathbf{y}_k$ is given as:

$$\mathbf{y}_k = \boldsymbol{h}(\mathbf{x}_k, \mathbf{u}_k, \mathbf{v}_k) \tag{3-2}$$

where $\mathbf{v}_k \sim \mathcal{N}(\mathbf{0}, \boldsymbol{\Sigma}_{\mathbf{v}})$ is the zero-mean white Gaussian measurement noise with covariance matrix $\boldsymbol{\Sigma}_{\mathbf{v}}$.

The EKF estimation is separated into two main steps, i.e. measurement update step and time update step. In the measurement update step, the *a priori* estimate $\hat{\mathbf{x}}_{k|k-1}$ of the state is available. The predicted measurement $\hat{\mathbf{y}}_{k|k-1}$ of state $\mathbf{x}_k$ is estimated as:

$$\hat{\mathbf{y}}_{k|k-1} = \boldsymbol{h}\left(\hat{\mathbf{x}}_{k|k-1}, \mathbf{u}_k, \mathbf{0}\right) \tag{3-3}$$

The Kalman gain matrix $\mathbf{L}_k$ is calculated to minimize the trace of the covariance matrix for the *a posteriori* estimate:

$$\mathbf{L}_k = \boldsymbol{\Sigma}_{\mathbf{x}_{k|k-1}} (\mathbf{H}_k^{\mathrm{x}})^{\mathrm{T}} \left(\mathbf{H}_k^{\mathrm{x}} \boldsymbol{\Sigma}_{\mathbf{x}_{k|k-1}} (\mathbf{H}_k^{\mathrm{x}})^{\mathrm{T}} + \mathbf{H}_k^{\mathrm{v}} \boldsymbol{\Sigma}_{\mathbf{v}} (\mathbf{H}_k^{\mathrm{v}})^{\mathrm{T}} \right)^{-1} \tag{3-4}$$

Here $\mathbf{H}_k^{\mathrm{x}}$ and $\mathbf{H}_k^{\mathrm{v}}$ are the linearized matrices of the measurement equation $\boldsymbol{h}$:

$$\mathbf{H}_k^{\mathrm{x}} = \left. \frac{\partial \boldsymbol{h}}{\partial \mathbf{x}} \right|_{\mathbf{x} = \hat{\mathbf{x}}_{k|k-1}} \tag{3-5}$$

$$\mathbf{H}_k^{\mathrm{v}} = \left.\frac{\partial \boldsymbol{h}}{\partial \mathbf{v}}\right|_{\mathbf{x}=\hat{\mathbf{x}}_{k|k-1}} \tag{3-6}$$

After measurement $\mathbf{y}_k$ is available, the *a posteriori* estimate $\hat{\mathbf{x}}_{k|k}$ is calculated using the Kalman gain matrix as:

$$\hat{\mathbf{x}}_{k|k} = \hat{\mathbf{x}}_{k|k-1} + \mathbf{L}_k\left(\mathbf{y}_k - \hat{\mathbf{y}}_{k|k-1}\right) \tag{3-7}$$

Along with the measurement update of the state, the covariance matrix $\boldsymbol{\Sigma}_{\mathbf{x}_{k|k}}$ for the *a posteriori* estimate can be evaluated as:

$$\boldsymbol{\Sigma}_{\mathbf{x}_{k|k}} = (\mathbf{I} - \mathbf{L}_k\mathbf{H}_k^{\mathrm{x}})\boldsymbol{\Sigma}_{\mathbf{x}_{k|k-1}}(\mathbf{I} - \mathbf{L}_k\mathbf{H}_k^{\mathrm{x}})^{\mathrm{T}} + \mathbf{L}_k\mathbf{H}_k^{\mathrm{v}}\boldsymbol{\Sigma}_{\mathbf{v}}(\mathbf{H}_k^{\mathrm{v}})^{\mathrm{T}}\mathbf{L}_k^{\mathrm{T}} \tag{3-8}$$

In the time update step, the *a priori* estimate $\hat{\mathbf{x}}_{k+1|k}$ of the state is predicted based on the system model:

$$\hat{\mathbf{x}}_{k+1|k} = \hat{\mathbf{x}}_{k|k} + \int_{k\Delta t}^{(k+1)\Delta t} f(\hat{\mathbf{x}}, \mathbf{u}, \mathbf{0})dt \tag{3-9}$$

Along with the time update of the state, the covariance matrix $\boldsymbol{\Sigma}_{\mathbf{x}_{k+1|k}}$ for the *a priori* estimate can be evaluated as [76]:

$$\boldsymbol{\Sigma}_{\mathbf{x}_{k+1|k}} = \boldsymbol{\Phi}_k^{\mathbf{x}}\boldsymbol{\Sigma}_{\mathbf{x}_{k|k}}(\boldsymbol{\Phi}_k^{\mathbf{x}})^{\mathrm{T}} + \boldsymbol{\Phi}_k^{\mathbf{w}}\boldsymbol{\Sigma}_{\mathbf{w}}(\boldsymbol{\Phi}_k^{\mathrm{w}})^{\mathrm{T}} \tag{3-10}$$

Here $\boldsymbol{\Phi}_k^{\mathbf{x}}$ and $\boldsymbol{\Phi}_k^{\mathbf{w}}$ are the state transition matrices and can be calculated by linearization of state-space equation $\boldsymbol{f}$:

$$\mathbf{\Phi}_k^{\mathrm{x}} = \mathbf{I} + \frac{\partial \boldsymbol{f}}{\partial \mathbf{x}}\Big|_{\mathbf{x}=\hat{\mathbf{x}}_{k|k}} \Delta t \tag{3-11}$$

$$\mathbf{\Phi}_k^{\mathbf{w}} = \frac{\partial \boldsymbol{f}}{\partial \mathbf{w}}\Big|_{\mathbf{x}=\hat{\mathbf{x}}_{k|k}} \Delta t \tag{3-12}$$

Repeating Eq. (3-3) ~ Eq. (3-12), EKF can recursively update the system states for a nonlinear system.

3.1.2 The Constrained EKF

The standard EKF on parameter identification problems finds the estimate of parameters through the entire unconstrained solution space. However, in structural applications, some model parameters must satisfy equality or inequality constraints from physics. Without incorporating those constraints in the estimation process, the standard EKF may lead to infeasible solutions. Therefore, certain constraints on parameters need to be incorporated in EKF algorithm.

EKF is the minimum-mean-square-error (MMSE) estimator for the linearized dynamical system. The Kalman gain $\mathbf{L}_k$ at time $t = k\Delta t$ of the unconstrained EKF (Eq. (3-4)) can be analytically derived by minimizing the trace of the *a posteriori* state covariance matrix:

$$\underset{\mathbf{L}}{\text{minimize}}\ \text{Trace}\left((\mathbf{I} - \mathbf{L}\mathbf{H}_k^{\mathrm{x}})\mathbf{\Sigma}_{\mathbf{x}_{k|k-1}}(\mathbf{I} - \mathbf{L}\mathbf{H}_k^{\mathrm{x}})^{\mathrm{T}} + \mathbf{L}\mathbf{H}_k^{\mathrm{v}}\mathbf{\Sigma}_{\mathbf{v}}(\mathbf{H}_k^{\mathrm{v}})^{\mathrm{T}}\mathbf{L}^{\mathrm{T}}\right) \tag{3-13}$$

When a general constraint $\boldsymbol{g}(\mathbf{x}) \geq 0$ is imposed on the system states, the closed-form solution of the Kalman gain matrix is usually difficult, if not impossible, to obtain. In this

situation, the Kalman gain of the constrained EKF can be numerically calculated by solving the optimization problem:

$$\begin{aligned} &\underset{\mathbf{L}}{\text{minimize}} \ \text{Trace}\left((\mathbf{I}-\mathbf{L}\mathbf{H}_k^{\text{x}})\boldsymbol{\Sigma}_{\mathbf{x}_{k|k-1}}(\mathbf{I}-\mathbf{L}\mathbf{H}_k^{\text{x}})^{\text{T}}+\mathbf{L}\mathbf{H}_k^{\text{v}}\boldsymbol{\Sigma}_{\mathbf{v}}(\mathbf{H}_k^{\text{v}})^{\text{T}}\mathbf{L}^{\text{T}}\right) \\ &\text{subject to} \ \boldsymbol{g}\left(\hat{\mathbf{x}}_{k|k-1}+\mathbf{L}\left(\mathbf{y}_k-\hat{\mathbf{y}}_{k|k-1}\right)\right)\geq 0 \end{aligned} \tag{3-14}$$

The computation cost increases from solving this optimization problem. Using the optimal Kalman gain matrix $\mathbf{L}^*$ solved from Eq. (3-14), the updated *a posteriori* estimates $\hat{\mathbf{x}}_{k|k}=\hat{\mathbf{x}}_{k|k-1}+\mathbf{L}^*\left(\mathbf{y}_k-\hat{\mathbf{y}}_{k|k-1}\right)$ are guaranteed to satisfy the constraints $\boldsymbol{g}\left(\hat{\mathbf{x}}_{k|k}\right)\geq 0$. The covariance matrix $\boldsymbol{\Sigma}_{\mathbf{x}_{k|k}}$ corresponding to the updated *a posteriori* estimates can also be calculated using $\mathbf{L}^*$.

Instead of a general function $\boldsymbol{g}(\mathbf{x})\geq 0$, constraints encountered in engineering applications are usually affine, i.e. $\mathbf{A}\mathbf{x}-\mathbf{b}\geq\mathbf{0}$. Here, $\mathbf{A}\in\mathbb{R}^{n_c\times n_x}$ is a constant coefficient matrix and $\mathbf{b}\in\mathbb{R}^{n_c}$ is a constant coefficient vector. Suppose that at time $t=k\Delta t$, n_{ac} of the n_c inequality constraints are active $\mathbf{A}_{\text{a}}\mathbf{x}-\mathbf{b}_{\text{a}}=\mathbf{0}$, where $\mathbf{A}_{\text{a}}\in\mathbb{R}^{n_{ac}\times n_x}$ and $\mathbf{b}_{\text{a}}\in\mathbb{R}^{n_{ac}}$. In this scenario, explicit analytical solution can be found for the optimal Kalman gain to the optimization problem Eq. (3-14). The optimization problem to compute the Kalman gain with equality constraint $\mathbf{A}_{\text{a}}\mathbf{x}-\mathbf{b}_{\text{a}}=\mathbf{0}$ is formulated as:

$$\begin{aligned} &\underset{\mathbf{L}}{\text{minimize}} \ \text{Trace}\left((\mathbf{I}-\mathbf{L}\mathbf{H}_k^{\text{x}})\boldsymbol{\Sigma}_{\mathbf{x}_{k|k-1}}(\mathbf{I}-\mathbf{L}\mathbf{H}_k^{\text{x}})^{\text{T}}+\mathbf{L}\mathbf{H}_k^{\text{v}}\boldsymbol{\Sigma}_{\mathbf{v}}(\mathbf{H}_k^{\text{v}})^{\text{T}}\mathbf{L}^{\text{T}}\right) \\ &\text{subject to} \ \mathbf{A}_{\text{a}}\left(\hat{\mathbf{x}}_{k|k-1}+\mathbf{L}\left(\mathbf{y}_k-\hat{\mathbf{y}}_{k|k-1}\right)\right)-\mathbf{b}_{\text{a}}=\mathbf{0} \end{aligned} \tag{3-15}$$

To lighten notations, denote the measurement residual $\mathbf{r}_k$ and innovation covariance $\mathbf{\Sigma}_{\mathbf{y}_{k|k-1}}$ at time $t = k\Delta t$ as:

$$\mathbf{r}_k = \mathbf{y}_k - \hat{\mathbf{y}}_{k|k-1} \tag{3-16}$$

$$\mathbf{\Sigma}_{\mathbf{y}_k} = \mathbf{H}_k^{\mathrm{x}} \mathbf{\Sigma}_{\mathbf{x}_{k|k-1}} (\mathbf{H}_k^{\mathrm{x}})^{\mathrm{T}} + \mathbf{H}_k^{\mathrm{v}} \mathbf{\Sigma}_{\mathbf{v}} (\mathbf{H}_k^{\mathrm{v}})^{\mathrm{T}} \tag{3-17}$$

Using Lagrange multiplier $\boldsymbol{\nu} \in \mathbb{R}^{n_{ac}}$, the Lagrangian for the problem Eq. (3-15) formulated as:

$$\begin{aligned} \mathcal{L}(\mathbf{L}, \boldsymbol{\nu}) = \mathrm{Trace}\Big((\mathbf{I} - \mathbf{L}\mathbf{H}_k^{\mathrm{x}}) \mathbf{\Sigma}_{\mathbf{x}_{k|k-1}} (\mathbf{I} - \mathbf{L}\mathbf{H}_k^{\mathrm{x}})^{\mathrm{T}} + \mathbf{L}\mathbf{H}_k^{\mathrm{v}} \mathbf{\Sigma}_{\mathbf{v}} (\mathbf{H}_k^{\mathrm{v}})^{\mathrm{T}} \mathbf{L}^{\mathrm{T}} \Big) \\ + \boldsymbol{\nu}^{\mathrm{T}} \big(\mathbf{A}_{\mathrm{a}} \big(\hat{\mathbf{x}}_{k|k-1} + \mathbf{L}\mathbf{r}_k \big) - \mathbf{b}_{\mathrm{a}} \big) \end{aligned} \tag{3-18}$$

Note that $\mathbf{\Sigma}_{\mathbf{x}_{k|k-1}} = \mathbf{\Sigma}_{\mathbf{x}_{k|k-1}}^{\mathrm{T}}$ and $\mathbf{H}_k^{\mathrm{v}} \mathbf{\Sigma}_{\mathbf{v}} (\mathbf{H}_k^{\mathrm{v}})^{\mathrm{T}} = (\mathbf{H}_k^{\mathrm{v}} \mathbf{\Sigma}_{\mathbf{v}} (\mathbf{H}_k^{\mathrm{v}})^{\mathrm{T}})^{\mathrm{T}}$. The partial derivatives of $\mathcal{L}(\mathbf{L}, \boldsymbol{\nu})$ with respect to $\mathbf{L}$ and $\boldsymbol{\nu}$, respectively, can be calculated as:

$$\frac{\partial}{\partial \mathbf{L}} \mathcal{L}(\mathbf{L}, \boldsymbol{\nu}) = 2(\mathbf{I} - \mathbf{L}\mathbf{H}_k^{\mathrm{x}}) \mathbf{\Sigma}_{\mathbf{x}_{k|k-1}} (-(\mathbf{H}_k^{\mathrm{x}})^{\mathrm{T}}) + 2\mathbf{L}\mathbf{H}_k^{\mathrm{v}} \mathbf{\Sigma}_{\mathbf{v}} (\mathbf{H}_k^{\mathrm{v}})^{\mathrm{T}} + \mathbf{A}_{\mathrm{a}}^{\mathrm{T}} \boldsymbol{\nu} \mathbf{r}_k^{\mathrm{T}} \tag{3-19}$$

$$\frac{\partial}{\partial \boldsymbol{\nu}} \mathcal{L}(\mathbf{L}, \boldsymbol{\nu}) = \mathbf{A}_{\mathrm{a}} \big(\hat{\mathbf{x}}_{k|k-1} + \mathbf{L}\mathbf{r}_k \big) - \mathbf{b}_{\mathrm{a}} \tag{3-20}$$

The optimality requires that both partial derivatives are zero. Assume $\mathbf{A}_{\mathrm{a}} \in \mathbb{R}^{n_{\mathrm{ac}} \times n_{\mathbf{x}}}$ is a full row-rank matrix with $\mathrm{rank}(\mathbf{A}_{\mathrm{a}}) = n_{\mathrm{ac}} \leq n_{\mathbf{x}}$. We can express the Kalman gain $\mathbf{L}$ as a function of the Lagrange multiplier $\boldsymbol{\nu}$. First, the partial derivative $\frac{\partial}{\partial \mathbf{L}} \mathcal{L}(\mathbf{L}, \boldsymbol{\nu})$ in Eq. (3-19) is set as zero. Solving the equation $\frac{\partial}{\partial \mathbf{L}} \mathcal{L}(\mathbf{L}, \boldsymbol{\nu}) = \mathbf{0}$ for $\mathbf{L}$ provides:

$$\mathbf{L} = \boldsymbol{\Sigma}_{\mathbf{x}_{k|k-1}} (\mathbf{H}_k^{\mathrm{x}})^{\mathrm{T}} \boldsymbol{\Sigma}_{\mathbf{y}_{k|k-1}}^{-1} - \frac{1}{2} \mathbf{A}_{\mathrm{a}}^{\mathrm{T}} \boldsymbol{\nu} \mathbf{r}_k^{\mathrm{T}} \boldsymbol{\Sigma}_{\mathbf{y}_{k|k-1}}^{-1} \tag{3-21}$$

Substituting Kalman gain expression Eq. (3-21) into the partial derivative Eq. (3-20) and solving the equation $\frac{\partial}{\partial \boldsymbol{\nu}} \mathcal{L}(\mathbf{L}, \boldsymbol{\nu}) = \mathbf{0}$ for $\boldsymbol{\nu}$ provides:

$$\boldsymbol{\nu} = 2(\mathbf{A}_{\mathrm{a}} \mathbf{A}_{\mathrm{a}}^{\mathrm{T}})^{-1} \left(\mathbf{A}_{\mathrm{a}} \left(\hat{\mathbf{x}}_{k|k-1} + \boldsymbol{\Sigma}_{\mathbf{x}_{k|k-1}} (\mathbf{H}_k^{\mathrm{x}})^{\mathrm{T}} \boldsymbol{\Sigma}_{\mathbf{y}_{k|k-1}}^{-1} \mathbf{r}_k \right) - \mathbf{b}_{\mathrm{a}} \right) \left(\mathbf{r}_k^{\mathrm{T}} \boldsymbol{\Sigma}_{\mathbf{y}_{k|k-1}}^{-1} \mathbf{r}_k \right)^{-1} \tag{3-22}$$

Denote the unconstrained Kalman gain and the *a posterior* state estimate of the unconstrained EKF as:

$$\tilde{\mathbf{L}}_k = \boldsymbol{\Sigma}_{\mathbf{x}_{k|k-1}} (\mathbf{H}_k^{\mathrm{x}})^{\mathrm{T}} \boldsymbol{\Sigma}_{\mathbf{y}_{k|k-1}}^{-1} \tag{3-23}$$

$$\tilde{\mathbf{x}}_{k|k} = \hat{\mathbf{x}}_{k|k-1} + \tilde{\mathbf{L}}_k \mathbf{r}_k \tag{3-24}$$

The Lagrange multiplier $\boldsymbol{\nu}$ in Eq. (3-32) is simplified as:

$$\boldsymbol{\nu} = 2(\mathbf{A}_{\mathrm{a}} \mathbf{A}_{\mathrm{a}}^{\mathrm{T}})^{-1} \left(\mathbf{A}_{\mathrm{a}} \tilde{\mathbf{x}}_{k|k} - \mathbf{b}_{\mathrm{a}} \right) \left(\mathbf{r}_k^{\mathrm{T}} \boldsymbol{\Sigma}_{\mathbf{y}_{k|k-1}}^{-1} \mathbf{r}_k \right)^{-1} \tag{3-25}$$

Finally, substituting the simplified $\boldsymbol{\nu}$ into Eq. (3-21), the Kalman gain of CEKF can be rewritten as:

$$\mathbf{L}_k = \tilde{\mathbf{L}}_k - \mathbf{A}_{\mathrm{a}}^{\mathrm{T}} (\mathbf{A}_{\mathrm{a}} \mathbf{A}_{\mathrm{a}}^{\mathrm{T}})^{-1} \left(\mathbf{A}_{\mathrm{a}} \tilde{\mathbf{x}}_{k|k} - \mathbf{b}_{\mathrm{a}} \right) \left(\mathbf{r}_k^{\mathrm{T}} \boldsymbol{\Sigma}_{\mathbf{y}_{k|k-1}}^{-1} \mathbf{r}_k \right)^{-1} \mathbf{r}_k^{\mathrm{T}} \boldsymbol{\Sigma}_{\mathbf{y}_{k|k-1}}^{-1} \tag{3-26}$$

The same solution is obtained in [77] while the derivation is more complicated. Using this Kalman gain, the *a posteriori* estimate $\hat{\mathbf{x}}_{k|k}$ of CEKF is found to be related to the unconstrained EKF estimation $\tilde{\mathbf{x}}_{k|k}$:

$$\hat{\mathbf{x}}_{k|k} = \tilde{\mathbf{x}}_{k|k} - \mathbf{A}_{\mathrm{a}}^{\mathrm{T}}(\mathbf{A}_{\mathrm{a}}\mathbf{A}_{\mathrm{a}}^{\mathrm{T}})^{-1}\left(\mathbf{A}_{\mathrm{a}}\tilde{\mathbf{x}}_{k|k} - \mathbf{b}_{\mathrm{a}}\right) \tag{3-27}$$

Finally, CEKF algorithm is summarized as follows.

Initial Estimate		
State estimate	$\hat{\mathbf{x}}_{0\|-1} = \mathbb{E}[\mathbf{x}_0]$	
State covariance	$\boldsymbol{\Sigma}_{\mathbf{x}_{0\|-1}} = \mathbb{E}\left[(\mathbf{x}_0 - \hat{\mathbf{x}}_{0\|-1})(\mathbf{x}_0 - \hat{\mathbf{x}}_{0\|-1})^{\mathrm{T}}\right]$	
`for` $k = 0, 1, \cdots, n$		
Measurement Update		
Measurement residual	$\mathbf{r}_k = \mathbf{y}_k - \hat{\mathbf{y}}_{k\|k-1}$	Rept. (3-16)
Innovation covariance matrix	$\boldsymbol{\Sigma}_{\mathbf{y}_k} = \mathbf{H}_k^{\mathrm{x}}\boldsymbol{\Sigma}_{\mathbf{x}_{k\|k-1}}(\mathbf{H}_k^{\mathrm{x}})^{\mathrm{T}} + \mathbf{H}_k^{\mathrm{v}}\boldsymbol{\Sigma}_{\mathbf{v}}(\mathbf{H}_k^{\mathrm{v}})^{\mathrm{T}}$	Rept. (3-17)
Kalman gain	$\tilde{\mathbf{L}}_k = \boldsymbol{\Sigma}_{\mathbf{x}_{k\|k-1}}(\mathbf{H}_k^{\mathrm{x}})^{\mathrm{T}}\boldsymbol{\Sigma}_{\mathbf{y}_k}^{-1}$	Rept. (3-23)
State estimate	$\tilde{\mathbf{x}}_{k\|k} = \hat{\mathbf{x}}_{k\|k-1} + \tilde{\mathbf{L}}_k\mathbf{r}_k$	Rept. (3-24)
Check constraints		
`if` There is no active constraint		
	$\mathbf{L}_k = \tilde{\mathbf{L}}_k$	
	$\hat{\mathbf{x}}_{k\|k} = \tilde{\mathbf{x}}_{k\|k}$	
`else if` There are active constraints $\mathbf{A}_{\mathrm{a}}\mathbf{x} - \mathbf{b}_{\mathrm{a}} = \mathbf{0}$		
	$\mathbf{L}_k = \tilde{\mathbf{L}}_k - \mathbf{A}_{\mathrm{a}}^{\mathrm{T}}(\mathbf{A}_{\mathrm{a}}\mathbf{A}_{\mathrm{a}}^{\mathrm{T}})^{-1}\left(\mathbf{A}_{\mathrm{a}}\tilde{\mathbf{x}}_{k\|k} - \mathbf{b}_{\mathrm{a}}\right)\left(\mathbf{r}_k^{\mathrm{T}}\boldsymbol{\Sigma}_{\mathbf{y}_{k\|k-1}}^{-1}\mathbf{r}_k\right)^{-1}\mathbf{r}_k^{\mathrm{T}}\boldsymbol{\Sigma}_{\mathbf{y}_k}^{-1}$	Rept. (3-26)
	$\hat{\mathbf{x}}_{k\|k} = \tilde{\mathbf{x}}_{k\|k} - \mathbf{A}_{\mathrm{a}}^{\mathrm{T}}(\mathbf{A}_{\mathrm{a}}\mathbf{A}_{\mathrm{a}}^{\mathrm{T}})^{-1}\left(\mathbf{A}_{\mathrm{a}}\tilde{\mathbf{x}}_{k\|k} - \mathbf{b}_{\mathrm{a}}\right)$	Rept. (3-27)
`end if`		
State covariance	$\boldsymbol{\Sigma}_{\mathbf{x}_{k\|k}} = (\mathbf{I} - \mathbf{L}_k\mathbf{H}_k^{\mathrm{x}})\boldsymbol{\Sigma}_{\mathbf{x}_{k\|k-1}}(\mathbf{I} - \mathbf{L}_k\mathbf{H}_k^{\mathrm{x}})^{\mathrm{T}} + \mathbf{L}_k\mathbf{H}_k^{\mathrm{v}}\boldsymbol{\Sigma}_{\mathbf{v}}(\mathbf{H}_k^{\mathrm{v}})^{\mathrm{T}}\mathbf{L}_k^{\mathrm{T}}$	Rept. (3-8)
Time Update		

State estimate	$\hat{\mathbf{x}}_{k+1\|k} = \hat{\mathbf{x}}_{k\|k} + \int_{k\Delta t}^{(k+1)\Delta t} f(\hat{\mathbf{x}}, \mathbf{u}, \mathbf{0}) dt$	Rept. (3-9)
State covariance	$\boldsymbol{\Sigma}_{\mathbf{x}_{k+1\|k}} = \boldsymbol{\Phi}_k^{\mathbf{x}} \boldsymbol{\Sigma}_{\mathbf{x}_{k\|k}} (\boldsymbol{\Phi}_k^{\mathbf{x}})^{\mathrm{T}} + \boldsymbol{\Phi}_k^{\mathbf{w}} \boldsymbol{\Sigma}_{\mathbf{w}} (\boldsymbol{\Phi}_k^{\mathrm{w}})^{\mathrm{T}}$	Rept. (3-10)
`end loop`		

3.2 Unscented Kalman Filter (UKF) for Parameter Identification

This section presents UKF for structural model parameter identification. UKF is another nonlinear variant of Kalman filter, which propagates the first two moments of states through suitably selected sigma points and corresponding weights. The standard UKF is briefly introduced and the constrained UKF (CUKF) is proposed to prevent the state estimates from violating constraints due to physical laws.

3.2.1 The Standard UKF

Similar to EKF, consider a state vector $\mathbf{x} = (\mathbf{q}^{\mathrm{T}}, \dot{\mathbf{q}}^{\mathrm{T}}, \boldsymbol{\theta}^{\mathbf{T}})^{\mathbf{T}}$. The nonlinear state-space equation is denoted as:

$$\dot{\mathbf{x}} = \boldsymbol{f}(\mathbf{x}, \mathbf{u}, \mathbf{w}) \tag{3-28}$$

where $\mathbf{u}$ is known excitation applied on the system and $\mathbf{w} \sim \mathcal{N}(\mathbf{0}, \boldsymbol{\Sigma}_{\mathbf{w}})$ is a zero-mean white Gaussian process noise with covariance matrix $\boldsymbol{\Sigma}_{\mathbf{w}}$. At time $t = k\Delta t$, the measurement $\mathbf{y}_k$ is given as:

$$\mathbf{y}_k = \boldsymbol{h}(\mathbf{x}_k, \mathbf{u}_k, \mathbf{v}_k) \tag{3-29}$$

where $\mathbf{v}_k \sim \mathcal{N}(\mathbf{0}, \mathbf{\Sigma}_\mathbf{v})$ is the zero-mean white Gaussian measurement noise with covariance matrix $\mathbf{\Sigma}_\mathbf{v}$.

In general, the state-space equation and measurement equation have noises, $\mathbf{w} \in \mathbb{R}^{n_\mathbf{w}}$ and $\mathbf{v}_k \in \mathbb{R}^{n_\mathbf{v}}$, entering those equations nonlinearly. Thus, the most general formulation of the UKF concatenates the process and measurement noise with the state vector $\mathbf{x} \in \mathbb{R}^{n_\mathbf{x}}$ to form an augmented state vector with dimension $N = n_\mathbf{x} + n_\mathbf{w} + n_\mathbf{v}$:

$$\mathbf{x}^a = [\mathbf{x}^\mathrm{T} \quad \mathbf{w}^\mathrm{T} \quad \mathbf{v}^\mathrm{T}]^\mathrm{T} \tag{3-30}$$

At time $t = k\Delta t$, the estimate of the augmented state vector is:

$$\hat{\mathbf{x}}^a_{k|k-1} = \left[\hat{\mathbf{x}}^\mathrm{T}_{k|k-1} \quad \mathbf{0} \quad \mathbf{0}\right]^\mathrm{T} \tag{3-31}$$

with error covariance matrix:

$$\mathbf{\Sigma}_{\mathbf{x}^a_{k|k-1}} = \begin{bmatrix} \mathbf{\Sigma}_{\mathbf{x}_{k|k-1}} & \mathbf{0} & \mathbf{0} \\ \mathbf{0} & \mathbf{\Sigma}_\mathbf{w} & \mathbf{0} \\ \mathbf{0} & \mathbf{0} & \mathbf{\Sigma}_\mathbf{v} \end{bmatrix} \tag{3-32}$$

The UKF estimation is separated into two main steps, i.e. measurement update step and time update step. Assuming by induction that the *a priori* estimate $\hat{\mathbf{x}}^a_{k|k-1}$ and its covariance matrix $\mathbf{\Sigma}_{\mathbf{x}^a_{k|k-1}}$ is known, $2N + 1$ sigma points $\boldsymbol{\mathcal{x}}^a_{k|k-1,i}$, $i = 0, 1, \cdots, 2N + 1$, are generated as:

$$\boldsymbol{x}^a_{k|k-1,0} = \hat{\mathbf{x}}^a_{k|k-1}$$

$$\boldsymbol{x}^a_{k|k-1,i} = \hat{\mathbf{x}}^a_{k|k-1} + \left(\sqrt{(N+\kappa)\boldsymbol{\Sigma}_{\mathbf{x}^a_{k|k-1}}}\right)_i \qquad i = 1, 2, \cdots, N \tag{3-33}$$

$$\boldsymbol{x}^a_{k|k-1,i} = \hat{\mathbf{x}}^a_{k|k-1} - \left(\sqrt{(N+\kappa)\boldsymbol{\Sigma}_{\mathbf{x}^a_{k|k-1}}}\right)_i \qquad i = 1, 2, \cdots, N$$

where $\sqrt{\cdot}$ is the matrix square root and $(\cdot)_i$ refers to the i-th column of the matrix. κ is a scaling parameter, and can be any number as long as $N + \kappa > 0$ [76, 78]. The $2N + 1$ weighting coefficients for the sigma points are given as:

$$W_0 = \frac{\kappa}{N+\kappa}$$

$$W_i = \frac{1}{2(N+\kappa)} \qquad i = 1, 2, \cdots, 2N \tag{3-34}$$

Using $\boldsymbol{x}^a_{k|k-1,i} = \left[\boldsymbol{x}^{\mathbf{x}}_{k|k-1,i} \quad \boldsymbol{x}^{\mathbf{w}}_{k|k-1,i} \quad \boldsymbol{x}^{\mathbf{v}}_{k|k-1,i}\right]^{\mathrm{T}}$, the predicted measurement $\boldsymbol{y}_{k|k-1,i}$ of each sigma point can be evaluated as:

$$\boldsymbol{y}_{k|k-1,i} = h\left(\boldsymbol{x}^{\mathbf{x}}_{k|k-1,i}, \mathbf{u}_k, \boldsymbol{x}^{\mathbf{v}}_{k|k-1,i}\right) \qquad i = 0,1, \cdots, 2N \tag{3-35}$$

The predicted measurement $\hat{\mathbf{y}}_{k|k-1}$ of state $\mathbf{x}_k$ is calculated as the weighted average of the predicted measurements of sigma points:

$$\hat{\mathbf{y}}_{k|k-1} = \sum_{i=0}^{2N} W_i \boldsymbol{y}_{k|k-1,i} \tag{3-36}$$

The innovation covariance matrix $\boldsymbol{\Sigma}_{\mathbf{y}_{k|k-1}}$ can be evaluated as:

$$\boldsymbol{\Sigma}_{\mathbf{y}_{k|k-1}} = \sum_{i=0}^{2N} W_i \left(\boldsymbol{\mathcal{Y}}_{k|k-1,i} - \hat{\mathbf{y}}_{k|k-1}\right)\left(\boldsymbol{\mathcal{Y}}_{k|k-1,i} - \hat{\mathbf{y}}_{k|k-1}\right)^{\mathrm{T}} \tag{3-37}$$

As noises **w** and **v** need not to be estimated, here the cross covariance $\boldsymbol{\Sigma}_{\mathbf{xy}_{k|k-1}}$ between the *a priori* estimate $\hat{\mathbf{x}}_{k|k-1}$ and its measurement $\hat{\mathbf{y}}_{k|k-1}$, rather than the cross covariance $\boldsymbol{\Sigma}_{\mathbf{x}^a\mathbf{y}_{k|k-1}}$, is required. From the sigma points and the predicted measurements of sigma points, the cross covariance $\boldsymbol{\Sigma}_{\mathbf{xy}_{k|k-1}}$ can be calculated as:

$$\boldsymbol{\Sigma}_{\mathbf{xy}_{k|k-1}} = \sum_{i=0}^{2N} W_i \left(\boldsymbol{\mathcal{X}}^{\mathbf{x}}_{k|k-1,i} - \hat{\mathbf{x}}_{k|k-1}\right)\left(\boldsymbol{\mathcal{Y}}_{k|k-1,i} - \hat{\mathbf{y}}_{k|k-1}\right)^{\mathrm{T}} \tag{3-38}$$

According to state estimation theory [79], the Kalman gain matrix is calculated as:

$$\mathbf{L}_k = \boldsymbol{\Sigma}_{\mathbf{xy}_{k|k-1}} \left(\boldsymbol{\Sigma}_{\mathbf{y}_{k|k-1}}\right)^{-1} \tag{3-39}$$

After measurement $\mathbf{y}_k$ is available, the measurement residual is obtained:

$$\mathbf{r}_k = \mathbf{y}_k - \hat{\mathbf{y}}_{k|k-1} \tag{3-40}$$

The *a posteriori* estimate $\hat{\mathbf{x}}_{k|k}$ is calculated using the Kalman gain matrix as:

$$\hat{\mathbf{x}}_{k|k} = \hat{\mathbf{x}}_{k|k-1} + \mathbf{L}_k \mathbf{r}_k \tag{3-41}$$

Along with the measurement update of the state, the error covariance matrix $\boldsymbol{\Sigma}_{\mathbf{x}_{k|k}}$ for the *a posteriori* estimate can be evaluated as:

$$\boldsymbol{\Sigma}_{\mathbf{x}_{k|k}} = \boldsymbol{\Sigma}_{\mathbf{x}_{k|k-1}} - \mathbf{L}_k \boldsymbol{\Sigma}_{\mathbf{y}_{k|k-1}} \mathbf{L}_k^{\mathrm{T}} \tag{3-42}$$

In the time update step, $2N+1$ sigma points $\boldsymbol{x}_{k|k,i}^{a}$, $i = 0, 1, \cdots, 2N+1$, are generated again using updated covariance matrix $\boldsymbol{\Sigma}_{\mathbf{x}_{k|k}}$ as:

$$\begin{aligned} \boldsymbol{x}_{k|k,0}^{a} &= \hat{\mathbf{x}}_{k|k}^{a} \\ \boldsymbol{x}_{k|k,i}^{a} &= \hat{\mathbf{x}}_{k|k}^{a} + \left(\sqrt{(N+\kappa)\boldsymbol{\Sigma}_{\mathrm{x}_{k|k}^{a}}}\right)_i \qquad i = 1, 2, \cdots, N \\ \boldsymbol{x}_{k|k,i}^{a} &= \hat{\mathbf{x}}_{k|k}^{a} - \left(\sqrt{(N+\kappa)\boldsymbol{\Sigma}_{\mathrm{x}_{k|k}^{a}}}\right)_i \qquad i = 1, 2, \cdots, N \end{aligned} \tag{3-43}$$

The corresponding weight factors W_i, $i = 0, 1, \cdots, 2N$, are the same as those in Eq. (3-34). Using $\boldsymbol{x}_{k|k,i}^{a} = \left[\boldsymbol{x}_{k|k,i}^{\mathbf{x}} \quad \boldsymbol{x}_{k|k,i}^{\mathbf{w}} \quad \boldsymbol{x}_{k|k,i}^{\mathbf{v}}\right]^{\mathrm{T}}$, each sigma point propagates through the nonlinear system to perform the time update.

$$\boldsymbol{x}_{k+1|k,i}^{\mathbf{x}} = \boldsymbol{x}_{k|k,i}^{\mathbf{x}} + \int_{k\Delta t}^{(k+1)\Delta t} f\left(\boldsymbol{x}_{k|k,i}^{\mathbf{x}}, \mathbf{u}, \boldsymbol{x}_{k|k,i}^{\mathbf{w}}\right) dt \qquad i = 0, 1, \cdots, 2N \tag{3-44}$$

The *a priori* estimate $\hat{\mathbf{x}}_{k+1|k}$ can be calculated as the weighted average of the sigma points:

$$\hat{\mathbf{x}}_{k+1|k} = \sum_{i=0}^{2N} W_i \boldsymbol{x}_{k+1|k,i}^{\mathbf{x}} \tag{3-45}$$

The corresponding error covariance matrix $\boldsymbol{\Sigma}_{\mathbf{x}_{k+1|k}}$ can be evaluated as:

$$\boldsymbol{\Sigma}_{\mathbf{x}_{k+1|k}} = \sum_{i=0}^{2N} W_i \left(\boldsymbol{\mathcal{X}}^{\mathbf{x}}_{k+1|k,i} - \hat{\mathbf{x}}_{k+1|k}\right)\left(\boldsymbol{\mathcal{X}}^{\mathbf{x}}_{k+1|k,i} - \hat{\mathbf{x}}_{k+1|k}\right)^{\mathrm{T}} \tag{3-46}$$

Repeating Eq. (3-28) ~ Eq. (3-46), UKF can recursively update the system states for a nonlinear system.

3.2.2 The Constrained UKF

Similar to EKF, the standard UKF searches for the optimal estimates of system states through the entire unconstrained solution space. Reasonable constraints need to be incorporated in the UKF estimation process to ensure that the estimates of parameters satisfy physical laws. When n_{ac} number of inequality constraints are active $\mathbf{A}_{\mathrm{a}}\mathbf{x} - \mathbf{b}_{\mathrm{a}} = \mathbf{0}$, the same method introduced in Section 3.1.2 can be implemented to adjust Kalman gain and make sure the *a posteriori* estimate $\hat{\mathbf{x}}_{k|k}$ stays within the feasible domain. Finally, the constrained UKF (CUKF) algorithm is summarized as follows.

Initial Estimate		
State estimate	$\hat{\mathbf{x}}_{0\|-1} = \mathbb{E}[\mathbf{x}_0]$	
State covariance	$\boldsymbol{\Sigma}_{\mathbf{x}_{0\|-1}} = \mathbb{E}\left[\left(\mathbf{x}_0 - \hat{\mathbf{x}}_{0\|-1}\right)\left(\mathbf{x}_0 - \hat{\mathbf{x}}_{0\|-1}\right)^{\mathrm{T}}\right]$	
`for` $k = 0, 1, \cdots, n$		
Measurement Update		
Augmented state vector estimate	$\hat{\mathbf{x}}^a_{k\|k-1} = \begin{bmatrix}\hat{\mathbf{x}}^{\mathrm{T}}_{k\|k-1} & \mathbf{0} & \mathbf{0}\end{bmatrix}^{\mathrm{T}}$	Rept. (3-31)
Augmented state vector covariance	$\boldsymbol{\Sigma}_{\mathbf{x}^a_{k\|k-1}} = \begin{bmatrix}\boldsymbol{\Sigma}_{\mathbf{x}_{k\|k-1}} & \mathbf{0} & \mathbf{0} \\ \mathbf{0} & \boldsymbol{\Sigma}_{\mathbf{w}} & \mathbf{0} \\ \mathbf{0} & \mathbf{0} & \boldsymbol{\Sigma}_{\mathbf{v}}\end{bmatrix}$	Rept. (3-32)
Sigma points	$\boldsymbol{\mathcal{X}}^a_{k\|k-1,0} = \hat{\mathbf{x}}^a_{k\|k-1}$ $\boldsymbol{\mathcal{X}}^a_{k\|k-1,i} = \hat{\mathbf{x}}^a_{k\|k-1} + \left(\sqrt{(N+\kappa)\boldsymbol{\Sigma}_{\mathbf{x}^a_{k\|k-1}}}\right)_i \quad i = 1, 2, \cdots, N$	Rept. (3-33)

$$\boldsymbol{x}^a_{k|k-1,i} = \hat{\mathbf{x}}^a_{k|k-1} - \left(\sqrt{(N+\kappa)\boldsymbol{\Sigma}_{\mathrm{x}^a_{k|k-1}}}\right)_i \qquad i = 1, 2, \cdots, N$$

Weighting factors

$$W_0 = \frac{\kappa}{N+\kappa}$$

$$W_i = \frac{1}{2(N+\kappa)} \qquad i = 1, 2, \cdots, 2N$$

Rept. (3-34)

Measurements of sigma points

$$\boldsymbol{y}_{k|k-1,i} = h\left(\boldsymbol{x}^{\mathbf{x}}_{k|k-1,i}, \mathbf{u}_k, \boldsymbol{x}^{\mathbf{v}}_{k|k-1,i}\right)$$ Rept. (3-35)

Innovation covariance

$$\boldsymbol{\Sigma}_{\mathbf{y}_{k|k-1}} = \sum_{i=0}^{2N} W_i\left(\boldsymbol{y}_{k|k-1,i} - \hat{\mathbf{y}}_{k|k-1}\right)\left(\boldsymbol{y}_{k|k-1,i} - \hat{\mathbf{y}}_{k|k-1}\right)^{\mathrm{T}}$$ Rept. (3-37)

Cross covariance

$$\boldsymbol{\Sigma}_{\mathbf{x}\mathbf{y}_{k|k-1}} = \sum_{i=0}^{2N} W_i\left(\boldsymbol{x}^{\mathbf{x}}_{k|k-1,i} - \hat{\mathbf{x}}_{k|k-1}\right)\left(\boldsymbol{y}_{k|k-1,i} - \hat{\mathbf{y}}_{k|k-1}\right)^{\mathrm{T}}$$ Rept. (3-38)

Kalman gain

$$\tilde{\mathbf{L}}_k = \boldsymbol{\Sigma}_{\mathbf{x}\mathbf{y}_{k|k-1}}\left(\boldsymbol{\Sigma}_{\mathbf{y}_{k|k-1}}\right)^{-1}$$ Rept. (3-39)

Measurement residual

$$\mathbf{r}_k = \mathbf{y}_k - \hat{\mathbf{y}}_{k|k-1}$$ Rept. (3-40)

State estimate

$$\tilde{\mathbf{x}}_{k|k} = \hat{\mathbf{x}}_{k|k-1} + \tilde{\mathbf{L}}_k\mathbf{r}_k$$ Rept. (3-41)

Check constraints

`if` there is no active constraint

$$\mathbf{L}_k = \tilde{\mathbf{L}}_k$$

$$\hat{\mathbf{x}}_{k|k} = \tilde{\mathbf{x}}_{k|k}$$

`else if` there are active constraints $\mathbf{A}_\mathrm{a}\mathbf{x} - \mathbf{b}_\mathrm{a} = \mathbf{0}$

$$\mathbf{L}_k = \tilde{\mathbf{L}}_k - \mathbf{A}_\mathrm{a}^{\mathrm{T}}(\mathbf{A}_\mathrm{a}\mathbf{A}_\mathrm{a}^{\mathrm{T}})^{-1}\left(\mathbf{A}_\mathrm{a}\tilde{\mathbf{x}}_{k|k} - \mathbf{b}_\mathrm{a}\right)\left(\mathbf{r}_k^{\mathrm{T}}\boldsymbol{\Sigma}^{-1}_{\mathbf{y}_{k|k-1}}\mathbf{r}_k\right)^{-1}\mathbf{r}_k^{\mathrm{T}}\boldsymbol{\Sigma}^{-1}_{\mathbf{y}_{k|k-1}}$$ Rept. (3-26)

$$\hat{\mathbf{x}}_{k|k} = \tilde{\mathbf{x}}_{k|k} - \mathbf{A}_\mathrm{a}^{\mathrm{T}}(\mathbf{A}_\mathrm{a}\mathbf{A}_\mathrm{a}^{\mathrm{T}})^{-1}\left(\mathbf{A}_\mathrm{a}\tilde{\mathbf{x}}_{k|k} - \mathbf{b}_\mathrm{a}\right)$$ Rept. (3-27)

`end if`

State covariance

$$\boldsymbol{\Sigma}_{\mathbf{x}_{k|k}} = \boldsymbol{\Sigma}_{\mathbf{x}_{k|k-1}} - \mathbf{L}_k\boldsymbol{\Sigma}_{\mathbf{y}_{k|k-1}}\mathbf{L}_k^{\mathrm{T}}$$ Rept. (3-42)

Time Update

$$\boldsymbol{x}^a_{k|k,0} = \hat{\mathbf{x}}^a_{k|k}$$

Sigma points

$$\boldsymbol{x}^a_{k|k,i} = \hat{\mathbf{x}}^a_{k|k} + \left(\sqrt{(N+\kappa)\boldsymbol{\Sigma}_{\mathrm{x}^a_{k|k}}}\right)_i \qquad i = 1, 2, \cdots, N$$

$$\boldsymbol{x}^a_{k|k,i} = \hat{\mathbf{x}}^a_{k|k} - \left(\sqrt{(N+\kappa)\boldsymbol{\Sigma}_{\mathrm{x}^a_{k|k}}}\right)_i \qquad i = 1, 2, \cdots, N$$

Rept. (3-43)

Propagate sigma points

$$\boldsymbol{x}^{\mathbf{x}}_{k+1|k,i} = \boldsymbol{x}^{\mathbf{x}}_{k|k,i} + \int_{k\Delta t}^{(k+1)\Delta t} f\left(\boldsymbol{x}^{\mathbf{x}}_{k|k,i}, \mathbf{u}, \boldsymbol{x}^{\mathbf{w}}_{k|k,i}\right)dt$$ Rept. (3-44)

State vector estimate	$\hat{\mathbf{x}}_{k+1\|k} = \sum_{i=0}^{2N} W_i \boldsymbol{x}^{\mathbf{x}}_{k+1\|k,i}$	Rept. (3-45)
State vector covariance	$\boldsymbol{\Sigma}_{\mathbf{x}_{k+1\|k}} = \sum_{i=0}^{2N} W_i \left(\boldsymbol{x}^{\mathbf{x}}_{k+1\|k,i} - \hat{\mathbf{x}}_{k+1\|k}\right)\left(\boldsymbol{x}^{\mathbf{x}}_{k+1\|k,i} - \hat{\mathbf{x}}_{k+1\|k}\right)^{\mathrm{T}}$	Rept. (3-46)
`end loop`		

3.3 Numerical Studies on Model Updating

This section presents two simulation examples validating the proposed model updating methods using Kalman filters. The first example is a linear four-story shear frame structure. EKF and UKF are applied to identify damping coefficients and inter-story stiffness values of the structure. The second example is a nonlinear single degree of freedom (SDOF) Bouc-Wen hysteretic system. Various Kalman filters, including EKF, CEKF, UKF, and CUKF, are used for identifying model parameters of the nonlinear system.

3.3.1 Linear Model Updating of a Four-Story Shear Frame Structure

To investigate Kalman filters for parameter identification, the linear structural model is constructed for a four-story shear frame (Figure 3-1). The true mass, damping, and inter-story stiffness values are annotated in the figure. It is assumed that all the four DOFs are instrumented with sensor measuring acceleration at sampling frequency of 200 Hz. The covariance of the input noise is set as $\Sigma_w = (10^{-1}\ \mathrm{m/s^2})^2$, and the covariance of sensor noise is set as $\boldsymbol{\Sigma}_{\mathbf{v}} = (10^{-1}\ \mathrm{m/s^2})^2\mathbf{I}$. A scaled El Centro earthquake excitation of 40 s duration is applied to excite the structure. In this example, all the damping coefficients and inter-story stiffness values are chosen to be updated while the mass values are considered

as accurate. The initial estimates for damping coefficients are set as $c_{0|0,i} = 2\ \mathrm{N \cdot s/m}$, $i = 1,2,3,4$; the initial estimates for the inter-story stiffness values are set as $k_{0|0,i} = 1500\ \mathrm{N/m}$, $i = 1,2,3,4$. Physical laws require that both damping coefficients and inter-story stiffness values are positive, i.e. $c_i > 0$ and $k_i > 0$, $i = 1,2,3,4$. The system state-space equation is integrated through a 4th-order Runge-Kutta method to obtain the acceleration responses of all floors.

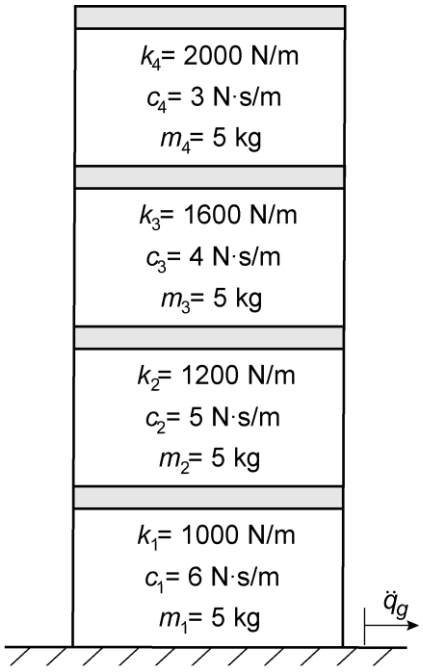

Figure 3-1 Four-story shear frame structure used for Kalman filters

Based on the described EKF and UKF algorithms, the time histories of the *a posteriori* estimates for the damping coefficients and the inter-story stiffness values are shown in Figure 3-2. The figure shows that both EKF and UKF can update the unknown parameters recursively from their initial values to the corresponding true values. The performance of EKF and UKF are similar to each other, except that the UKF estimate of c_4 is faster than the EKF estimate. In addition, the stiffness parameters converges to the

true values faster than the damping coefficients. This is because the stiffness parameters contribute more to the structural response, and thus the measurement data is more sensitive to the stiffness parameters [80]. As all estimates satisfy constraints during both EKF and UKF identification processes, there is no need to apply constrained Kalman filters on this simulation example.

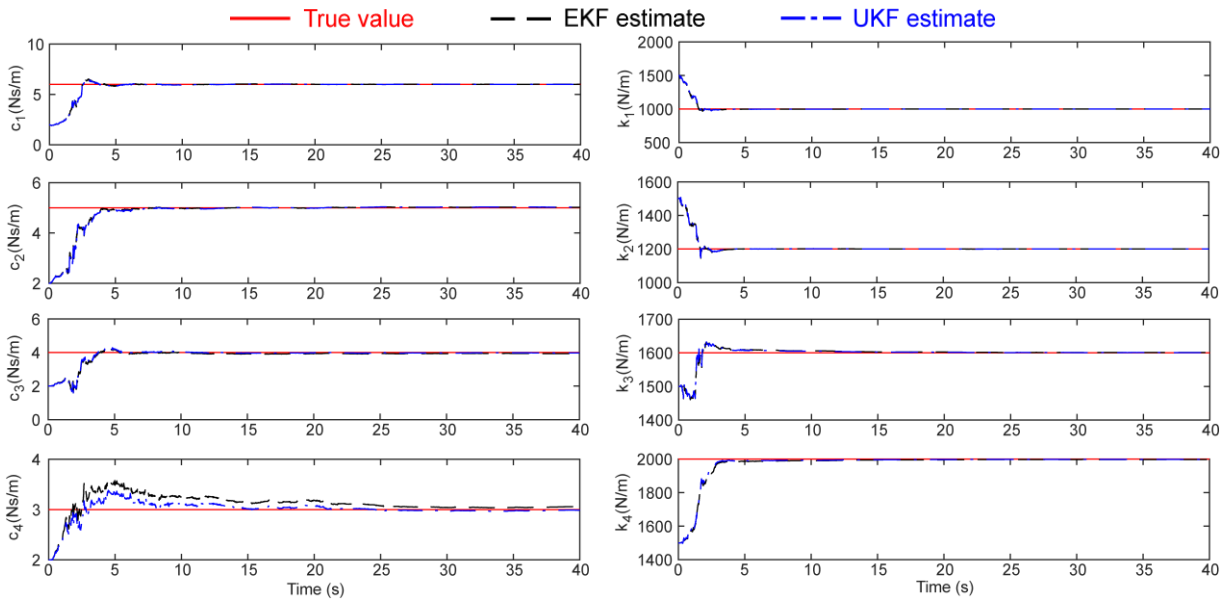

Figure 3-2 Identified results using EKF and UKF on the four-story shear frame structure

A comparison of the final estimated values using the EKF and the UKF algorithms is shown Table 3-1. The comparison shows that both the EKF and the UKF are capable of identifying the unknown model parameters of this four-story linear structure with acceptable accuracy. Overall, the estimation errors using UKF is slightly smaller than the errors using EKF.

Table 3-1 Comparison of estimation results on the four-story shear frame structure using EKF and UKF

Parameters	Actual values	EKF		UKF	
		Values	Errors (%)	Values	Errors (%)
c_1 (Ns/m)	6	6.0082	0.1364	6.0005	0.0082
c_2 (Ns/m)	5	5.0174	0.3489	5.0242	0.4831
c_3 (Ns/m)	4	3.9392	−1.5204	3.9738	−0.6548
c_4 (Ns/m)	3	3.0554	1.8470	2.9875	−0.4168
k_1 (N/m)	1,000	999.7391	−0.0261	999.7982	−0.0202
k_2 (N/m)	1,200	1200.5577	0.0465	1200.5070	0.0422
k_3 (N/m)	1,600	1601.1534	0.0721	1600.8751	0.0547
k_4 (N/m)	2,000	1997.2610	−0.1370	1997.8292	−0.1085

3.3.2 Nonlinear Model Updating of a Single-Degree-of-Freedom (SDOF) Bouc-Wen Model

The next example to investigate constrained Kalman filters for parameter identification is an SDOF Bouc-Wen hysteretic model (Figure 3-3). The governing equation of the system with mass m, damping coefficient c, stiffness k and ground excitation $\ddot{q}_g$ is shown as:

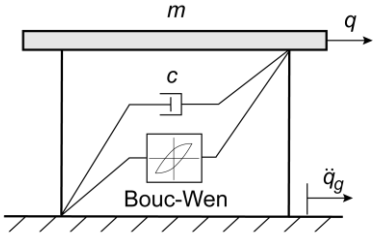

Figure 3-3 Bouc-Wen hysteretic system with viscous damping

$$m\ddot{q}(t) + c\dot{q}(t) + kz(t) = -m\left(\ddot{q}_g(t) + w\right) \tag{3-47}$$

Here the excitation to the system is $u = -m\ddot{q}_g(t)$, and the ground acceleration input $\ddot{q}_g(t)$ is contaminated with uncertainty w. The nonlinear restoring force is $r = kz(t)$, and z is a hidden hysteretic displacement. A first-order differential equation describes the hysteretic displacement:

$$\dot{z} = \dot{q} - \beta|\dot{q}||z|^{n-1}z - \gamma\dot{q}|z|^n = \dot{q}\left(1 - |z|^n\left(\gamma + \beta\text{sgn}(z\dot{q})\right)\right) \tag{3-48}$$

Here β, γ, and n are dimensionless parameters controlling the shape and magnitude of the hysteresis loop; $\text{sgn}(\cdot)$ is the signum function. This differential model has many advantages in describing nonlinear hysteresis. By adjusting the parameters, this model is capable of generating a large variety of hysteretic loops. In order to identify proper values for the Bouc-Wen parameters, constrained Kalman filters (CEKF and CUKF) are used to search parameter values using real-time dynamic response data.

3.3.2.1 Differentiable Bouc-Wen Model

Notice that the model equation Eq. (3-48) is not differentiable at $\dot{q} = 0$ or $z = 0$, and this singularity is not ideal for the linearization in EKF. Three reasons causing the non-differentiability are discussed as follows.

(i) Derivative of the signum function $\text{sgn}(a)$ with respect to a and derivative of the absolute value function $|a|$ with respect to a

As the absolute function $|a| = \text{sgn}(a)\, a$, it suffices to only discuss the derivative of the signum function $\text{sgn}(a)$. This derivative is not defined at $a = 0$. In order to address this problem, the hyperbolic tangent function $\tanh(\cdot)$ can be adopted to approximate the signum function $\text{sgn}(\cdot)$.

$$\text{sgn}(a) \approx \tanh(\rho a) \tag{3-49}$$

Here $\rho > 0$ is a factor controlling the curvature. Figure 3-4 shows the plot of $\tanh(\rho a)$ with different values of ρ. When the value of ρ is larger, the differentiable function $\tanh(\rho a)$ better approximates $\text{sgn}(a)$.

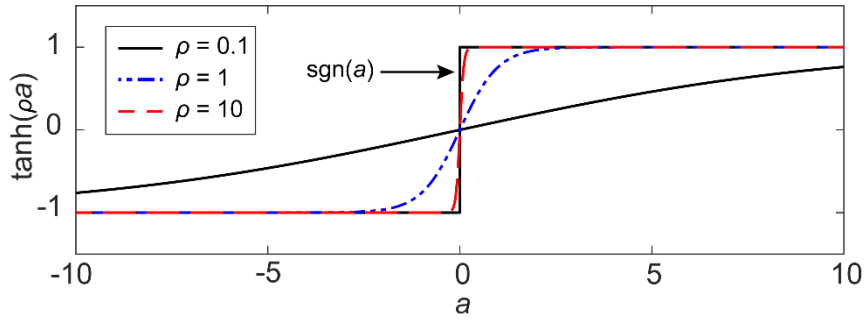

Figure 3-4 Plot of $\tanh(\rho a)$

Using this approximation, the Bouc-Wen equation is then modified as:

$$\dot{z} = \dot{q}\left(1 - (\tanh(\rho z)\, z)^n (\gamma + \beta \tanh(\rho z \dot{q}))\right) \tag{3-50}$$

(ii) Derivative of the exponential function a^b with respect to a $(b < 1)$

For the term $f = (\tanh(\rho z)\, z)^n$ in Eq. (3-50), $\frac{\partial f}{\partial z}$ requires taking derivative with respect to the base. The derivative of the exponential function a^b with respect to a is

calculated as $\frac{\partial}{\partial a}a^b = ba^{b-1}$. When $b < 1$, the derivative is undefined at $a = 0$. To avoid this singular point, we can simply require $b \geq 1$. Applying this constraint on the state equation of the Bouc-Wen model requires $n \geq 1$, which satisfies most of engineering applications.

(iii) Derivative of the exponential function a^b with respect to b ($a = 0$)

For the term $f = (\tanh(\rho z)\, z)^n$ in Eq. (3-50), $\frac{\partial f}{\partial n}$ requires taking derivative with respect to the power. The derivative of the exponential function a^b with respect to b is calculated as $\frac{\partial}{\partial b}a^b = a^b \ln a$, which is not defined for $a \leq 0$. In the system equation Eq. (3-50), the base of exponential functions is $\tanh(\rho z)\, z$ which is always nonnegative. Therefore, we only need to consider the case $a = 0$. Note that in (ii), we require $b \geq 1$. Using L'Hospital's rule, the limit of the function $a^b \ln a$, as a approaches 0^+ can be calculated as:

$$\lim_{a\to 0^+} a^b \ln a = \lim_{a\to 0^+} \frac{\ln a}{a^{-b}} = \lim_{a\to 0^+} \frac{a^{-1}}{-ba^{-b-1}} = \lim_{a\to 0^+} \frac{a^b}{-b} = 0 \tag{3-51}$$

In the application of EKF, we define the derivative $\frac{\partial}{\partial b}a^b = 0$ at $a = 0$.

To demonstrate the effectiveness of the proposed differentiable Bouc-Wen model, simulation on an SDOF nonlinear hysteretic system (Figure 3-3) is conducted. In this simulation example, system parameters are set as $m = 1$ kg, $c = 0.3$ Ns/m, $k = 12$ N/m, $\beta = 2$, $\gamma = 1$, and $n = 2$. In the differentiable Bouc-Wen model, the curvature controlling parameter is set as $\rho = 100$. A scaled El Centro earthquake excitation of 40 s duration is

applied to excite the system. Figure 3-5 plots the displacement q, velocity $\dot{q}$, hysteretic displacement z, and the hysteretic loops using the original Bouc-Wen model (Eq. (3-48)) and the differentiable Bouc-Wen model (Eq. (3-50)). The dynamical responses and hysteretic loops of the two model are almost the same to each other. The simulated results indicate that the proposed differentiable Bouc-Wen model is capable of capturing the hysteretic behaviors of the system with acceptable accuracy. In the discussion afterwards, the proposed differentiable Bouc-Wen model will be adopted for parameter identification.

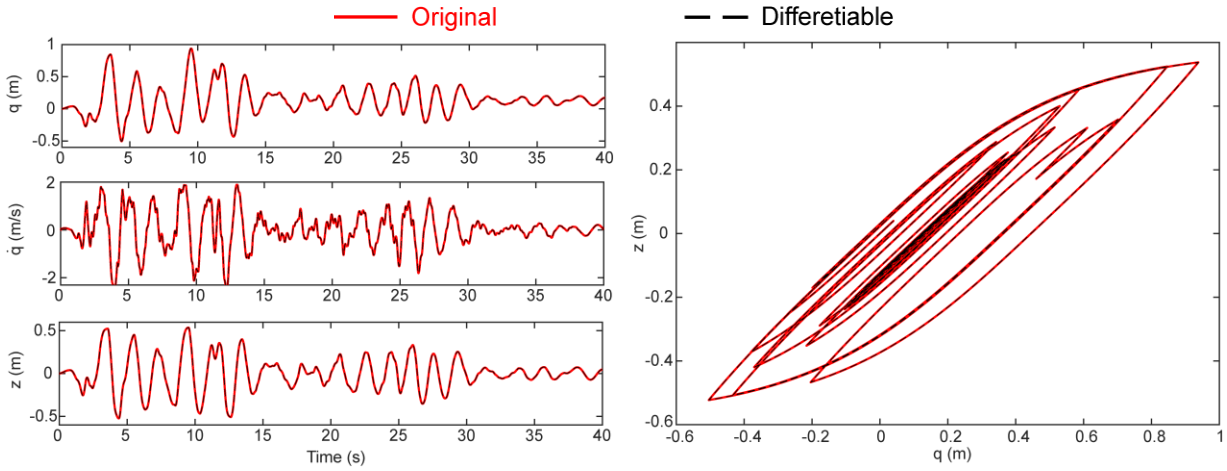

Figure 3-5 Structural responses of the SDOF Bouc-Wen hysteretic system

3.3.2.2 Parameter Identification Using EKF and CEKF

In this parameter identification example, the values of system parameters and excitation are the same as in Section 3.3.2.1. The mass m is treated as accurate and other parameters are chosen for identification. The model parameters are summarized in Table 3-2.

Table 3-2 Model parameters of the SDOF Bouc-Wen system

Parameters	Actual values	Initial values
c (Ns/m)	0.3	0.15
k (N/m)	12	6
β	2	1
γ	1	0.5
n	2	4

The state-space system equation for parameter identification can be formulated as:

$$\mathbf{x} = \begin{pmatrix} q \\ \dot{q} \\ z \\ c \\ k \\ \beta \\ \gamma \\ n \end{pmatrix} \quad \dot{\mathbf{x}} = f(\mathbf{x}, \ddot{q}_g, w) = \begin{pmatrix} \dot{q} \\ -(\ddot{q}_g + w) - (c\dot{q} + kz)/m \\ \dot{q}\left(1 - (\tanh(\rho z)\, z)^n(\gamma + \beta \tanh(\rho z \dot{q}))\right) \\ 0 \\ 0 \\ 0 \\ 0 \\ 0 \end{pmatrix} \tag{3-52}$$

The absolute acceleration of the mass is measured at $t = k\Delta t$ and the measurement equation is given as:

$$y_k = -(c\dot{q}_k + kz_k)/m + v_k \tag{3-53}$$

The covariance of the process noise is set as $\Sigma_w = (10^{-2}\ \mathrm{m/s^2})^2$, and the covariance of sensor noise is set as $\Sigma_v = (10^{-2}\ \mathrm{m/s^2})^2$. Model parameters are identified using EKF and CEKF first. In the identification process, the linearization of system equation $\boldsymbol{f}$ (Eq. (3-52)) and measurement equation $\boldsymbol{h}$ (Eq. (3-53)) uses analytically derived partial derivatives.

For CEKF, inequality constraints applied on the parameters are listed as follows [81]:

$$c \geq 0, \qquad k \geq 0, \qquad \beta + \gamma \geq 0, \qquad \beta - \gamma \geq 0, \qquad n \geq 1 \tag{3-54}$$

Using the EKF and CEKF algorithms, the parameters of the nonlinear Bouc-Wen hysteretic system are identified together with the original system states, including displacement, velocity, and hysteretic displacement. Figure 3-6 shows the time histories of the *a posteriori* estimates of the parameters and the system states. Except for the damping parameter c and the stiffness parameter k, all the other parameters cannot be updated correctly by EKF. On the other hand, the proposed CEKF can recursively update all the parameters from their initial values to the corresponding true values. The constraints can

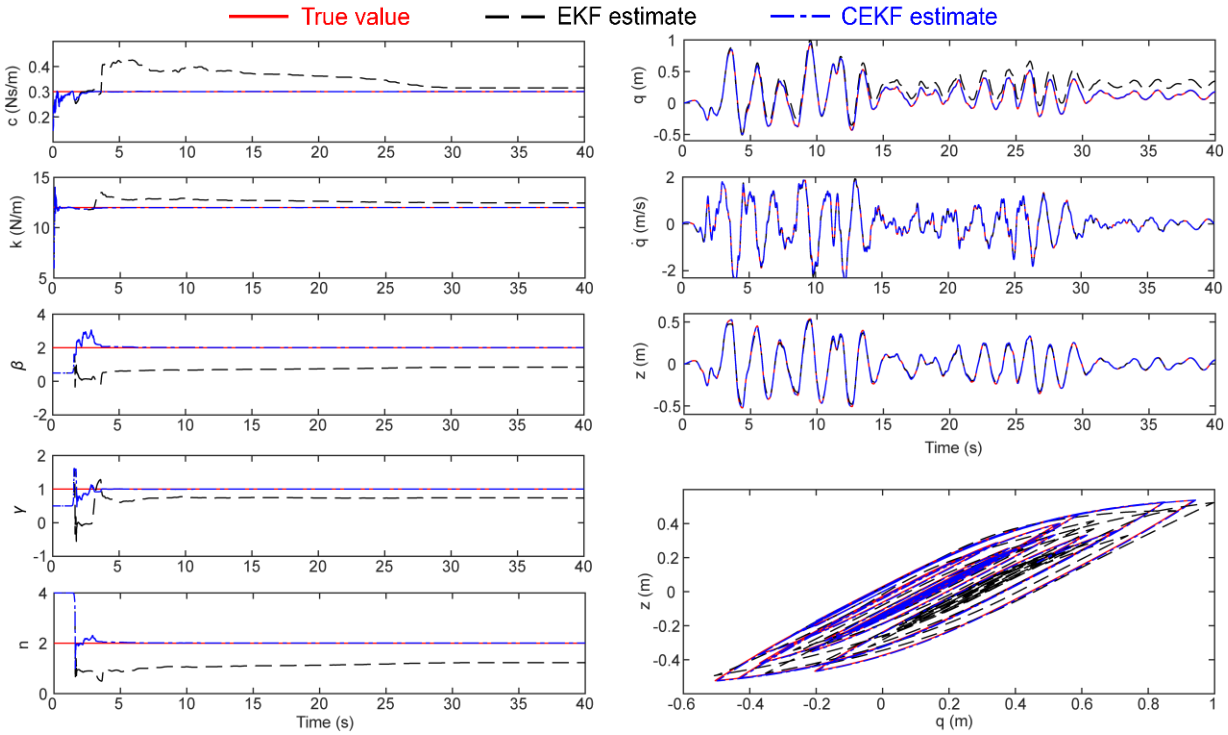

Figure 3-6 Updating results on the SDOF Bouc-Wen hysteretic model using EKF and CEKF

effectively prevent the estimates from being unreasonable values. The estimates of stiffness parameter k and damping coefficient c converge faster than the estimates of hysteretic parameters, which remain not updated and change rapidly after about 2 seconds. This is because the structure has not exhibited nonlinear behavior within the first 2 seconds of the estimation process. The plots show that after about 4 seconds, all the CEKF estimates reach values quite close to the true values.

Similar to the estimation of parameters, the estimated states and hysteretic loop from the proposed CEKF match well with the actual states and hysteretic loop, respectively. In Figure 3-6, the CEKF curves of states and hysteretic loop and the actual value curves overlap with each other. On the other hand, EKF can provide accurate estimates for velocity $\dot{q}$ and hysteretic displacement z, while the estimate of displacement q suffers slow drift over time during the model updating process, and results in an inaccurate hysteretic loop.

A comparison of the final estimated values using different identification algorithms is summarized in Table 3-3. EKF estimation errors of all the hysteretic parameters are greater than 25%. The difficulty of EKF identifying parameters of highly nonlinear systems

Table 3-3 Comparison of estimation results on the SDOF Bouc-Wen hysteretic model using EKF and CEKF

Parameters	Actual values	EKF		CEKF	
		Values	Errors (%)	Values	Errors (%)
c (Ns/m)	0.3	0.3149	4.9603	0.3007	0.2185
k (N/m)	12	12.4596	3.8297	11.9958	−0.0353
β	2	0.8424	−57.8792	2.0109	0.5464
γ	1	0.7389	−26.1072	1.0026	0.2634
n	2	1.2313	−38.4326	2.0080	0.4011

has also been reported by other researchers [53]. On the other hand, the proposed CEKF is capable of accurately identifying model parameter values; all estimation errors are within $\pm 1\%$. This simulation example shows that the proposed CEKF outperforms EKF when applied for parameter identification of highly nonlinear systems.

3.3.2.3 Parameter identification using UKF and CUKF

The same problem is solved by UKF and CUKF. For CUKF, the same inequality constraints Eq. (3-54) are applied during the identification process. Using the UKF and CUKF algorithms, the parameters of the nonlinear Bouc-Wen hysteretic system are identified together with the original system states, including displacement, velocity, and hysteretic displacement. Figure 3-7 shows the time histories of the *a posteriori* estimates

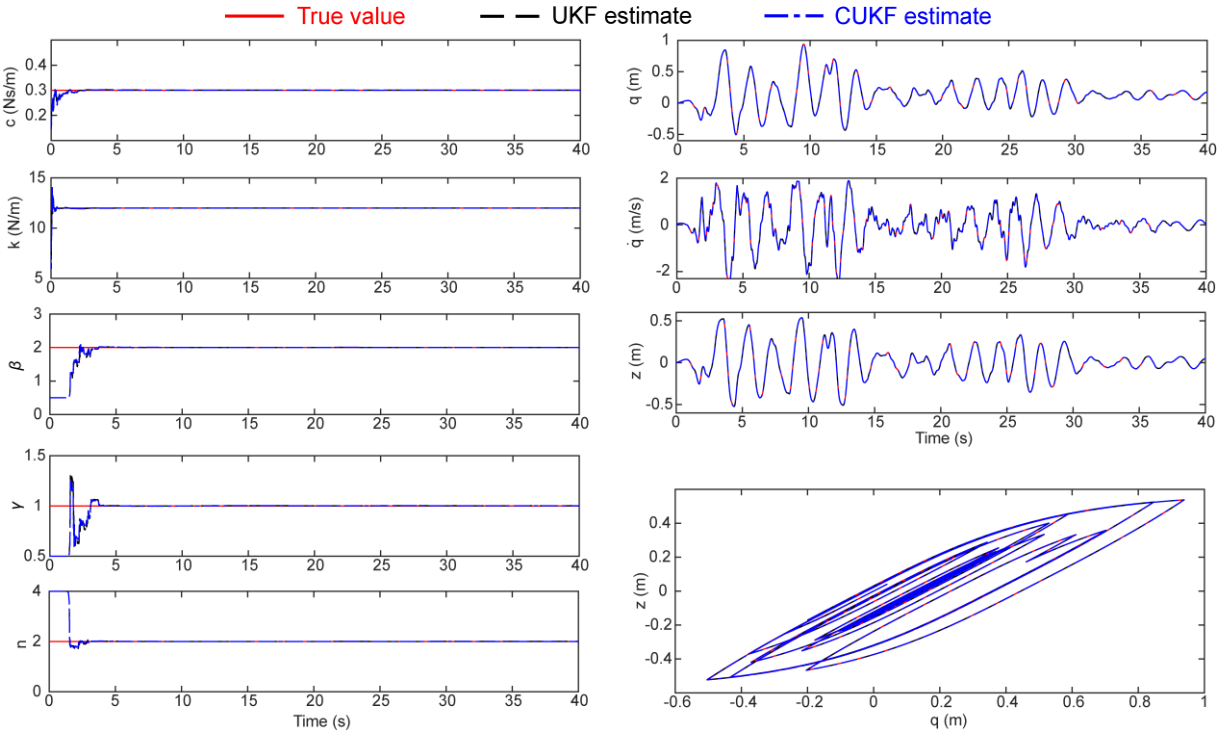

Figure 3-7 Updating results on the SDOF Bouc-Wen hysteretic model using UKF and CUKF

of the parameters and the system states. Both UKF and the proposed CUKF can recursively update all the parameters from their initial values to the corresponding true values. Most of the UKF curves and CUKF curves overlap with each other, except for the estimates of β and γ during time span 2 ~ 4 s. It shows that CUKF algorithm can effectively prevent the estimates from violating constraints. Like CEKF, the estimates of stiffness parameter k and damping coefficient c converge faster than the estimates of hysteretic parameters, which remain not updated and change rapidly after about 2 seconds. Similar to the estimation of parameters, the estimated states and hysteretic loop from both UKF and the proposed CUKF match well with the actual states and hysteretic loop, respectively.

A comparison of the final estimated values using different identification algorithms is summarized in Table 3-4. Both UKF and CUKF can achieve accurate model parameter values. All estimation errors of UKF are within $\pm 0.3\%$; all estimation errors of CUKF are within $\pm 0.2\%$. This simulation example shows that considering constraints during UKF estimation process can slightly improve the accuracy of the identification results.

Table 3-4 Comparison of estimation results on the SDOF Bouc-Wen hysteretic model using UKF and CUKF

Parameters	Actual values	UKF		CUKF	
		Values	Errors (%)	Values	Errors (%)
c (Ns/m)	0.3	0.3003	0.1092	0.3002	0.0828
k (N/m)	12	11.9987	−0.0111	11.9987	−0.0107
β	2	2.0044	0.2177	2.0042	0.2109
γ	1	1.0024	0.2352	1.0021	0.2135
n	2	2.0034	0.1707	2.0032	0.1592

3.4 Summary

This chapter investigates model updating using constrained Kalman filters. Model parameters can be recursively updated, together with system states, from noisy measurement data through nonlinear variants of Kalman filters, especially the extended Kalman filter (EKF) and the unscented Kalman filter (UKF). Incorporating constraints from physical laws during the updating process can effectively prevent estimates of parameters from being unrealistic. Details of the constrained EKF (CEKF) and the constrained UKF (CUKF) are provided.

Numerical simulations are conducted to validate the proposed methods. Model updating of the four-story shear frame structure has shown that both EKF and UKF can reliably update the model parameters to the corresponding true values, and all estimates satisfy the constraints during the identification processes. The SDOF example with Bouc-Wen hysteresis demonstrates that EKF can easily result in unreliable estimates of model parameters due to large linearization error for the highly nonlinear system. Comparing to EKF, CEKF can effectively prevent the estimates of model parameters from being unrealistic and finally provide reasonable estimates by applying constraints on parameters during the estimation process. In addition, both UKF and CUKF can achieve accurate updating results for model parameters of the hysteretic system. Considering constraints during UKF estimation process can slightly improve the accuracy of the identification results.

CHAPTER 4. EXPERIMENTAL VALIDTION OF MODEL UPDATING APPROACHES ON A FOUR-STORY SHEAR STRUCTURE

To compare the proposed model updating methods, this chapter presents the laboratory experiment with a four-story shear structure. The methods include the SOS optimization from Chapter 2 that minimizes modal dynamic residuals and constrained Kalman filters from Chapter 3. Dynamical responses of the structure and base excitation are measured by accelerometers and displacement sensors. Modal properties of the shear structure are extracted from the acceleration data through the eigensystem realization algorithm (ERA). The acceleration data are also used in constrained Kalman filters for identifying model parameters. The displacement data are added for evaluating the performance of model updating methods.

To apply the modal dynamic residual formulation, a 4-DOF linear model is built and the SOS optimization is conducted to update the stiffness variables from the experimentally obtained modal properties. As for constrained Kalman filters, a 4-DOF nonlinear model with Bouc-Wen hysteresis is built. Based on this nonlinear model and experimental acceleration data, model parameters, including damping coefficients, inter-story stiffness parameters, and hysteresis parameters, are recursively updated together with the system states. The performance of various model updating methods are evaluated and compared through simulating the dynamical responses of the shear structure using the updated model parameters.

4.1 Test Structure

The four-story shear structure is made of aluminum alloy with rigid plates as floors and flexible strips as columns (Figure 4-1). The total height of the structure is 1.182 m. The weight of each floor is measured by scale. The structure is mounted on a shake table which provides horizontal base excitation. An accelerometer (#0) and a displacement sensor (#0) are installed at base to measure the excitation signal generated by the modal shaker. In addition, accelerometers (#1~#4) and displacement sensors (#1~#4) are instrumented to measure dynamic responses of the structure. The sampling frequency of sensors is set as 200 Hz. Since complete sensor measurement is available from all the four DOFs, we can extract all four resonance frequencies, damping ratios, and mode shapes of this 4-DOF model structure.

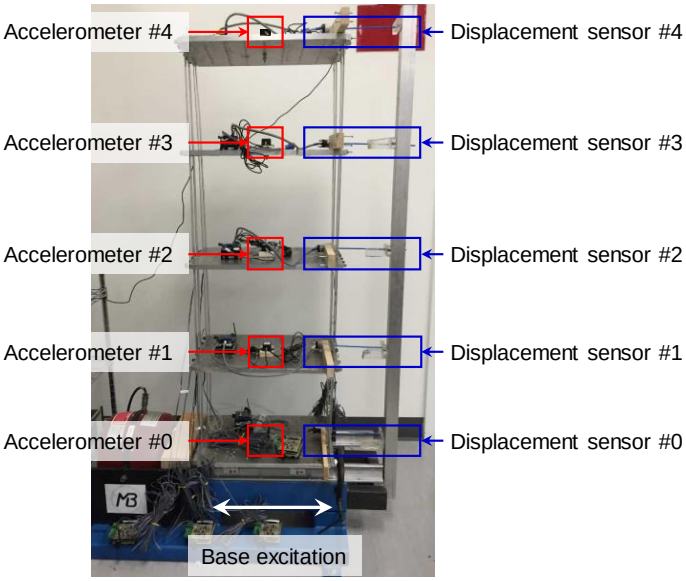

Figure 4-1 Experiment setup of the four-story shear structure

To excite the structure, a scaled chirp signal from 0 Hz to 10 Hz is generated as ground excitation. The measured ground acceleration and displacement and structural responses of each story relative to the ground are shown in Figure 4-2. The eigensystem realization

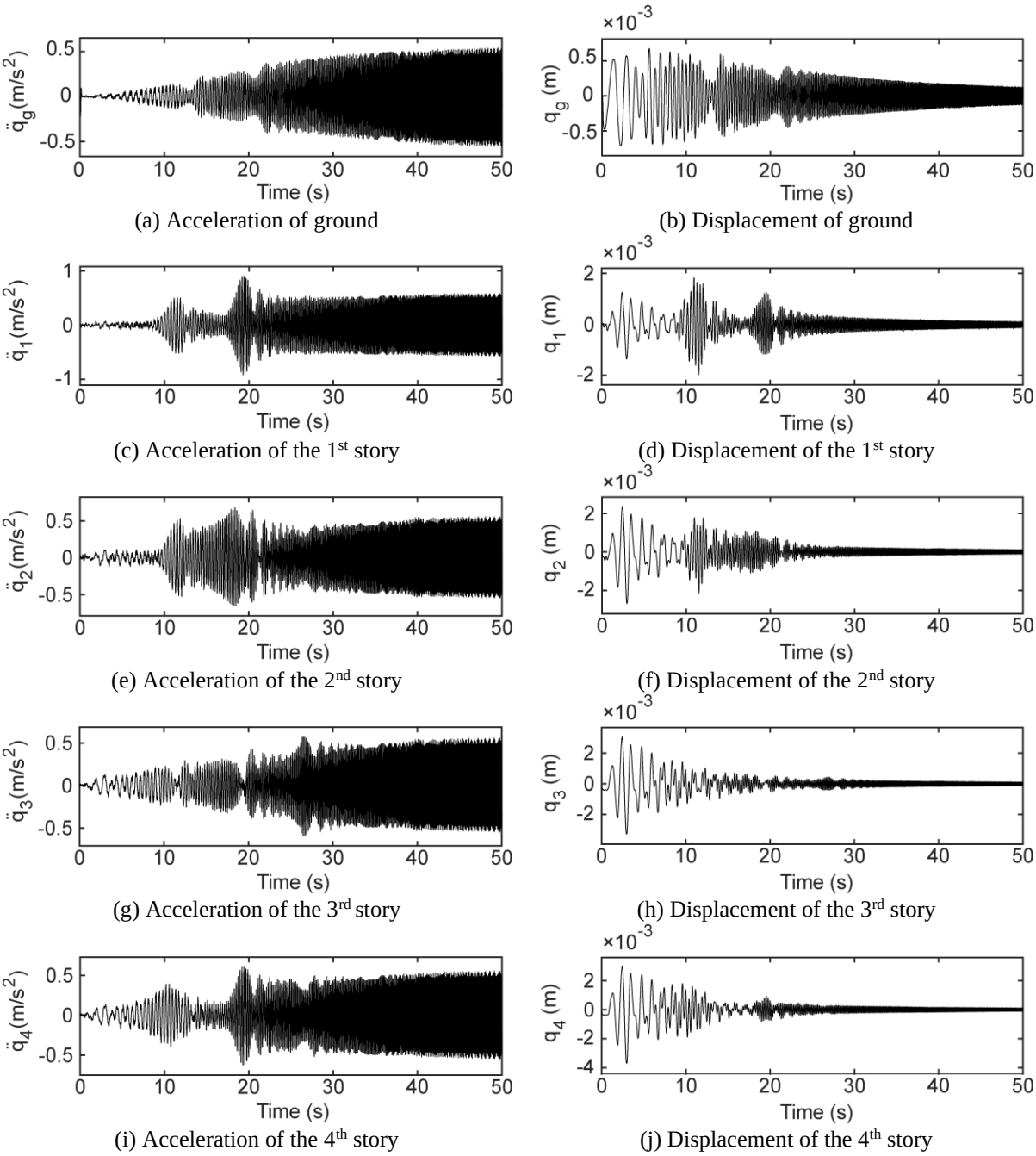

(a) Acceleration of ground (b) Displacement of ground

(c) Acceleration of the 1st story (d) Displacement of the 1st story

(e) Acceleration of the 2nd story (f) Displacement of the 2nd story

(g) Acceleration of the 3rd story (h) Displacement of the 3rd story

(i) Acceleration of the 4th story (j) Displacement of the 4th story

Figure 4-2 Measured accelerations and displacements

algorithm (ERA) [82] is applied to extract modal properties of the shear structure from the acceleration data. Figure 4-3 plots the mode shapes of all the four modes of the shear structure. Identified resonance frequencies and damping ratios are annotated in the figure. The extracted modal properties agree with expectation for a four-story shear structure.

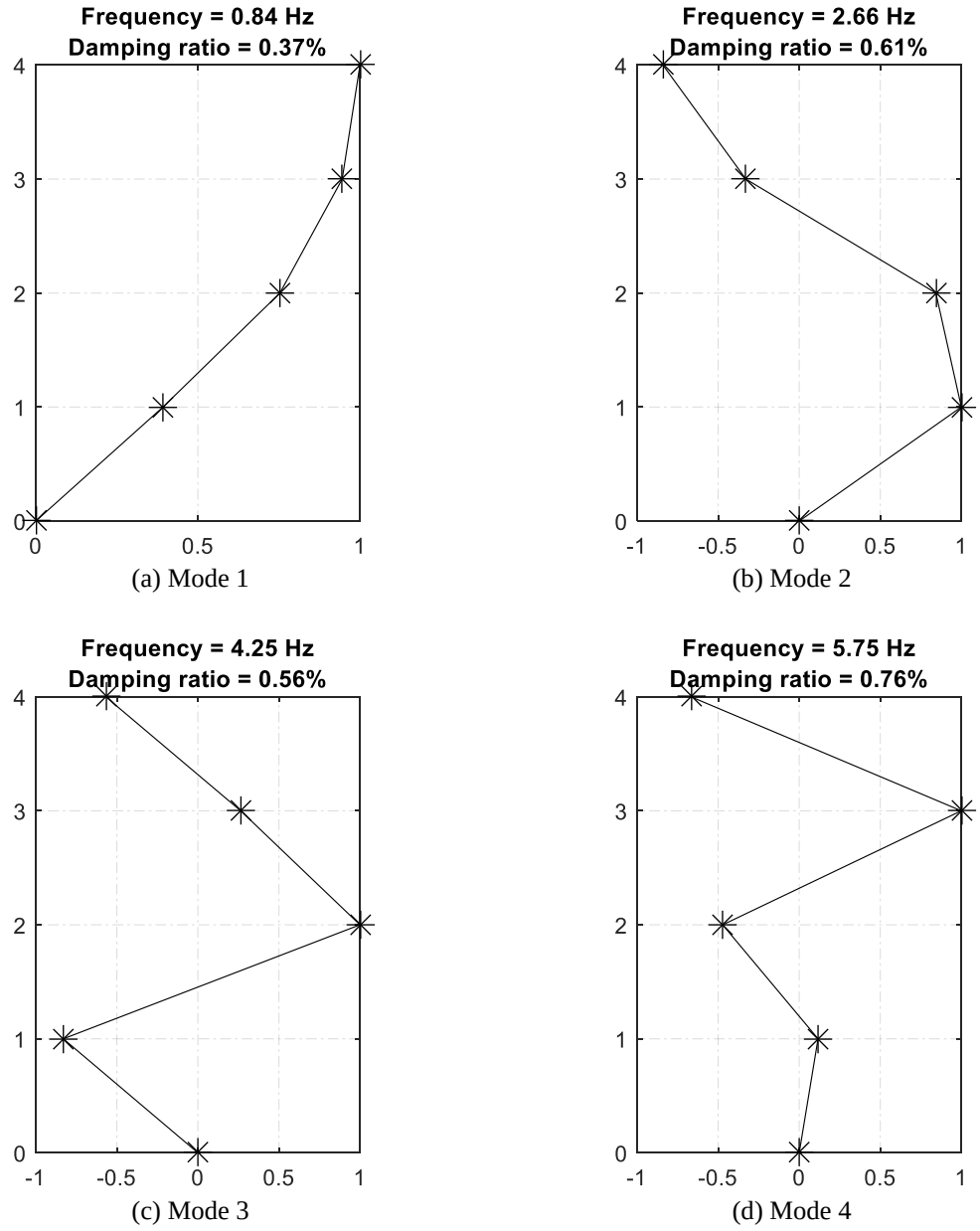

(a) Mode 1 (b) Mode 2

(c) Mode 3 (d) Mode 4

Figure 4-3 Modal properties of the four-story shear structure

4.2 Linear Model Updating Using SOS Optimization Method

The four-story shear structure is simulated as a four-DOF linear model first. In this model updating problem, only the inter-story stiffness parameters are updated. Considered as accurate, the mass of each floor is weighted by a scale and found to be 5 kg. All the four initial/nominal inter-story stiffness parameters are set as 1.5 kN/m prior to model updating. To update all the four stiffness parameters, updating (vector) variable $\boldsymbol{\theta} \in \mathbb{R}^4$ is introduced in the optimization problem. Each θ_i represents the relative change of a stiffness parameter k_i in kN/m from the initial value, i.e. $\theta_i = (k_i - 1.5)/1.5$, $i = 1, 2, 3, 4$.

In this example, all four vibration modes shown in Figure 4-3 are available for model updating, i.e. $n_{\text{modes}} = 4$. As all DOFs are instrumented with sensors, the modal dynamic residual formulation degenerates to a convex optimization problem as follows:

$$\begin{aligned} &\underset{\boldsymbol{\theta}}{\text{minimize}} \;\; r = \sum_{i=1}^{4} \left\| [\mathbf{K}(\boldsymbol{\theta}) - \omega_i^2 \mathbf{M}] \boldsymbol{\psi}_i \right\|_2^2 \\ &\text{subject to} \;\; \mathbf{L}_{\boldsymbol{\theta}} \leq \boldsymbol{\theta} \leq \mathbf{U}_{\boldsymbol{\theta}} \end{aligned} \tag{4-1}$$

The lower bound for variable $\boldsymbol{\theta} \in \mathbb{R}^4$ is set as $\mathbf{L}_{\boldsymbol{\theta}} = -\mathbf{1}_{4\times 1}$ (meaning the lowest possible stiffness parameter value is 0) and the upper bound is set as $\mathbf{U}_{\boldsymbol{\theta}} = \mathbf{1}_{4\times 1}$ (meaning the highest possible stiffness parameter value is twice the initial/nominal value).

To conduct model updating, both the SOS optimization method and two local optimization algorithms (Gauss-Newton algorithm and trust-region-reflective algorithm) are adopted to solve the problem Eq. (2-3). After the optimal solution $\boldsymbol{\theta}^*$ is solved, the updated stiffness parameters can be calculated using the nominal values. Table 4-1

summarizes the updated inter-story stiffness parameters obtained from different optimization methods. The updating results agree with expectation that due to the convexity of problem Eq. (2-3), both Gauss-Newton algorithm and trust-region-reflective algorithm converge at the same optimal solution point as the SOS optimization method. In addition, the updated inter-story stiffness values of lower stories are much less than that of the top story, because of the significant *P*-Δ effect of the structure.

Table 4-1 Updated inter-story stiffness parameters (Unit: kN/m)

Parameters	Gauss-Newton	Trust-region-reflective	SOS
k_1	1.0358	1.0358	1.0358
k_2	1.2495	1.2495	1.2495
k_3	1.5187	1.5187	1.5187
k_4	2.5620	2.5620	2.5620

Using the optimal inter-story stiffness parameters, an updated numerical model can be constructed. Table 4-2 compares the modal properties extracted from experimental data and calculated from the updated model. Because the updated stiffness values are the same from different optimization algorithms, only one column of "updated model" is provided for all algorithms. Besides resonance frequencies, the modal assurance criterion (MAC) value is provided qualifying the similarity between each experimentally extracted mode shape $\boldsymbol{\psi}_i^{\mathrm{EXP}}$ and the numerically simulated mode shape $\boldsymbol{\psi}_i$. The MAC value is calculated as:

$$\mathrm{MAC} = \frac{\left(\left(\boldsymbol{\psi}_i^{\mathrm{EXP}}\right)^{\mathrm{T}}\boldsymbol{\psi}_i\right)^2}{\left\|\boldsymbol{\psi}_i^{\mathrm{EXP}}\right\|_2^2\|\boldsymbol{\psi}_i\|_2^2} \tag{4-2}$$

where $\|\cdot\|_2$ denotes the ℓ_2-norm. A MAC value closer to 1 indicates the collinearity of two vectors; a MAC value closer to 0 indicates the orthogonality of two vectors. The comparison demonstrates that the updated model achieves closer modal properties to the experimental ones, i.e. lower Δf_i and higher MAC values.

Table 4-2 Comparison of experimental and simulated modal properties

Modes	Experimental results	Initial model			Updated model		
	f_i^{EXP} (Hz)	f_i (Hz)	Δf_i (%)	MAC	f_i (Hz)	Δf_i (%)	MAC
1st mode	0.8435	0.9574	13.5047	0.9969	0.8591	1.8564	0.9991
2nd mode	2.6605	2.7566	3.6133	0.9506	2.7412	3.0325	0.9845
3rd mode	4.2515	4.2234	−0.6614	0.6565	4.2750	0.5509	0.9945
4th mode	5.7484	5.1808	−9.8746	0.7053	5.7207	−0.4822	0.9996

4.3 Nonlinear Model Updating Using Constrained Kalman Filters

4.3.1 EKF and CEKF Model Updating

In the time domain model updating, each inter-story element of the shear structure is modeled with viscous damping and hysteresis as shown in Figure 4-4. The hysteretic force within the *i*-th story is $k_i z_i$, where the hysteretic displacement z_i is described by the differentiable Bouc-Wen model.

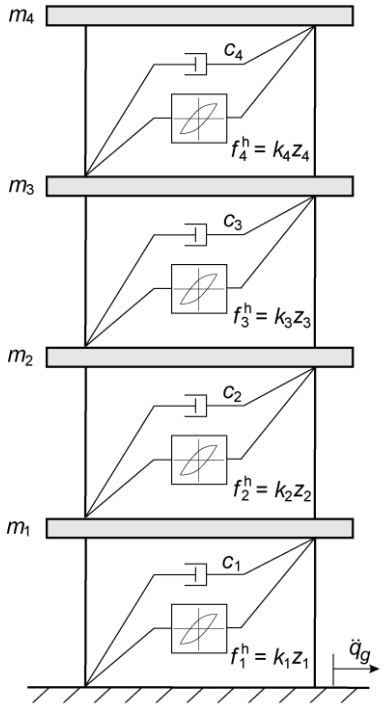

Figure 4-4 Four-story shear structure with viscous damping and hysteresis

$$\dot{z}_i = \begin{cases} \dot{q}_i\left(1 - (\tanh(\rho z_i) z_i)^n [\gamma + \beta \tanh(\rho z_i \dot{q}_i)]\right) & i = 1 \\ (\dot{q}_i - \dot{q}_{i-1})\left(1 - (\tanh(\rho z_i) z_i)^n \left[\gamma + \beta \tanh\left(\rho z_i (\dot{q}_i - \dot{q}_{i-1})\right)\right]\right) & i = 2,3,4 \end{cases} \quad (4\text{-}3)$$

The equation of motion for this four-story structure with nonlinear hysteresis can be expressed as:

$$\mathbf{M}\ddot{\mathbf{q}} + \mathbf{C}\dot{\mathbf{q}} + \mathbf{K}\mathbf{z} = -\mathbf{M}\boldsymbol{\iota}\left(\ddot{q}_g + w\right) \quad (4\text{-}4)$$

where $\mathbf{q} \in \mathbb{R}^4$ is the displacement vector, $\mathbf{z} \in \mathbb{R}^4$ is the hysteretic displacement vector with each z_i described by Eq. (4-3), $\mathbf{M} \in \mathbb{R}^{4\times4}$ is the mass matrix, $\mathbf{C} \in \mathbb{R}^{4\times4}$ is the damping matrix, $\boldsymbol{\iota} = \{\mathbf{1}\} \in \mathbb{R}^4$ is the influence vector, $\ddot{q}_g \in \mathbb{R}$ is the ground acceleration, $w \in \mathbb{R}$ is the input uncertainty, and $\mathbf{K}$ contains the inter-story stiffness values. Note that this definition of $\mathbf{K}$ and the definition of $\mathbf{z}$ in Eq. (4-3) together describe the effect of inter-

story hysteretic forces in the equations of motion. Thus, the definition is different from the typical linear stiffness matrix of a 4-DOF structure:

$$\mathbf{K} = \begin{pmatrix} k_1 & -k_2 & & \\ & k_2 & -k_3 & \\ & & k_3 & -k_4 \\ & & & k_4 \end{pmatrix} \tag{4-5}$$

The state-space system equation for parameter identification can be formulated as:

$$\mathbf{x} = \begin{pmatrix} \mathbf{q} \\ \dot{\mathbf{q}} \\ \mathbf{z} \\ \mathbf{c} \\ \mathbf{k} \\ \beta \\ \gamma \\ n \end{pmatrix} \qquad \dot{\mathbf{x}} = \boldsymbol{f}(\mathbf{x}, \ddot{q}_g, w) = \begin{pmatrix} \dot{\mathbf{q}} \\ -\mathbf{M}^{-1}(\mathbf{C}\dot{\mathbf{q}} + \mathbf{K}\mathbf{z}) - \boldsymbol{\iota}(\ddot{q}_g + w) \\ \dot{\mathbf{z}} \\ \mathbf{0} \\ \mathbf{0} \\ 0 \\ 0 \\ 0 \end{pmatrix} \tag{4-6}$$

Here $\dot{\mathbf{z}}$ is determined by Eq. (4-3). Acceleration data is used for model updating. At the *k*-th time step, the absolute accelerations of all floors are measured as $\mathbf{y}_k \in \mathbb{R}^4$:

$$\mathbf{y}_k = -\mathbf{M}^{-1}(\mathbf{C}\dot{\mathbf{q}}_k + \mathbf{K}\mathbf{z}_k) + \mathbf{v}_k \tag{4-7}$$

The covariance of the process noise is set as $\Sigma_w = (3.5 \times 10^{-3}\ \mathrm{m/s^2})^2$, and the covariance of sensor noise is set as $\boldsymbol{\Sigma}_\mathbf{v} = (3.5 \times 10^{-3}\ \mathrm{m/s^2})^2\mathbf{I}$.

To identify the model parameters together with the system states, EKF and CEKF introduced in Chapter 3 are conducted. Again, considered as accurate, the mass of each floor is 5 kg. Damping coefficients c_i, stiffness parameters k_i, and hysteretic parameters β, γ, and n are identified through the measurement data. The initial estimates are set as

$c_{i,0|-1} = 5$ Ns/m, $k_{i,0|-1} = 1.5$ kN/m, $\beta_{0|-1} = 0.5$, $\gamma_{0|-1} = 0.5$, and $n_{0|-1} = 4$. For CEKF, inequality constraints applied on the parameters are listed as follows:

$$c_i \geq 0, \qquad k_i \geq 0, \qquad \beta + \gamma \geq 0, \qquad \beta - \gamma \geq 0, \qquad n \geq 1 \tag{4-8}$$

Figure 4-5 plots the time histories of the *a posteriori* parameter estimates of the four-story shear structure using EKF and CEKF on experimental data. The estimates of damping coefficients and stiffness parameters start updating from the beginning of vibration. After significant changes during time span from about 10 s to 20 s, the estimates gradually converge to constant values. It is observed that the updating results of EKF and CEKF on damping coefficients and stiffness parameters are close to each other. However, it should be noted that estimates generated from CEKF always stay within the feasible domain, while some estimates from EKF fail to satisfy the constraints during the identification process.

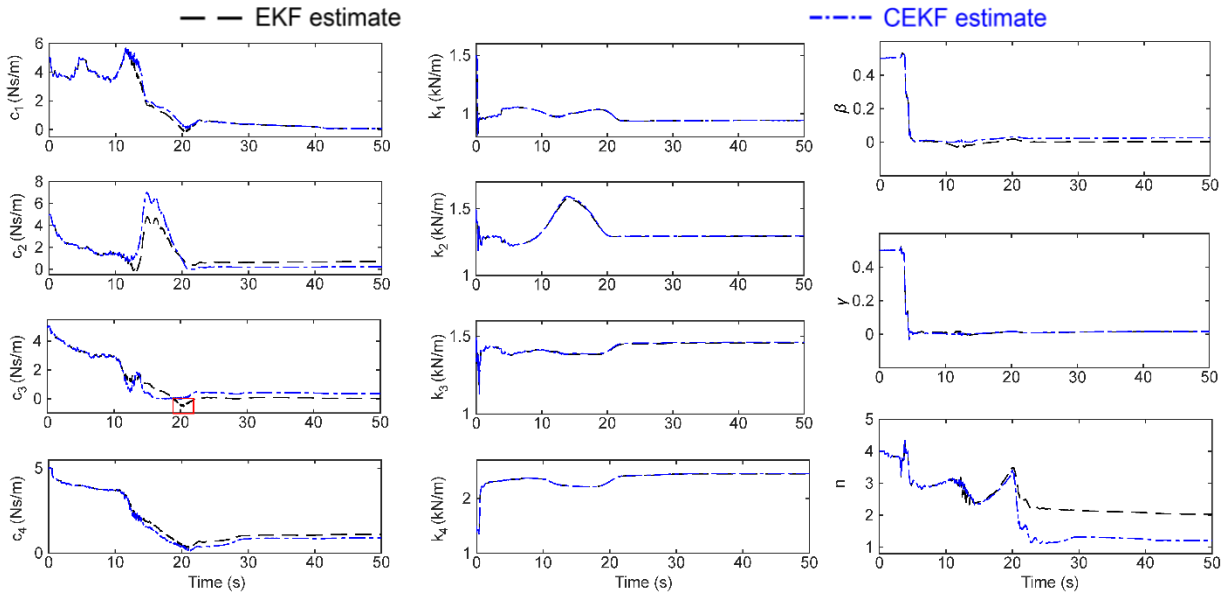

Figure 4-5 Updating results of EKF and CEKF on the four-story shear structure using experimental data

For example, EKF estimate of c_3 becomes negative at about 20 s as shown in the figure. The estimates of hysteretic parameters (β, γ, and n) change slowly at the beginning of the identification process, and change rapidly at about 5 s. After the rapid updating, the estimates of β and γ remain steady, while the estimate of n starts to fluctuate. The EKF and CEKF estimates of n diverge at about 20 s, and finally reach at different values.

Table 4-3 summarizes the estimated results provided by EKF and CEKF for the four-story shear structure using experimental data. Both EKF and CEKF results show that lower stories demonstrate much less inter-story stiffness due to significant *P*-Δ effect of the lab structure. The stiffness values estimated by EKF and CEKF are similar to those obtained from previous frequency domain model updating approaches (assuming linear structure) shown in Section 4.2. It should be noted that the hysteretic parameters estimated by EKF

Table 4-3 Estimation results using EKF and CEKF on the four-story shear structure

Parameters	EKF	CEKF
c_1 (Ns/m)	0.0594	0.0635
c_2 (Ns/m)	0.7010	0.2309
c_3 (Ns/m)	0.0219	0.3562
c_4 (Ns/m)	1.1048	0.8935
k_1 (kN/m)	0.9418	0.9418
k_2 (kN/m)	1.2932	1.2958
k_3 (kN/m)	1.4560	1.4612
k_4 (kN/m)	2.4484	2.4520
β	0.0032	0.0257
γ	0.0152	0.0163
n	2.0319	1.2079

are not reasonable, as β is smaller than γ. On the other hand, CEKF ensures the hysteretic parameters remain within realistic bounds.

4.3.2 UKF and CUKF Model Updating

The parameter identification problem of the laboratory 4-story frame is also solved by UKF and CUKF described in Chapter 3. To be consistent with EKF and CEKF, the same initial values and constraints are adopted. Figure 4-6 plots the time histories of the *a posteriori* parameter estimates of the four-story shear structure using UKF and CUKF on experimental data. The UKF and CUKF estimates show similar trends as the EKF and CEKF estimates. The estimates of damping coefficients and stiffness parameters start updating from the beginning of vibration, change significantly during time span from about 10 s to 20 s, and gradually converge to constant values. The figure shows that some UKF estimates of damping coefficients, especially c_3, reach negative values during the

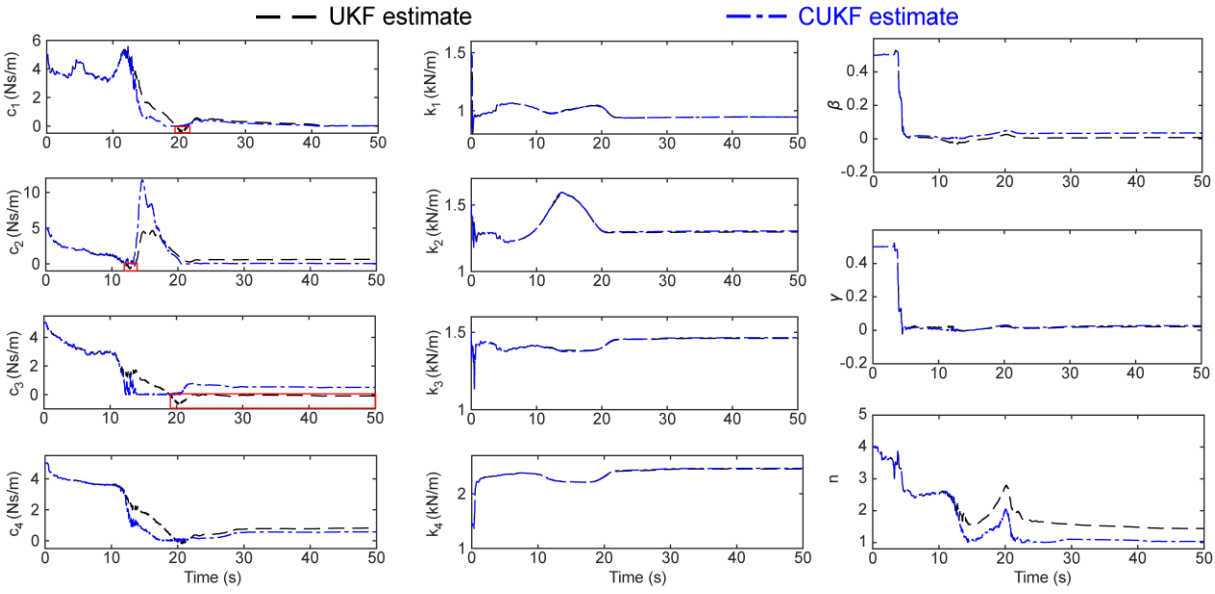

Figure 4-6 Updating results of UKF and CUKF on the four-story shear structure using experimental data

identification process. On the other hand, the CUKF estimates always stay within feasible domain by incorporating constraints in parameter identification. Similar to EKF and CEKF updating results, the UKF and CUKF estimates of hysteretic parameters (β, γ, and n) start to rapidly update at about 5 s. The estimates of β and γ quickly reach at constant values. The UKF and CUKF estimates of n also diverge at about 20 s and converge to different values in the end.

Table 4-4 summarizes the estimated results provided by UKF and CUKF for the four-story shear structure using experimental data. Again, both UKF and CUKF results show that lower stories demonstrate much less inter-story stiffness due to significant *P*-Δ effect of the shear structure. The stiffness values estimated by UKF and CUKF are similar to the results obtained from previous frequency domain model updating approaches (assuming

Table 4-4 Estimation results using UKF and CUKF on the four-story shear structure

Parameters	UKF	CUKF
c_1 (Ns/m)	0.0079	0.0169
c_2 (Ns/m)	0.6285	0.0509
c_3 (Ns/m)	−0.0947	0.5020
c_4 (Ns/m)	0.8199	0.5762
k_1 (kN/m)	0.9457	0.9469
k_2 (kN/m)	1.2969	1.3046
k_3 (kN/m)	1.4610	1.4649
k_4 (kN/m)	2.4544	2.4665
β	0.0075	0.0352
γ	0.0215	0.0278
n	1.4411	1.0339

linear structure) shown in Table 4-1. The results in Table 4-4 are also close to those obtained from EKF and CEKF shown in Table 4-3. It should be noted that in Table 4-4, UKF estimates of c_3, β, and γ fail to satisfy the constraints from physical laws, as c_3 is negative and β is smaller than γ.

4.4 Comparison Between Updating Results of Different Approaches

To investigate the performance of parameter identification algorithms, structural responses are simulated using the updated parameter values obtained from different model updating approaches in Section 4.2 and Section 4.3. In the simulation, the process noise covariance Σ_w and the measurement noise covariance $\mathbf{\Sigma_v}$ are set as 0.

The linear model updating using SOS optimization method in Section 4.2 only provides updated values for stiffness parameters. To simulate reasonable structural responses, a Rayleigh damping matrix is constructed using the first two damping ratios identified from experimental data (Figure 4-3). Structural responses, including displacement $\mathbf{q}$ and acceleration $\ddot{\mathbf{q}}$, can be calculated according to the Eq. (4-9) shown below.

$$\mathbf{M}\ddot{\mathbf{q}} + \mathbf{C}\dot{\mathbf{q}} + \mathbf{K}\mathbf{q} = -\mathbf{M}\boldsymbol{\iota}\ddot{q}_g \tag{4-9}$$

Here $\boldsymbol{\iota} = \{\mathbf{1}\} \in \mathbb{R}^4$ is the influence vector. Figure 4-7 plots the simulated displacement responses of the shear structure using initial stiffness parameters and those updated through SOS optimization method. Displacement responses of entire time span from 0 s to 50 s are plotted in Figure 4-7 (a). The close-up plots of 5 s to 8 s are shown in

Figure 4-7 (b), and the close-up plots of 30 s to 33 s are shown in Figure 4-7 (c). The comparison demonstrates that the updated stiffness parameters from SOS optimization method can predict displacement responses close to the measurement data. On the other hand, the linear model using the initial stiffness parameters cannot provide accurate displacement responses.

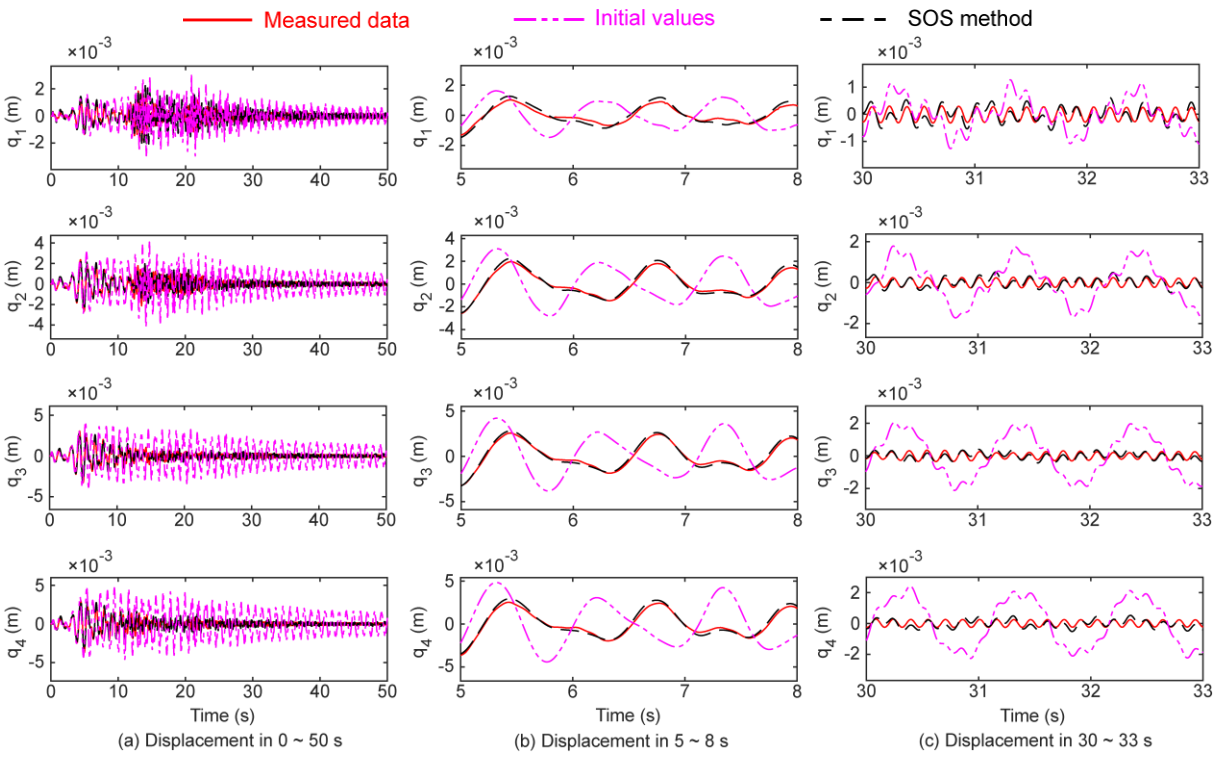

Figure 4-7 Simulated displacement using initial stiffness parameters and parameters updated by SOS optimization

Figure 4-8 plots the simulated acceleration responses of the shear structure using initial stiffness parameters and those updated through SOS optimization method. Acceleration responses of entire time span from 0 s to 50 s are plotted in Figure 4-8 (a). The close-up plots of 5 s to 8 s are shown in Figure 4-8 (b), and the close-up plots of 30 s to 33 s are shown in Figure 4-8 (c). The simulation results show that the updated stiffness

parameters from SOS optimization method can predict acceleration responses close to the measurement data. The acceleration responses simulated using the initial stiffness parameters are quite different from the measurement data at beginning but become closer to the measurement data as time increases.

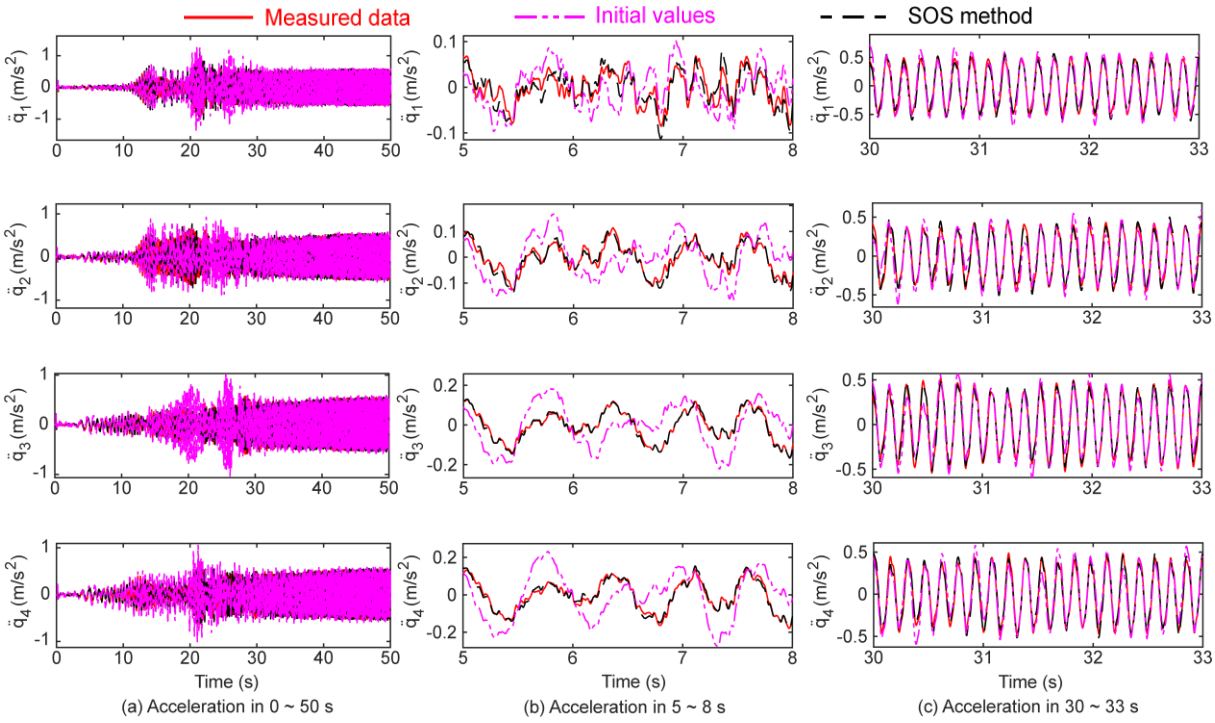

Figure 4-8 Simulated acceleration using initial stiffness parameters and parameters updated by SOS optimization

Next, updated model parameters from EKF and CEKF are used to simulate the dynamical responses of the shear structure. Displacement $\mathbf{q}$ and acceleration $\ddot{\mathbf{q}}$ can be calculated according to the nonlinear system equations Eq. (4-3) and Eq. (4-4). Figure 4-9 plots the simulated displacement responses of the shear structure using initial model parameters and those updated through EKF and CEKF algorithms. Displacement responses of entire time span from 0 s to 50 s are plotted in Figure 4-9 (a). The close-up plots of 5 s to 8 s are shown in Figure 4-9 (b). The simulation results show that parameters updated by

EKF and CEKF provide similar displacement responses at the beginning. Comparing to the displacement responses generated from initial model parameters, the EKF and CEKF responses are much closer to the measurement data. The close-up plots of 30 s to 33 s are shown in Figure 4-9 (c). It can be seen from the figure that CEKF updated parameters performs consistently well over time. On the other hand, the EKF updated parameters cannot provide accurate displacement responses as time increases. Different from the results of linear model (Figure 4-7), the nonlinear model using initial parameters can generate relatively accurate displacement responses in the later part of simulation.

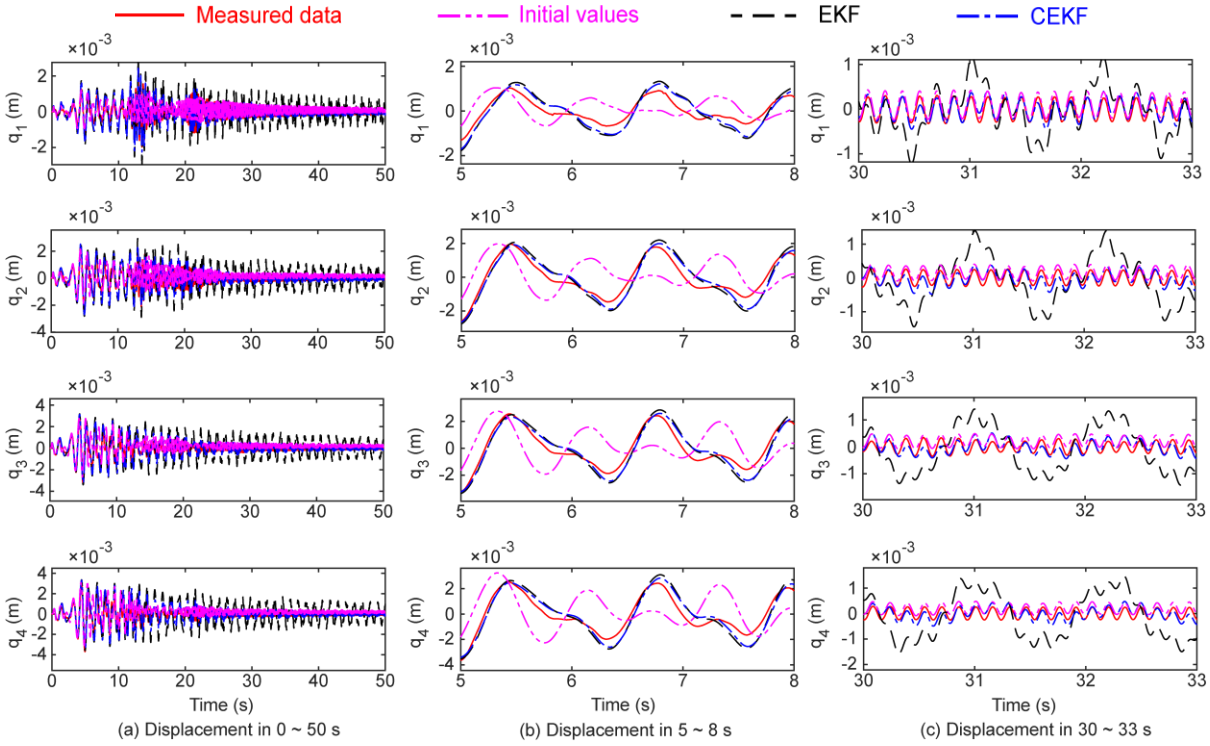

Figure 4-9 Simulated displacement using initial model parameters and parameters updated by EKF and CEKF

Figure 4-10 plots the simulated acceleration responses of the shear structure using initial model parameters and the updated parameter values from EKF and CEKF algorithms. Acceleration responses of entire time span from 0 s to 50 s are plotted in Figure

4-10 (a). The close-up plots of 5 s to 8 s are shown in Figure 4-10 (b).At the beginning, both EKF and CEKF updated parameters provide acceleration responses close to measurement data, while initial model parameters cannot generate accurate acceleration response. The close-up plots of 30 s to 33 s are shown in Figure 4-10 (c). Similar to the results of linear model shown in Figure 4-8, acceleration responses provided by all the model parameters become closer to the measurement data as time increases.

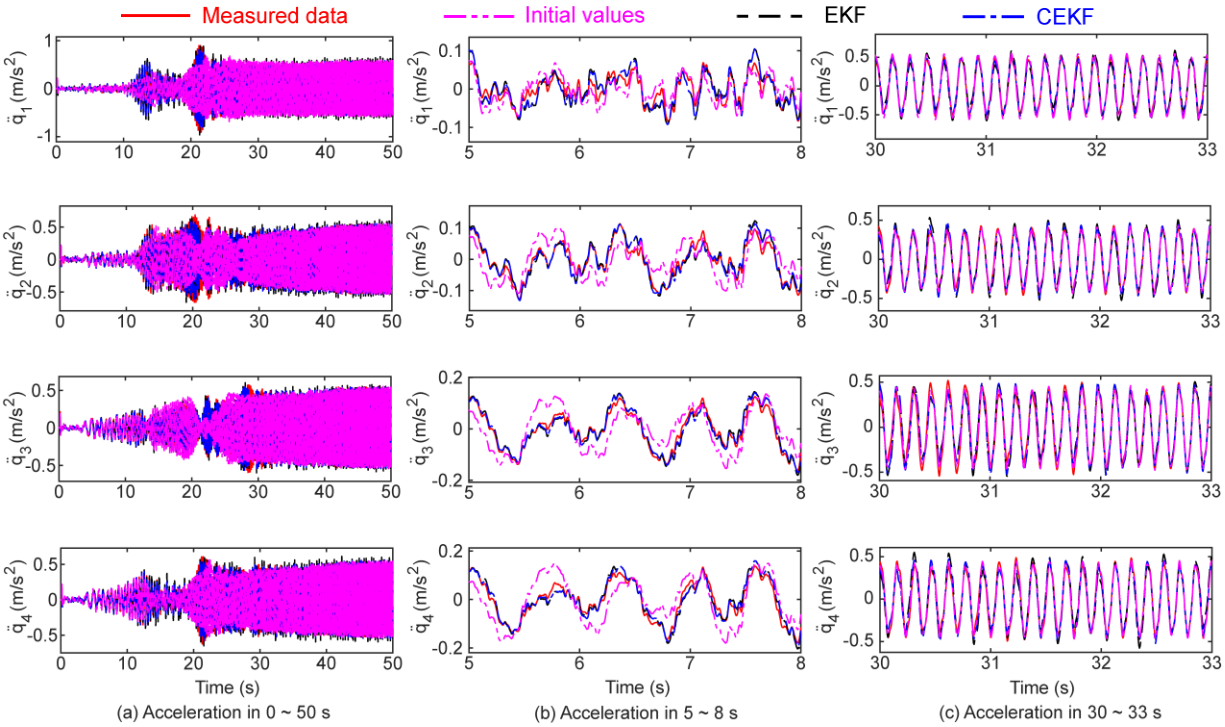

Figure 4-10 Simulated acceleration using initial model parameters and parameters updated by EKF and CEKF

The dynamical responses of the shear structure are simulated again through the nonlinear system equations Eq. (4-3) and Eq. (4-4) using updated model parameters from UKF and CUKF. Figure 4-11 plots the simulated displacement responses of the shear structure using initial model parameters and those updated through UKF and CUKF algorithms. Displacement responses of entire time span from 0 s to 50 s are shown in Figure

4-11 (a). The close-up plots of 5 s to 8 s are plotted in Figure 4-11 (b), and the close-up plots of 30 s to 33 s are shown in Figure 4-11 (c). The displacement responses from initial parameters are the same as those shown in Figure 4-9, and are plotted here for comparison with the updated parameters. The simulation results show that parameters updated by UKF and CUKF provide similar displacement responses at the beginning. Similar to CEKF, the updated parameters from CUKF performs consistently well over time. On the other hand, the UKF updated parameters cannot provide accurate displacement responses as time increases.

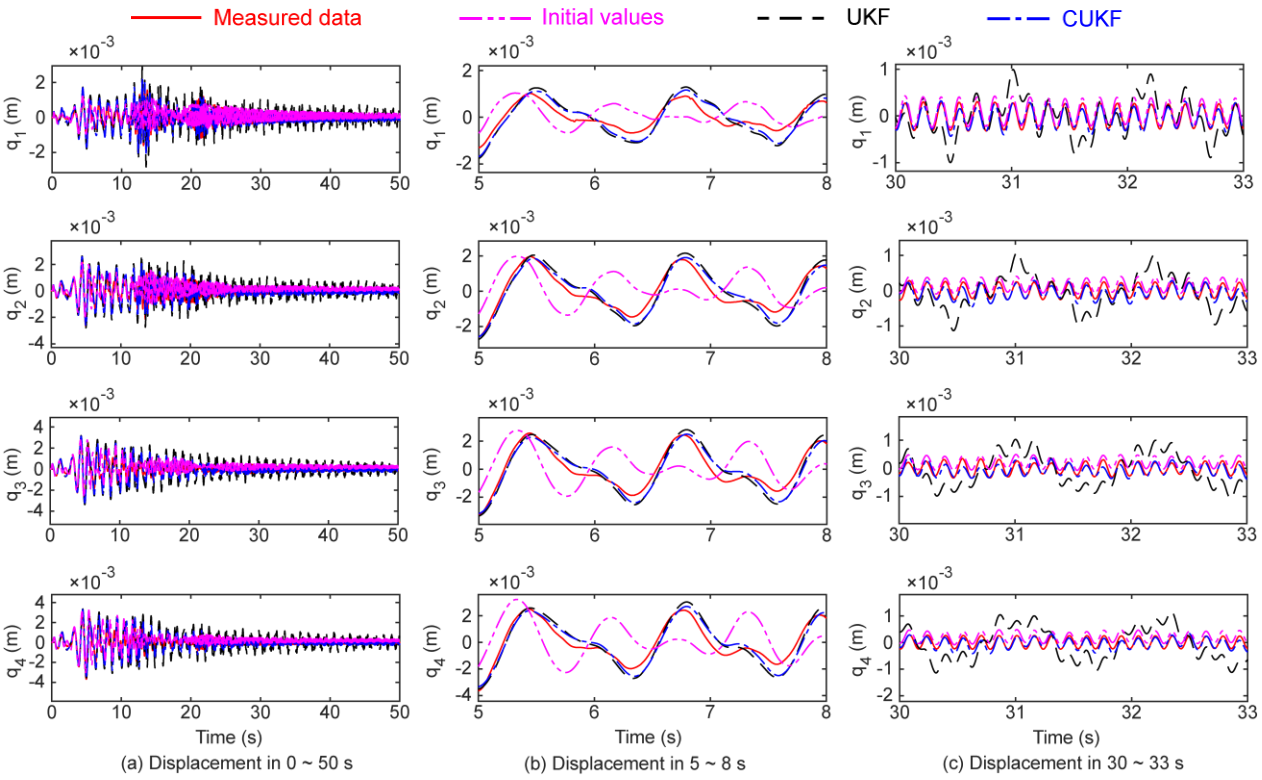

Figure 4-11 Simulated displacement using initial model parameters and parameters updated by UKF and CUKF

Figure 4-12 plots the simulated acceleration responses of the shear structure using initial model parameters and those updated through UKF and CUKF algorithms.

Acceleration responses of entire time span from 0 s to 50 s are plotted in Figure 4-12 (a). The close-up plots of 5 s to 8 s are shown in Figure 4-12 (b), and the close-up plots of 30 s to 33 s are shown in Figure 4-12 (c). Again, the acceleration responses of initial model parameters are plotted for comparison. Similar to the EKF and CEKF, parameters updated by both UKF and CUKF can provide acceleration responses close to measurement data throughout the entire time span.

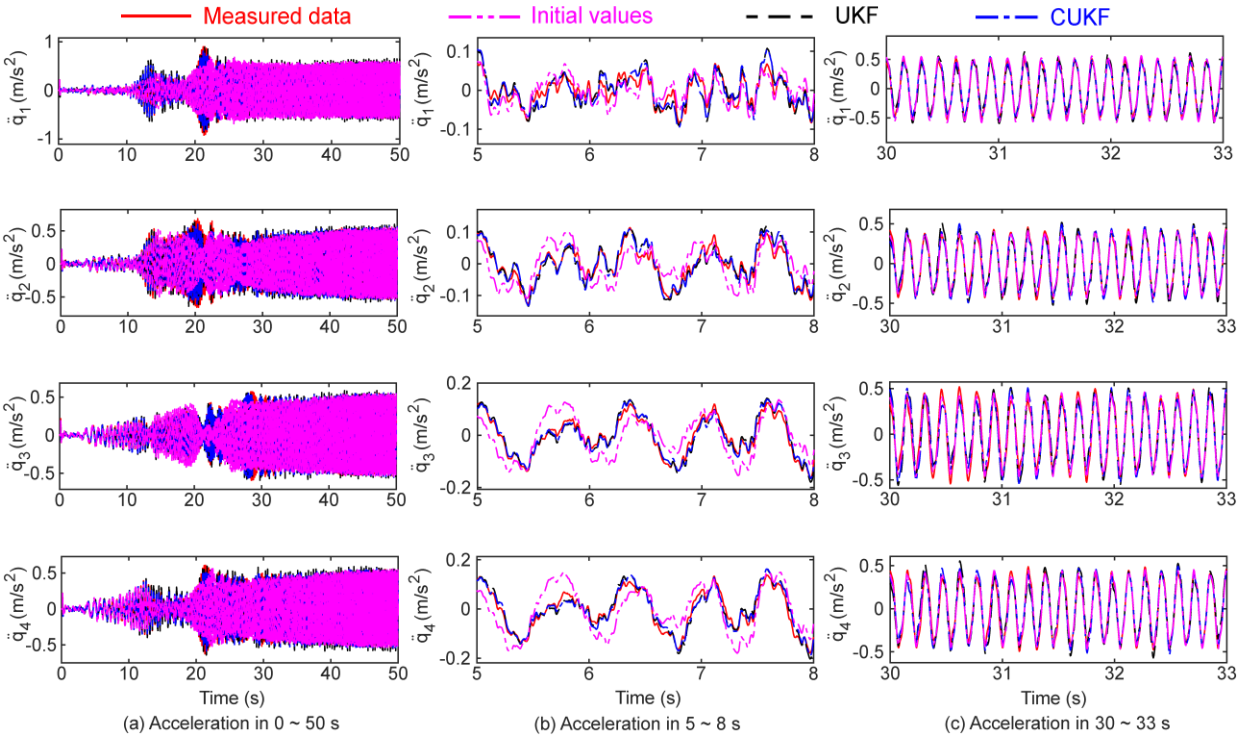

Figure 4-12 Simulated acceleration using initial model parameters and parameters updated by UKF and CUKF

To quantify the performance of model updating methods, Table 4-5 summarizes the root mean square (RMS) errors of the simulated responses for the entire 50 s time span. For each row in the table, the smallest error is circled, and the largest error has highlighted background. The comparison shows that the SOS updated parameters performs well in terms of displacements of the third floor q_3 and the fourth floor q_4, and acceleration of the

third floor $\ddot{q}_3$, while having large estimation errors for all the other acceleration responses, including $\ddot{q}_1$, $\ddot{q}_2$, and $\ddot{q}_4$. The constrained Kalman filters, CEKF and CUKF, are able to reduce the estimation errors of the Kalman filters, EKF and UKF, respectively. Comparing EKF and UKF results, the errors of UKF are generally smaller than those of EKF. As for CEKF and CUKF, the displacement errors of CUKF are smaller than those of CEKF, while CEKF performs better in terms of acceleration responses.

Table 4-5 RMS error comparison of simulated responses

RMS error	SOS	EKF	CEKF	UKF	CUKF
q_1 ($\times 10^{-4}$ m)	4.0610	4.9317	2.3347	4.0796	2.1697
q_2 ($\times 10^{-4}$ m)	2.9715	6.6412	3.1165	5.1741	2.8564
q_3 ($\times 10^{-4}$ m)	1.8507	7.9809	3.6720	6.1322	3.2725
q_4 ($\times 10^{-4}$ m)	3.1309	8.7002	4.0522	6.7637	3.6253
$\ddot{q}_1$ ($\times 10^{-2}$ m/s²)	12.4800	7.4750	3.5921	6.9007	4.3505
$\ddot{q}_2$ ($\times 10^{-2}$ m/s²)	9.2858	5.7188	4.3160	5.4344	5.0976
$\ddot{q}_3$ ($\times 10^{-2}$ m/s²)	3.8336	4.8263	3.8885	4.9726	3.9826
$\ddot{q}_4$ ($\times 10^{-2}$ m/s²)	8.5242	5.8907	3.4961	5.5358	3.8978

4.5 Summary

This chapter investigates model updating performance of the SOS optimization to minimize modal dynamic residuals and constrained Kalman filters. The comparison uses experimentally measured data from a four-story laboratory structure. Based on a 4-DOF linear model, the inter-story stiffness parameters are updated through modal dynamic residual formulation using modal properties extracted from acceleration data. As all the DOFs are measured by sensors, the modal dynamic residual formulation leads to a convex

optimization problem, for which the SOS optimization method and local optimization algorithms find the same optimal solution of the stiffness variables. The modal properties of the updated model are shown to be close to those extracted from experimental data. Next, based on a 4-DOF nonlinear hysteretic model, constrained Kalman filters are used for updating damping coefficients, inter-story stiffness parameters, and Bouc-Wen hysteretic parameters. The updating results demonstrate that incorporating constraints during the estimation process can effectively prevent the parameters from being unrealistic.

Finally, the updated model parameters are used to simulate the dynamical responses of the shear structure. Compared with the experimental measurements, the SOS-updated stiffness parameters can generate relatively accurate displacement responses, while the accelerations of the first, second, and fourth story have large errors. Constrained Kalman filters CEKF and CUKF outperform standard Kalman filters EKF and UKF in terms of both displacement and acceleration responses.

CHAPTER 5. EXPERIMENTAL VALIDTION OF MODEL UPDATING APPROACHES ON A FULL-SCALE REINFORCED CONCRETE FRAME STRUCTURE

This chapter investigates the performance of constrained Kalman filters on model updating through experimental data collected from a full-scale reinforced concrete frame structure. For large and complex structures, it turns out that only updating stiffness parameter may not guarantee accurate simulation of dynamical responses. Thus, the SOS optimization method is not studied using this frame structure. The test structure and experiment setup are first introduced in Section 5.1. The measured acceleration responses at critical locations are used by constrained Kalman filters for identifying model parameters.

A 2D FE model is built for the reinforced concrete frame structure. In Section 5.2, the proposed CEKF and CUKF are investigated using simulated dynamical responses of the FE model. Model parameters, including stiffness variables and damping ratios, are updated based the acceleration data. The effectiveness of the constraints during the parameter identification process is demonstrated.

In Section 5.3, experimentally obtained structural responses are used to update model parameters for the reinforced concrete frame structure. CEKF and CUKF are conducted to update the stiffness variables and damping ratios for the frame structure. Dynamical responses of the structure are simulated using the updated models from CEKF and CUKF. The performance of proposed model updating methods are evaluated by comparing the simulated dynamical responses with the experimental data.

5.1 Frame Structure and Vibration Test

Four reinforced concrete frames were constructed and tested in the Structural Engineering and Materials Laboratory on Georgia Tech campus (Figure 5-1). The four frames are sperate from each other, with a gap between every two neighboring frames. Each frame consists of two stories and two bays with a total height of 24 ft and a total length of 36 ft. When testing of each frame, a 75-kip hydraulic linear inertial shaker was installed on the second elevated slab and utilized to excite the frame with a scaled El Centro record. The moving mass of the shaker can provide in-plane excitation along longitudinal direction. Experimental measurements from the frame #1 are used in this thesis study. When constructing the frame, the concrete was poured in five stages. Figure 5-1(b) illustrates the pour sequence for the frame.

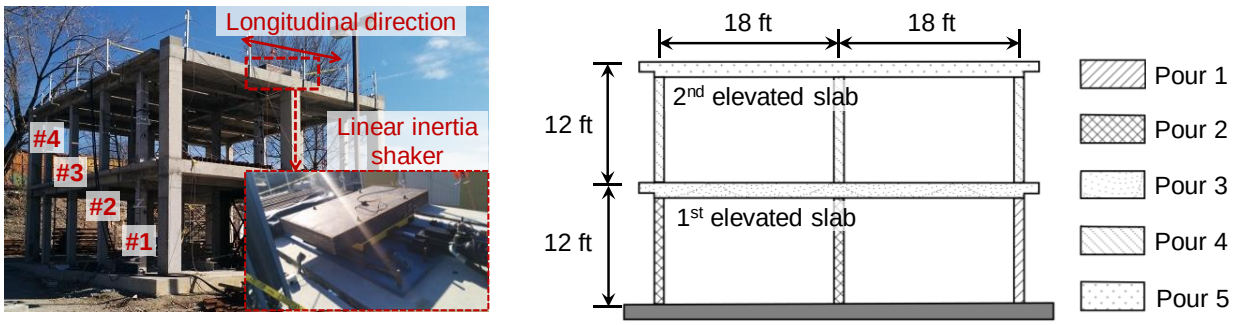

(a) Reinforced concrete frame (b) Sequence of construction

Figure 5-1 Full-scale test frame and pour sequence

A total of 44 in-plane acceleration channels were installed to measure the dynamical responses of the concrete frame. Figure 5-2 illustrates the sensor instrumentation, including 27 channels along longitudinal direction (annotated by blue arrows) and 17 channels along vertical direction (annotated by red arrows). These sensors were installed at mid-length and quarter-length of each beam or column member. With these critical locations measured,

the modal properties of interest can be extracted from the measurement. The sampling frequency was set as 200 Hz.

Figure 5-3 plots two sets of example acceleration data collected by accelerometers

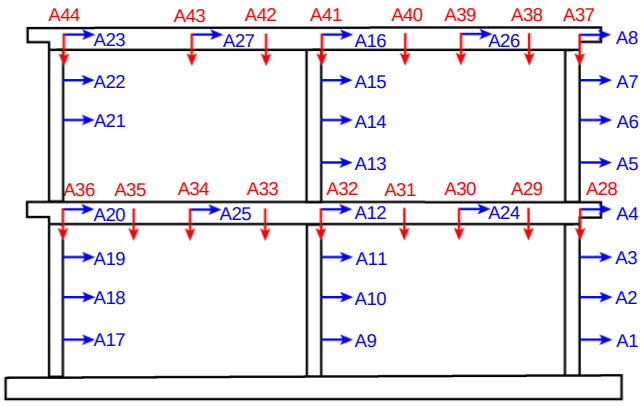

Figure 5-2 Sensor instrumentation

A16 and A18, together with the corresponding frequency spectra. The response spectra indicate that the motion of the structure due to shaker excitation is significant in frequency range from 0 ~ 10 Hz, while higher frequency components also exist.

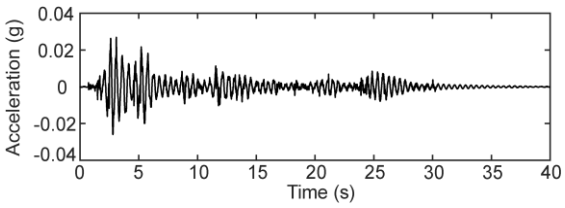

(a) Acceleration of A16

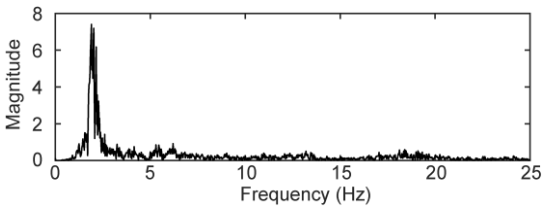

(b) Frequency spectrum of A16

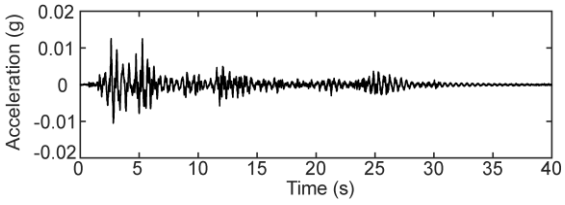

(c) Acceleration of A18

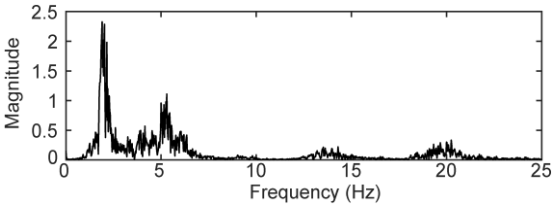

(d) Frequency spectrum of A18

Figure 5-3 Example of acceleration responses and frequency spectra

5.2 Finite Element Model and Model Updating with Simulated Measurements

A 2D FE model for the reinforced concrete frame is built using Euler-Bernoulli beam elements as shown in Figure 5-4. The model consists of 23 nodes, 24 elements, and 36 DOFs in total. Axial deformations of beam elements are neglected in this model. The three bases are modelled as fixed end. Composite sections are adopted to consider the contribution from both concrete and rebars. Table 5-1 summarizes the nominal values of Young's moduli of the concrete and steel rebars for the initial model.

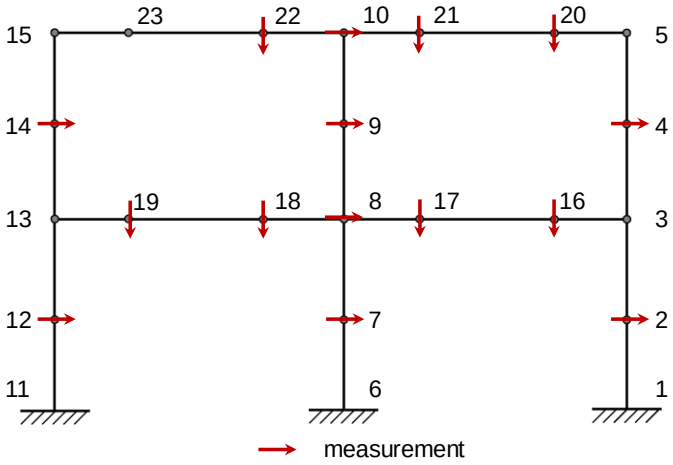

Figure 5-4 FE model for the reinforced concrete frame

Table 5-1 Nominal values of Young's moduli of concrete and steel (Unit: kips/in^2)

Material	Young's moduli
Concrete	3,800
Steel	28,000

Using the FE model, the proposed model updating methods are first studied with simulated data. The constrained Kalman filters, CEKF and CUKF, are applied to identify

the stiffness parameters and damping ratios of the structure. Model updating with experimental data will be presented in upcoming Section 5.3.

Five stiffness variables $\boldsymbol{\theta} \in \mathbb{R}^5$ corresponding to the five pours (Figure 5-1(b)) are selected for updating. Similar to the model updating problems in Chapter 2, the stiffness variables $\boldsymbol{\theta}$ represent the relative change from the nominal values in Table 5-1. In this simulation study, the true values of stiffness variables are set as $\boldsymbol{\theta}^* = (-0.25, 0.1, -0.15, 0.15, -0.2)^{\mathrm{T}}$. Besides five stiffness variables $\boldsymbol{\theta} \in \mathbb{R}^5$, two damping ratios $\boldsymbol{\zeta} \in \mathbb{R}^2$ are also updated for constructing a Rayleigh damping matrix. In this simulation example, the true values of damping ratios are set as $\boldsymbol{\zeta}^* = (0.05, 0.05)^{\mathrm{T}}$. Acceleration responses simulated from the "as-built" structure are utilized as "experimental" data for model updating. The 15 acceleration channels are used, as illustrated in Figure 5-4. To improve the computational efficiency, Guyan model reduction technique is applied to condense the FE model to the 15 measured DOFs. Based on the condensed model, the dynamical responses are calculated through Newmark-beta method.

Constrained Kalman filters, CEKF and CUKF, introduced in Chapter 3 are conducted to identify the model parameters together with the system states. The initial estimates are set as $\theta_{i,0|-1} = 0$ and $\zeta_{i,0|-1} = 0.02$. Inequality constraints applied on the parameters are listed as follows:

$$-1 \leq \theta_i \leq 1, \qquad 0.001 \leq \zeta_i \leq 0.2 \tag{5-1}$$

The time histories of the *a posteriori* estimates of the stiffness variables and damping ratios of the reinforced concrete frame structure obtained from CEKF and CUKF are

plotted in Figure 5-5. The identified results show that both CEKF and CUKF can update the stiffness variables and damping ratios recursively from their initial values to the corresponding true values. It can be seen from the close-up plot Figure 5-5(c) that both CEKF can CUKF can effectively restrain the damping ratio estimates within the feasible domain.

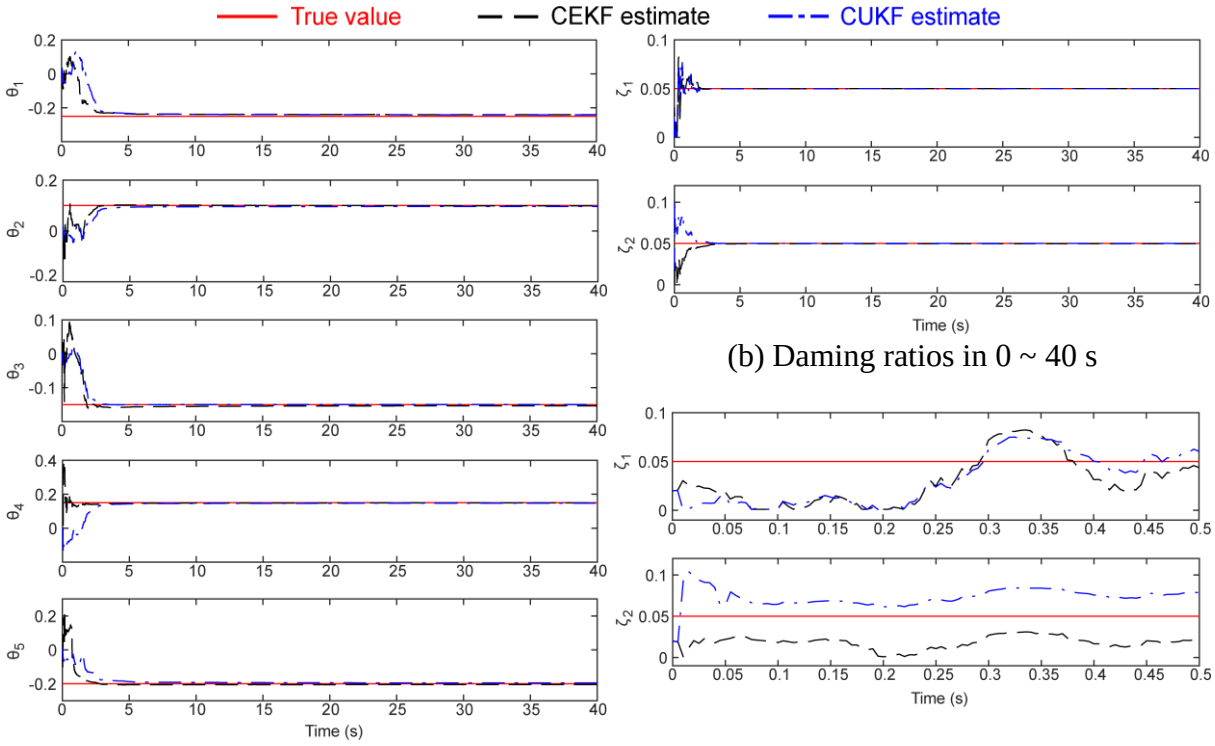

(a) Stiffness variables in 0 ~ 40 s

(b) Daming ratios in 0 ~ 40 s

(c) Daming ratios in 0 ~ 0.5 s

Figure 5-5 Identified stiffness variables and damping ratios from CEKF and CUKF using simulated data

Table 5-2 summaries the final estimated values of model parameters using CEKF and CUKF algorithms. The comparison shows that both the CEKF and the CUKF are capable of identifying the unknown model parameters of this reinforced concrete frame

structure with acceptable accuracy. The performance of the CEKF is similar to the performance of the CUKF. All estimation errors are within $\pm 4\%$.

Table 5-2 Comparison of estimation results on the reinforced concrete frame using CEKF and CUKF with simulated data

Parameters	Actual values	CEKF		CUKF	
		Values	Errors (%)	Values	Errors (%)
θ_1	-0.25	-0.2403	-3.8626	-0.2415	-3.4198
θ_2	0.10	0.0990	-1.0419	0.0962	-3.8425
θ_3	-0.15	-0.1533	2.2247	-0.1497	-0.2085
θ_4	0.15	0.1493	-0.4343	0.1476	-1.6149
θ_5	-0.20	-0.2047	2.3491	-0.1956	-2.1820
ζ_1	0.05	0.0500	-0.0623	0.0499	-0.2161
ζ_2	0.05	0.0497	-0.6969	0.0499	-0.1048

5.3 Model Updating with Experimental Measurements

In this section, the proposed CEKF and CUKF are applied to estimate model parameters of the reinforced concrete frame structure using experimental measurements described in Section 5.1.

The same five stiffness variables $\boldsymbol{\theta} \in \mathbb{R}^5$ and two damping ratios $\boldsymbol{\zeta} \in \mathbb{R}^2$ for the Rayleigh damping matrix are updated again using experimental measurements. The initial estimates are set as $\theta_{i,0|-1} = 0$ and $\zeta_{i,0|-1} = 0.02$. Inequality constraints of the model parameters are listed as follows:

$$-0.3 \leq \theta_i \leq 0.3, \qquad 0.001 \leq \zeta_i \leq 0.2 \tag{5-2}$$

Figure 5-6 plots the time histories of the *a posteriori* parameter estimates of the reinforced concrete frame structure using CEKF and CUKF on experimental data. The stiffness variables and damping ratios start updating from the beginning of vibration. During the beginning 2 s, the parameter estimates change significantly and some of them reach the bound. After that, the parameter estimates gradually converge to constant values. It is observed that the updating results of θ_1 and ζ_1 using CEKF and CUKF are close to each other, while the estimates of other parameters reach at different values.

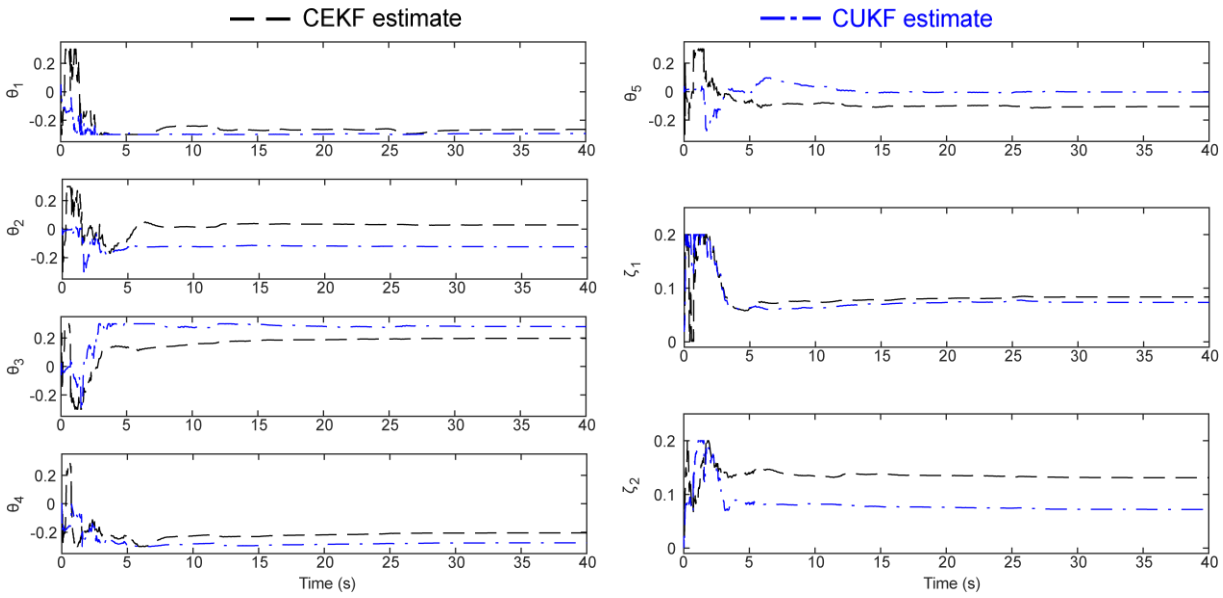

Figure 5-6 Identified stiffness variables and damping ratios from CEKF and CUKF using experimental data

Table 5-3 summarizes the identification results provided by CEKF and CUKF for the reinforced concrete frame structure using experimental data. Both CEKF and CUKF results show that the stiffness values of members constructed by the 1st, 4th and 5th concrete pours decrease from the nominal value, while the stiffness value of members constructed by the 3rd concrete pour increases. The stiffness value of members constructed by the 2nd concrete pour changes slightly from its nominal value. In terms of damping ratios, the

values updated by CUKF are reasonable for reinforced concrete structures, whose damping ratios typically range from 0.05 to 0.10 [83]. On the other hand, CEKF provides slightly higher values of damping ratios, especially for ζ_2.

Table 5-3 Estimation results using CEKF and CUKF of the reinforced concrete frame structure using experimental data

Parameters	CEKF	CUKF
θ_1	-0.2641	-0.2931
θ_2	0.0293	-0.1236
θ_3	0.1980	0.2803
θ_4	-0.2047	-0.2746
θ_5	-0.1052	-0.0021
ζ_1	0.0836	0.0736
ζ_2	0.1311	0.0720

Based on the parameter identification results from CEKF and CUKF, updated FE models are built. The dynamical responses of the reinforced concrete frame structure are simulated using the same excitation. Figure 5-7 plots the simulated acceleration responses of the frame structure at location A16 and A18 using initial model parameters and the updated parameter values from CEKF and CUKF algorithms. Acceleration responses of entire time span from 0 s to 40 s are plotted in Figure 5-7(a). The close-up plots of 15.5 s to 17.5 s are shown in Figure 5-7(b). The comparison shows that both CEKF and CUKF updated parameters provide acceleration responses close to measurement data, while initial model parameters cannot generate accurate acceleration response.

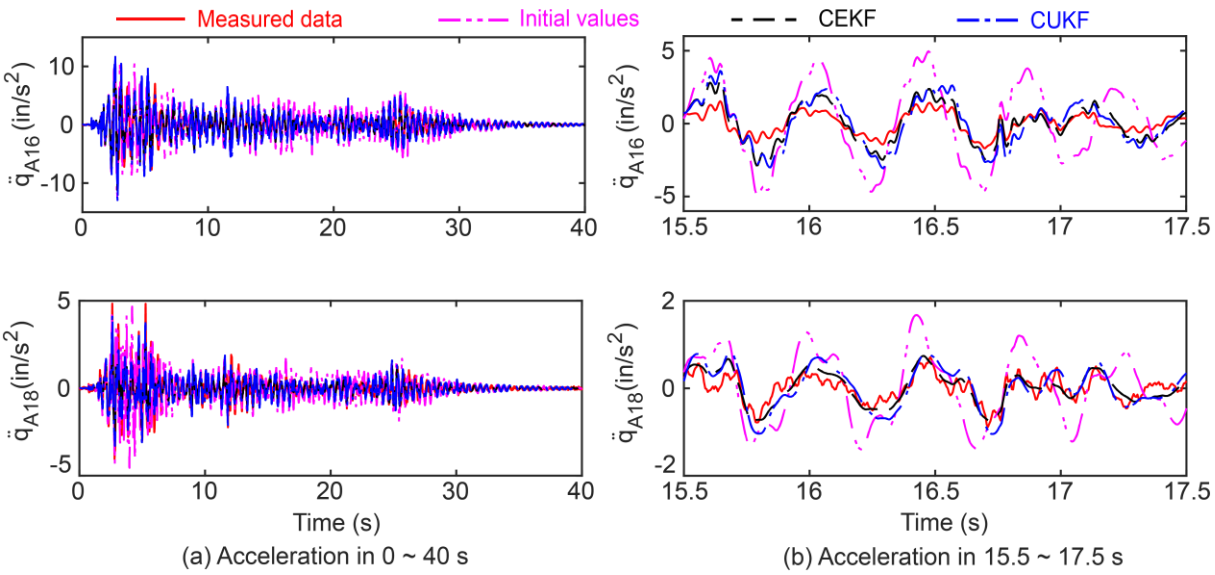

Figure 5-7 Simulated acceleration using initial model parameters and parameters updated by CEKF and CUKF

To quantify the performance of CEKF and CUKF, Table 5-4 summarizes the root mean square (RMS) errors of the simulated acceleration responses for the entire 40 s time span. Compared with the initial FE model, both the CEKF and CUKF updated FE models provide simulated responses with less RMS errors.

Table 5-4 RMS error comparison of simulated acceleration responses of updated models from CEKF and CUKF (Unit: in/s^2)

Channel	Initial	CEKF	CUKF	Channel	Initial	UKF	CUKF
A2	0.7727	0.3505	0.3413	A29	0.1734	0.1284	0.1384
A6	1.5568	0.7493	0.7507	A31	0.0455	0.0347	0.0322
A10	0.8014	0.3528	0.3322	A33	0.0536	0.0285	0.0316
A12	1.3393	0.5241	0.5684	A35	0.1548	0.1153	0.1198
A14	1.5241	0.7099	0.7072	A38	0.2009	0.1287	0.1404
A16	1.9091	0.8508	0.8940	A40	0.1061	0.0598	0.0630
A18	0.7764	0.3531	0.3363	A42	0.0846	0.0464	0.0453
A21	1.5536	0.7462	0.7514				

5.4 Summary

Based on a 2D linear FE model, this chapter presents model updating for a full-scale reinforced concrete frame structure. The proposed CEKF and CUKF are validated using simulated acceleration responses. Reasonable bound constraints are applied on model parameters. The simulation results show that both CEKF and CUKF can effectively prevent parameter estimates from violating the constraints during the identification process. The final identification results show that both CEKF and CUKF can reliably update the model parameters to the corresponding true values.

The proposed model updating methods are repeated using experimental measurements. Constrained Kalman filters are conducted to update the stiffness parameters and damping ratios using measured acceleration data from the dynamical test. Incorporating constraints during the estimation process can effectively prevent the parameters from being unrealistic. The updating results of CEKF and CUKF show similar trend of stiffness change, while CEKF provides higher damping ratios. The updated model parameters are used to simulate the dynamical behaviors of the reinforced concrete frame structure. The simulation results show that acceleration responses of two updated models are much closer to the measured responses than the initial model.

CHAPTER 6. SUMMARY AND FUTURE WORK

This research studies techniques to improve the performance of finite element (FE) model updating for civil structures. A global optimization algorithm, the sum-of-squares (SOS) method, is proposed to solve the modal dynamic residual formulation for frequency-domain model updating. Methods improving computational efficiency of the SOS method is discussed for practical application. In terms of time-domain model updating, the constrained extended Kalman filter (CEKF) and the constrained unscented Kalman filter (CUKF) are proposed to update both linear and nonlinear structures. Extensive simulations and experiments are conducted to validate the proposed FE model updating methods. This chapter first summarizes main conclusions of the dissertation, and then discusses potential research topics in future.

6.1 Summary of the Dissertation

The main conclusions and major findings of this dissertation are summarized as follows:

1. In this dissertation, modal dynamic residual formulation is adopted to update stiffness parameters using experimental modal properties of a structure. In general, the formulated optimization problem is nonconvex, for which traditional optimization algorithms, e.g. the gradient based algorithm, can be easily trapped at a local minimum and fail to find the global solution. The SOS optimization method can recast such a nonconvex polynomial problem into a convex SDP problem. As the SDP problem is convex, the solution is guaranteed to be globally optimal. Numerical studies on a four-story shear

structure shows the nonconvexity of the model updating problem and validates that the SOS optimization method can reliably find the global optimum.

2. While the optimization method is promising in solving nonconvex polynomial problems, the computational complexity of the formulated SDP problem grows rapidly when the polynomial optimization problem has a large number of variables and/or high degree. As the formulated objective function consists of several polynomials only involving a small number of variables, sparse SOS optimization method is applied to reduce the computational effort. To further improve the computational efficiency, the facial reduction technique is applied to yield an equivalent SDP problem with smaller size. Numerical studies on a plane truss structure demonstrate that the sparse SOS optimization method and facial reduction technique can reach the global optimum of the model updating problem while significantly reducing computation effort compared with the standard SOS optimization method.

3. Model parameters can be recursively updated from the measured dynamical responses of structures using nonlinear Kalman filters, such as EKF and UKF. In order to achieve reasonable parameter estimates, constraints are incorporated during the identification process. Details of CEKF and CUKF are provided in the Chapter 3. Numerical studies on a four-story shear structure show that both EKF and UKF can accurately identify the stiffness parameters and damping coefficients for such a linear structure. To further investigate the model updating performance of Kalman filters, a differentiable Bouc-Wen model is proposed for implementation of EKF and CEKF. Simulation on an SDOF Bouc-Wen hysteretic system demonstrates that EKF can easily result in unreliable estimates for model parameters, especially for hysteretic parameters,

due to large linearization error of the highly nonlinear system. Compared with EKF, CEKF can effectively prevent the parameter estimates from violating the constraints, and finally achieve accurate identification results. In addition, both UKF and CUKF can provide reasonable updating results and CUKF performs slightly better in terms of accuracy.

4. Experimental measurements of a four-story shear structure are used to investigate the performance of the proposed model updating methods, i.e. the SOS optimization minimizing modal dynamic residuals and constrained Kalman filters (CEKF and CUKF). A 4-DOF linear model is built for updating inter-story stiffness parameters through modal dynamic residual formulation. With all DOFs measured by sensors, the modal dynamic residual formulation leads to a convex optimization problem. SOS optimization method and local optimization algorithms are applied to solve the model updating problem and are shown to reach the same optimal solution. Modal properties of the updated model are closer to the experimental modal properties than the initial model. A nonlinear hysteretic model is built for updating model parameters through constrained Kalman filters. The updating results show that CEKF and CUKF can prevent model parameters from violating constraints and provide reasonable estimates. Dynamical responses of the CEKF and CUKF updated models are closer to the experimental data than the EKF and UKF updated models. In addition, nonlinear model updating using the CEKF and CUKF results in more reliable acceleration response than linear model updating using the SOS optimization method.

5. The proposed CEKF and CUKF are investigated using numerical simulation and experimental measurements on a full-scale reinforced concrete structure. A 2D linear FE model is built for model updating. The effectiveness of CEKF and CUKF is validated in

simulation first. Using simulated acceleration responses, stiffness parameters and damping ratios can be recursively identified by CEKF and CUKF. Parameter estimates always follow the constraints during the estimation process. Experimental measurements are then used to update model parameters. CEKF and CUKF are conducted again to identify stiffness parameters and damping ratios of the structure. CEKF and CUKF provide similar stiffness parameters, while damping ratios identified by CEKF are higher than those by CUKF. Simulation results demonstrate that acceleration responses of CEKF and CUKF updated models are much closer to the measured responses than the initial model. The SOS optimization method is not studied using the full-scale reinforced concrete frame structure as only updating stiffness parameters may not guarantee trustworthy simulation of dynamical responses for large and complex structures.

6.2 Future Work

Based on research work presented in the dissertation, several future studies are recommended as follows:

1. The proposed SOS optimization minimizing modal dynamic residuals encounters challenges when updating FE models for large structures using experimental data contaminated with noises. These measurement noises inevitably bring errors in identified modal properties and thus adversely affect the model updating results. Systematic studies need to be conducted to investigate the influence of noises on the model updating results using modal dynamic residual formulation. Another promising research direction can be developing frequency-domain model updating approaches which are insensitive to measurement noises.

2. For constrained Kalman filters, the noise covariances are of significant importance for reliable model updating and needs to be determined properly based on prior statistical knowledge of the data. Under certain circumstance, accurate statistical information of the measurement data is difficult to obtain. Therefore, the effect of noise covariances needs to be analyzed and investigated for accurate parameter identification.

3. The proposed SOS optimization method has demonstrated promising performance on updating small and medium sized FE models, i.e. the 4-DOF model for shear structure and the 2D plane truss model. Studies need to be conducted on applying the presented model updating methods on larger-scale structural models with hundreds or thousands of DOFs. The SOS optimization method is based on convex optimization which is still a very active research area. Developing more efficient solvers for SDP problems would improve the computational efficiency of the SOS optimization method. In addition, model order reduction techniques, such as dynamic condensation [84] and system equivalent reduction expression process (SEREP) [85], can be investigated for the SOS optimization method toward larger applications and under realistic constraints on computing resources. Model updating using constrained Kalman filters would also benefit from the model order reduction techniques.

4. Nonlinear FE model updating has found many applications in structural analysis and damage detection. This research demonstrates the application of constrained Kalman filters to update model parameters for a four-story shear structure with Bouc-Wen hysteresis. Different nonlinear patterns, including material nonlinearity and geometry nonlinearity, can be further investigated for model updating of civil structures using

constrained Kalman filters. Additional stability analysis is needed for nonlinear model updating using constrained Kalman filters.

REFERENCES

[1] M. Friswell and J. E. Mottershead, *Finite element model updating in structural dynamics* vol. 38: Springer Science & Business Media, 2013.

[2] A. Teughels and G. De Roeck, "Structural damage identification of the highway bridge Z24 by FE model updating," *Journal of Sound and Vibration,* vol. 278, pp. 589-610, 2004.

[3] S.-E. Fang, R. Perera, and G. De Roeck, "Damage identification of a reinforced concrete frame by finite element model updating using damage parameterization," *Journal of Sound and Vibration,* vol. 313, pp. 544-559, 2008.

[4] B. Weber, P. Paultre, and J. Proulx, "Consistent regularization of nonlinear model updating for damage identification," *Mechanical Systems and Signal Processing,* vol. 23, pp. 1965-1985, 2009.

[5] S. W. Doebling, C. R. Farrar, and M. B. Prime, "A summary review of vibration-based damage identification methods," *Shock and Vibration Digest,* vol. 30, pp. 91-105, 1998.

[6] E. P. Carden and P. Fanning, "Vibration based condition monitoring: a review," *Structural Health Monitoring,* vol. 3, pp. 355-377, 2004.

[7] E. Simoen, G. De Roeck, and G. Lombaert, "Dealing with uncertainty in model updating for damage assessment: A review," *Mechanical Systems and Signal Processing,* vol. 56, pp. 123-149, 2015.

[8] L. Wang and T. H. Chan, "Review of vibration-based damage detection and condition assessment of bridge structures using structural health monitoring," 2009.

[9] M. I. Friswell, "Damage identification using inverse methods," *Philosophical Transactions of the Royal Society A: Mathematical, Physical and Engineering Sciences,* vol. 365, pp. 393-410, 2006.

[10] Q. W. Zhang, C. C. Chang, and T. Y. P. Chang, "Finite element model updating for structures with parametric constraints," *Earthquake Engineering & Structural Dynamics,* vol. 29, pp. 927-944, Jul 2000.

[11] P. Ladevèze, D. Nedjar, and M. Reynier, "Updating of finite element models using vibration tests," *AIAA Journal,* vol. 32, pp. 1485-1491, 1994.

[12] A. Teughels, J. Maeck, and G. De Roeck, "Damage assessment by FE model updating using damage functions," *Computers & Structures,* vol. 80, pp. 1869-1879, Sep 2002.

[13] B. Jaishi and W. X. Ren, "Damage detection by finite element model updating using modal flexibility residual," *Journal of Sound and Vibration,* vol. 290, pp. 369-387, Feb 2006.

[14] J. E. Mottershead, M. Link, and M. I. Friswell, "The sensitivity method in finite element model updating: a tutorial," *Mechanical Systems and Signal Processing,* vol. 25, pp. 2275-2296, 2011.

[15] A. Fregolent, W. D'Ambrogio, P. Salvini, and A. Sestieri, "Regularisation techniques for dynamic model updating using input residual," *Inverse Problems in Engineering,* vol. 2, pp. 171-200, 1996.

[16] H. Natke, "Updating computational models in the frequency domain based on measured data: a survey," *Probabilistic Engineering Mechanics,* vol. 3, pp. 28-35, 1988.

[17] C. Farhat and F. M. Hemez, "Updating finite element dynamic models using an element-by-element sensitivity methodology," *AIAA Journal,* vol. 31, pp. 1702-1711, 1993.

[18] S. Ibrahim, C. Stavrinidis, E. Fissette, and O. Brunner, "A direct two response approach for updating analytical dynamic models of structures with emphasis on uniqueness," 1990.

[19] D. Zhu, X. Dong, and Y. Wang, "Substructure stiffness and mass updating through minimization of modal dynamic residuals," *ASCE Journal of Engineering Mechanics,* vol. 142, p. 04016013, 2016.

[20] M. Imregun, W. Visser, and D. Ewins, "Finite element model updating using frequency response function data: I. Theory and initial investigation," *Mechanical Systems and Signal Processing,* vol. 9, pp. 187-202, 1995.

[21] M. Imregun, K. Sanliturk, and D. Ewins, "Finite element model updating using frequency response function data: II. Case study on a medium-size finite element model," *Mechanical Systems and Signal Processing,* vol. 9, pp. 203-213, 1995.

[22] J. D. Sipple and M. Sanayei, "Finite element model updating using frequency response functions and numerical sensitivities," *Structural Control and Health Monitoring,* vol. 21, pp. 784-802, 2014.

[23] V. Arora, S. Singh, and T. Kundra, "Finite element model updating with damping identification," *Journal of Sound and Vibration,* vol. 324, pp. 1111-1123, 2009.

[24] R. Levin and N. Lieven, "Dynamic finite element model updating using simulated annealing and genetic algorithms," *Mechanical Systems and Signal Processing,* vol. 12, pp. 91-120, 1998.

[25] A. Teughels, G. De Roeck, and J. A. Suykens, "Global optimization by coupled local minimizers and its application to FE model updating," *Computers & Structures,* vol. 81, pp. 2337-2351, 2003.

[26] P. G. Bakir, E. Reynders, and G. De Roeck, "An improved finite element model updating method by the global optimization technique 'Coupled Local Minimizers'," *Computers & Structures,* vol. 86, pp. 1339-1352, 2008.

[27] T. Ma, J. Shi, and D. Steurer, "Polynomial-time tensor decompositions with sum-of-squares," in *2016 IEEE 57th Annual Symposium on Foundations of Computer Science (FOCS),* 2016, pp. 438-446.

[28] J. Nie, "Symmetric tensor nuclear norms," *SIAM Journal on Applied Algebra and Geometry,* vol. 1, pp. 599-625, 2017.

[29] A. A. Ahmadi, G. Hall, A. Makadia, and V. Sindhwani, "Geometry of 3D environments and sum of squares polynomials," in *Proceedings of Robotics: Science and Systems 2017,* Cambridge, MA, 2017.

[30] J. Anderson and A. Papachristodoulou, "Advances in computational Lyapunov analysis using sum-of-squares programming," *Discrete & Continuous Dynamical Systems-Series B,* vol. 20, 2015.

[31] J. B. Lasserre, "Convergent SDP-relaxations in polynomial optimization with sparsity," *SIAM Journal on Optimization,* vol. 17, pp. 822-843, 2006.

[32] H. Waki, S. Kim, M. Kojima, and M. Muramatsu, "Sums of squares and semidefinite program relaxations for polynomial optimization problems with structured sparsity," *SIAM Journal on Optimization,* vol. 17, pp. 218-242, 2006.

[33] L. Vandenberghe and S. Boyd, "Semidefinite programming," *SIAM Review,* vol. 38, pp. 49-95, 1996.

[34] J. N. Yang and S. Lin, "Identification of parametric variations of structures based on least squares estimation and adaptive tracking technique," *Journal of Engineering Mechanics,* vol. 131, pp. 290-298, 2005.

[35] W. Song and S. Dyke, "Real-time dynamic model updating of a hysteretic structural system," *Journal of Structural Engineering,* vol. 140, p. 04013082, 2013.

[36] S. Li, Y. Suzuki, and M. Noori, "Improvement of parameter estimation for non-linear hysteretic systems with slip by a fast Bayesian bootstrap filter," *International Journal of Non-Linear Mechanics,* vol. 39, pp. 1435-1445, 2004.

[37] E. N. Chatzi and A. W. Smyth, "Particle filter scheme with mutation for the estimation of time-invariant parameters in structural health monitoring applications," *Structural Control and Health Monitoring,* vol. 20, pp. 1081-1095, 2013.

[38] J. N. Yang, S. Lin, H. Huang, and L. Zhou, "An adaptive extended Kalman filter for structural damage identification," *Structural Control and Health Monitoring: The Official Journal of the International Association for Structural Control and Monitoring and of the European Association for the Control of Structures,* vol. 13, pp. 849-867, 2006.

[39] M. N. Chatzis, E. N. Chatzi, and A. W. Smyth, "An experimental validation of time domain system identification methods with fusion of heterogeneous data," *Earthquake Engineering & Structural Dynamics,* vol. 44, pp. 523-547, 2015.

[40] M. Ismail, F. Ikhouane, and J. Rodellar, "The hysteresis Bouc-Wen model, a survey," *Archives of Computational Methods in Engineering,* vol. 16, pp. 161-188, 2009.

[41] V. Hassani, T. Tjahjowidodo, and T. N. Do, "A survey on hysteresis modeling, identification and control," *Mechanical Systems and Signal Processing,* vol. 49, pp. 209-233, 2014.

[42] B. Spencer Jr, S. Dyke, M. Sain, and J. Carlson, "Phenomenological model for magnetorheological dampers," *Journal of Engineering Mechanics,* vol. 123, pp. 230-238, 1997.

[43] G. Yang, B. F. Spencer Jr, H.-J. Jung, and J. D. Carlson, "Dynamic modeling of large-scale magnetorheological damper systems for civil engineering applications," *Journal of Engineering Mechanics,* vol. 130, pp. 1107-1114, 2004.

[44] M. S. Miah, E. N. Chatzi, V. K. Dertimanis, and F. Weber, "Nonlinear modeling of a rotational MR damper via an enhanced Bouc–Wen model," *Smart Materials and Structures,* vol. 24, p. 105020, 2015.

[45] P. Sengupta and B. Li, "Modified Bouc–Wen model for hysteresis behavior of RC beam–column joints with limited transverse reinforcement," *Engineering Structures,* vol. 46, pp. 392-406, 2013.

[46] C.-L. Ning, B. Yu, and B. Li, "Beam-column joint model for nonlinear analysis of non-seismically detailed reinforced concrete frame," *Journal of Earthquake Engineering,* vol. 20, pp. 476-502, 2016.

[47] B. Soneji and R. Jangid, "Influence of soil–structure interaction on the response of seismically isolated cable-stayed bridge," *Soil Dynamics and Earthquake Engineering,* vol. 28, pp. 245-257, 2008.

[48] L. Jeen-Shang and Z. Yigong, "Nonlinear structural identification using extended Kalman filter," *Computers & Structures,* vol. 52, pp. 757-764, 1994.

[49] M. Hoshiya and E. Saito, "Structural identification by extended kalman filter," *ASCE Journal of Engineering Mechanics,* vol. 110, pp. 1757-1770, 1984.

[50] W. Song and S. J. Dyke, "Application of nonlinear observers in hysteretic model updating," in *Sensors and Smart Structures Technologies for Civil, Mechanical, and Aerospace Systems 2010*, 2010, p. 764732.

[51] A. Calabrese, S. Strano, and M. Terzo, "Adaptive constrained unscented Kalman filtering for real-time nonlinear structural system identification," *Structural Control and Health Monitoring*, vol. 25, p. e2084, 2018.

[52] M. Wu and A. W. Smyth, "Real-time parameter estimation for degrading and pinching hysteretic models," *International Journal of Non-Linear Mechanics*, vol. 43, pp. 822-833, 2008.

[53] M. Wu and A. W. Smyth, "Application of the unscented Kalman filter for real-time nonlinear structural system identification," *Structural Control and Health Monitoring*, vol. 14, pp. 971-990, 2007.

[54] Y. Yang and F. Ma, "Constrained Kalman filter for nonlinear structural identification," *Modal Analysis*, vol. 9, pp. 1343-1357, 2003.

[55] S. Sen and B. Bhattacharya, "Online structural damage identification technique using constrained dual extended Kalman filter," *Structural Control and Health Monitoring*, vol. 24, p. e1961, 2017.

[56] R. Kandepu, L. Imsland, and B. A. Foss, "Constrained state estimation using the unscented Kalman filter," in *2008 16th Mediterranean Conference on Control and Automation*, 2008, pp. 1453-1458.

[57] P. Vachhani, S. Narasimhan, and R. Rengaswamy, "Robust and reliable estimation via unscented recursive nonlinear dynamic data reconciliation," *Journal of Process Control*, vol. 16, pp. 1075-1086, 2006.

[58] D. Li, X. Dong, and Y. Wang, "Model updating using sum of squares (SOS) optimization to minimize modal dynamic residuals," *Structural Control and Health Monitoring*, vol. 25, p. e2263, 2018.

[59] S. P. Boyd and L. Vandenberghe, *Convex Optimization*. Cambridge, UK ; New York: Cambridge University Press, 2004.

[60] P. A. Parrilo, "Semidefinite programming relaxations for semialgebraic problems," *Mathematical Programming*, vol. 96, pp. 293-320, 2003.

[61] S. Basu, R. Pollack, and M.-F. Roy, *Algorithms in Real Algebraic Geometry* vol. 4: Springer Heidelberg, 2003.

[62] J. B. Lasserre, *An Introduction to Polynomial and Semi-Algebraic Optimization* vol. 52: Cambridge University Press, 2015.

[63] D. Henrion and J. B. Lasserre, "Detecting global optimality and extracting solutions in GloptiPoly," in *Positive Polynomials in Control*, ed: Springer, 2005, pp. 293-310.

[64] J. B. Lasserre, "Global optimization with polynomials and the problem of moments," *SIAM Journal on Optimization,* vol. 11, pp. 796-817, 2001.

[65] J. Nocedal and S. Wright, *Numerical Optimization*: Springer Science & Business Media, 2006.

[66] MathWorks Inc., *Optimization Toolbox™ User's Guide,* Version 6. ed. Natick, MA: MathWorks Inc., 2016.

[67] T. F. Coleman and Y. Li, "An interior trust region approach for nonlinear minimization subject to bounds," *SIAM Journal on optimization,* vol. 6, pp. 418-445, 1996.

[68] D. Li and Y. Wang, "Sparse sum-of-squares optimization for model updating through minimization of modal dynamic residuals," *Journal of Nondestructive Evaluation, Diagnostics and Prognostics of Engineering Systems,* vol. 2, p. 011005, 2019.

[69] S. Zhang, "A new self-dual embedding method for convex programming," *Journal of Global Optimization,* vol. 29, pp. 479-496, 2004.

[70] F. Permenter and P. Parrilo, "Partial facial reduction: simplified, equivalent SDPs via approximations of the PSD cone," *Mathematical Programming,* vol. 171, pp. 1-54, 2018.

[71] Y.-L. Cheung, "Preprocessing and reduction for semidefinite programming via facial reduction: theory and practice," PhD, University of Waterloo, 2013.

[72] Y. Zhu, G. Pataki, and Q. Tran-Dinh, "Sieve-SDP: a simple facial reduction algorithm to preprocess semidefinite programs," *Mathematical Programming Computation,* vol. 11, pp. 503-586, 2019.

[73] J.-B. Lasserre and V. Magron, "In SDP relaxations, inaccurate solvers do robust optimization," *SIAM Journal on Optimization,* vol. 29, pp. 2128-2145, 2019.

[74] J. Nie and L. Wang, "Regularization methods for SDP relaxations in large-scale polynomial optimization," *SIAM Journal on Optimization,* vol. 22, pp. 408-428, 2012.

[75] P. Biswas, T.-C. Liang, K.-C. Toh, Y. Ye, and T.-C. Wang, "Semidefinite programming approaches for sensor network localization with noisy distance measurements," *IEEE Transactions on Automation Science and Engineering,* vol. 3, pp. 360-371, 2006.

[76] D. Simon, *Optimal state estimation: Kalman, H infinity, and nonlinear approaches*: John Wiley & Sons, 2006.

[77] N. Gupta and R. Hauser, "Kalman filtering with equality and inequality state constraints," *arXiv preprint arXiv:0709.2791*, 2007.

[78] S. Julier, J. Uhlmann, and H. F. Durrant-Whyte, "A new method for the nonlinear transformation of means and covariances in filters and estimators," *IEEE Transactions on Automatic Control*, vol. 45, pp. 477-482, 2000.

[79] T. Kailath, "Lectures on Wiener and Kalman filtering," in *Lectures on Wiener and Kalman Filtering*, ed: Springer, 1981, pp. 1-143.

[80] H. Ebrahimian, R. Astroza, and J. P. Conte, "Extended Kalman filter for material parameter estimation in nonlinear structural finite element models using direct differentiation method," *Earthquake Engineering & Structural Dynamics*, vol. 44, pp. 1495-1522, 2015.

[81] L. Wang and Z. Lu, "Identification of Bouc-Wen hysteretic parameters based on enhanced response sensitivity approach," *Journal of Physics: Conference Series*, vol. 842, p. 012021, 2017.

[82] J. N. Juang and R. S. Pappa, "An eigensystem realization algorithm for modal parameter identification and model reduction," *Journal of Guidance Control and Dynamics*, vol. 8, pp. 620-627, 1985.

[83] A. K. Chopra, *Dynamics of Structures: Theory and Applications to Earthquake Engineering*, 2nd ed. Upper Saddle River, NJ: Prentice Hall, 2001.

[84] M. Paz, "Dynamic condensation," *AIAA Journal*, vol. 22, pp. 724-727, 1984.

[85] M. Papadopoulos and E. Garcia, "Improvement in model reduction schemes using the system equivalent reduction expansion process," *AIAA Journal*, vol. 34, pp. 2217-2219, 1996.